ABSTRACT

Title of Document:	AEROSOL SYNTHESIS OF CATHODE MATERIALS FOR NA-ION AND LI-ION BATTERIES
	Alex Langrock, Doctor of Philosophy, 2014
Directed By:	Professor Chunsheng Wang Department of Chemical and Biomolecular Engineering

Energy production and storage are important issues that play a key role in our daily lives. There is a need for high energy and high power systems for portable electronic devices and zero-emission vehicles. Lithium-ion batteries are crucial in addressing these needs. However, for the smart electric grid and renewable energy storage where cost is critical but weight and footprint requirement is less important, the sodium-ion battery is the most suitable power sources. To achieve both high power density and high energy density, nanostructured sphere particles with controlled porosity and high tapping density are desired for both Li-ion and Na-ion batteries. The versatile and facile ultrasonic spray pyrolysis method allows for the synthesis of a variety of electrode materials with sphere morphology. Work has been done to develop electrode materials through an aerosol method that can be readily applied to industry.

Two classes of high energy cathodes suitable for lithium-ion batteries were studied. These include the 5V spinels and lithium-rich materials. The 5V spinels are a promising class of electrodes for secondary lithium batteries. This class of material has the highest intrinsic rate capability of the intercalation cathodes with high safety, low toxicity, and low cost

making it ideal for high-power applications such as electric vehicles, while the lithium-rich compounds exhibit high capacity and reasonable cycle stability.

Two classes of stable cathodes suitable for sodium-ion batteries were studied. The first was carbon coated porous hollow Na_2FePO_4F spheres with 500 nm diameter and 80 nm wall thickness synthesized by a one-step template-free ultrasonic spray pyrolysis process using sucrose as the carbon source. Nano-sized porous hollow Na_2FePO_4F spheres allow electrolyte to penetrate into the hollow structure, and thus the electrochemical reaction can take place on both the outside and inside surface and in the pores. Also, the carbon coating on Na_2FePO_4F hollow spheres enhances the electronic conductivity and charge transfer reaction kinetics. The exceptional performance of hollow Na_2FePO_4F spheres combined with mature aerosol spray synthesis technology make these carbon coated porous hollow Na_2FePO_4F spheres very promising as cathode materials for practical applications in Na-ion batteries. Finally, P2-type earth abundant layered oxides with high energy density and long cycling stability were also developed and studied. These layered materials were investigated due to their high theoretical capacity.

A novel ultrasonic spray pyrolysis system has been developed to effectively coat any cathode, including layered oxides, with a thin layer of carbon to improve the kinetics and increase the electronic conductivity. The residence time in air is sufficiently short to allow the decomposition of the carbon source (sucrose) without further reduction of the cathode material. A vertical configuration allows the solid particles to reach the filter for collection with high efficiency. As a test sample, lithium-rich cathodes have been successfully carbon coated and compared with the bare material.

AEROSOL SYNTHESIS OF CATHODE MATERIALS FOR NA-ION AND LI-ION
BATTERIES

By

Alex Langrock

Dissertation submitted to the Faculty of the Graduate School of the
University of Maryland, College Park, in partial fulfillment
of the requirements for the degree of
Doctor of Philosophy
2014

Advisory Committee:
Professor Chunsheng Wang, Chair
Professor Sheryl Ehrman
Professor Dongxia Liu
Professor Liangbing Hu
Professor Bao Yang

Dedication

This dissertation is dedicated to my family for their love and support.

Acknowledgements

I would like to thank my advisor Dr.Chunsheng Wang for his guidance and support over the last four years. I'm grateful for the opportunity to study and work with him. Additionally, I would like to acknowledge Dr. Yunhua Xu who would never hesitate to take time out of his busy schedule to help me with any of my doubts and assist me in getting acquainted with the lab equipment. I would also like to thank all my group members past and present– Yujie Zhu, Yanting Luo, Yihang Liu, Yang Wen, Chao Luo, Ying Liu, Fudong Han, Tao Gao, and Jianfeng Mao –who were always helpful when I had questions. Lastly, I want to acknowledge my parents and sister whose unwavering support has gotten me to where I am today.

Table of Contents

List of Tables

List of Figures

Chapter 1: Introduction and Overview

This dissertation centers on the synthesis of electrode materials for both lithium and sodium-ion batteries using spray pyrolysis technology. Spray pyrolysis is a versatile and facile technique that involves the atomization of a precursor solution which is transported through a high temperature reactor via carrier gas. The as prepared powder is collected downstream once the filter material has been sufficiently coated. Final particle size can be controlled mainly through the choice of precursor solution concentration, while reactor temperature and carrier gas flow rate are basic operating variables that govern the residence time in the reactor and influence morphology. This technique has a number of positive attributes. Relatively pure phase particles in the submicrometer range can be created. A wide range of chemical compositions can be produced including complex, multicomponent ceramic systems. Each droplet acts as a microreactor in which the constituents are mixed on the atomic level hence particle homogeneity is predicted. The method has the added benefit of continuous formation of particles in one step, thus it can be applied to industry. As a result, spray pyrolysis is ideal for synthesizing electrode materials for batteries.

Batteries are ubiquitous in today's world. From portable electronics to electric vehicles to the smart grid, the demand for greatly enhanced energy density and improved stability continues to grow. Two promising battery technologies are lithium and sodium-ion. Lithium-ion batteries have emerged as the battery of choice for portable electronics and electric vehicles due to their large energy density, no

memory effect, and slow loss of charge when not in use. Sodium-ion batteries are a promising alternative as the supply of lithium is limited and the cost continues to increase. Sodium-ion batteries are better suited for medium and large-scale stationary energy storage as the redox potential and energy density is lower than that of lithium. Much research is still needed to improve the performance of both lithium and sodium-ion batteries and this provides the motivation for the present dissertation.

Research Objectives

The objective of the current research is to develop high energy cathode materials for lithium ion battery (LIB) and sodium ion battery (NIB) technology. Particular focus is placed on synthesis of nanostructured cathode materials using aerosol spray pyrolysis method.

The goals of the study are:

　i. Enhance the energy and power density of LIBs by developing high voltage spinels

　ii. Increase the capacity of LIB cathodes by developing lithium-rich layered oxides

　iii. Improve cycle life of NIBs by synthesizing unique hollow porous C/Na_2FePO_4F

　iv. Increase capacity of NIB cathodes by developing P2-type layered oxides

The subsequent five chapters discuss the efforts to achieve the stated goals. Chapter 2 provides background into the historical development of rechargeable batteries along with the components of a battery, including the anode, cathode, and electrolyte. The chapter concludes with a description of the ultrasonic spray pyrolysis process used in

this study. Chapter 3 focuses on the first goal and discusses the characterization and electrochemical performance of 5V spinels. Chapter 4 investigates the performance of lithium-rich layered oxides. Chapter 5 will focus on improving cycle life of NIBs through the synthesis of hollow porous carbon coated Na_2FePO_4F. Chapter 6 studies the performance of P2-type transition metal oxides for NIBs with the aim of increasing capacity of NIB cathodes.

Chapter 2: Background

In this chapter we reviewed rechargeable batteries along with the components of a battery, including the anode, cathode, and electrolyte. Thereafter, we describe the ultrasonic spray pyrolysis process in detail.

2.1 Development of Secondary Batteries

A battery consists of one or more cells that convert chemical energy into electrical energy and is usually composed of a positive electrode (cathode) and a negative electrode (anode) separated by ionically conducting and electronically insulating electrolyte. Batteries are classified into two categories: primary and secondary batteries. The primary battery can only convert chemical energy to electrical energy, thus they consist of non-rechargeable cells. Batteries that can restore their chemical energy or original chemical composition by supplying an electrical current are called secondary (or rechargeable) batteries.

The first secondary battery, the lead-acid cell, was invented in 1859 by French physicist Gaston Plante. A lead-acid cell consists of a lead anode and a lead oxide cathode submerged in a sulfuric acid solution, with the redox shuttle taking place between elemental Pb and Pb^{n+} supplying the current. Due to its dependability and inexpensive cost-per-watt base, the lead-acid battery is still widely used today in automobiles and other uninterruptible power supplies. Despite the low cost of

material, a lead-acid battery suffers from low specific energy (30-50 Wh kg^{-1}) and limited cycle life (200-300 cycles).

By the mid 1900s, the nickel-cadmium (NiCd) and nickel-metal hydride (NiMH) secondary batteries were developed. These have an improved energy density, 45-80 Wh kg^{-1} and 60-120 Wh kg^{-1}, respectively. Nonetheless, the metal Cd and rare earth elements used in these batteries are very expensive, so NiCd and NiMH batteries are not suitable for large-scale applications. Some applications of Ni based secondary batteries include power tools and emergency medical equipment.

Experimentation with lithium batteries began as early as 1912 under G.N. Lewis. It wasn't until the 1970's that primary lithium batteries were commercialized. During the 1980's, innovations by John B. Goodenough and Akira Yoshino allowed for the first lithium-ion battery (LIB) prototype, which was a rechargeable and more stable version of the lithium battery. In 1991, Sony commercialized the lithium-ion battery. Lithium batteries are widely regarded to be the most promising electronic energy storage intermediates for consumer electronics, transportation, and large energy storage facilities for renewable sources that require high volumetric and gravimetric energy densities (**Figure 2.1**).
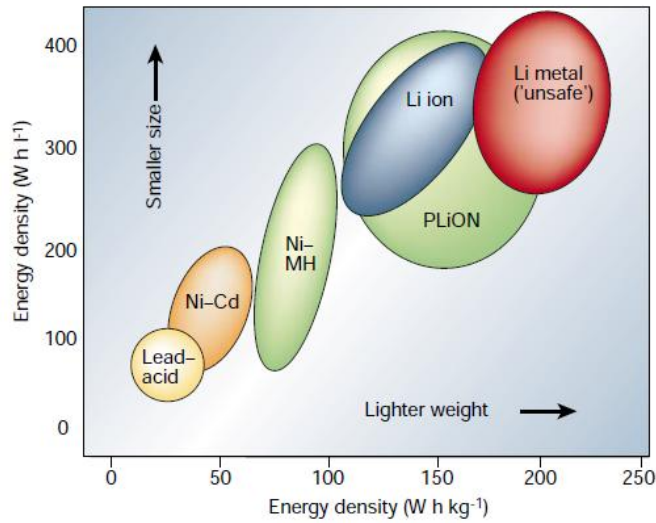
Figure 2.1 Comparison of energy densities for various battery technologies [2.1]

2.2 Advantages and Disadvantages of LIBs

LIBs have several advantages over other secondary battery chemistries. First, LIBs

are much lighter than other batteries due to their high gravimetric capacity. Second,

the pair of $LiCoO_2$ and graphite delivers a working voltage of ~3.8V, which is much

higher than other rechargeable batteries, i.e. ~2.0 V for lead-acid batteries, 1.2V for

nickel-cadmium (Ni-Cd) batteries, and 1.2 V for nickel metal hydride (Ni-MH). This

feature increases the power density of LIBs, which means LIBs can deliver more

power at the same current compared to other rechargeable batteries. Third, LIBs do

not have a memory effect as found in Ni-Cd rechargeable batteries. In Ni-Cd

rechargeable batteries, the maximum capacity gradually decreases if the Ni-Cd

batteries are charged after being only partially discharged. It appears as though the

battery remembers the smaller capacity. However, LIBs can be charged at any depth

of discharge (DOD) status without losing any maximum capacity. It is not necessary

6

to discharge fully before charging. Fourth, the self-discharge rate in LIBs is very low, about 5-10% per month. This rate is much less than 10% per month in Ni-Cd batteries, and 30% per month in Ni-MH batteries.

LIBs are not without disadvantages. First, LIBs have high internal resistance compared to other rechargeable batteries, which limit the power density of LIBs. The internal resistance continually increases with both cycling and age due to the formation of deposits inside the electrolyte. The formation of deposits in the organic electrolyte hinders lithium ion transport and causes a decline in working voltage. Second, LIBs can experience thermal runaway and cell rupture if the LIB is over-charged or over-discharged.

The evolution of secondary battery chemistry through the years is shown in **Figure 2.2**.
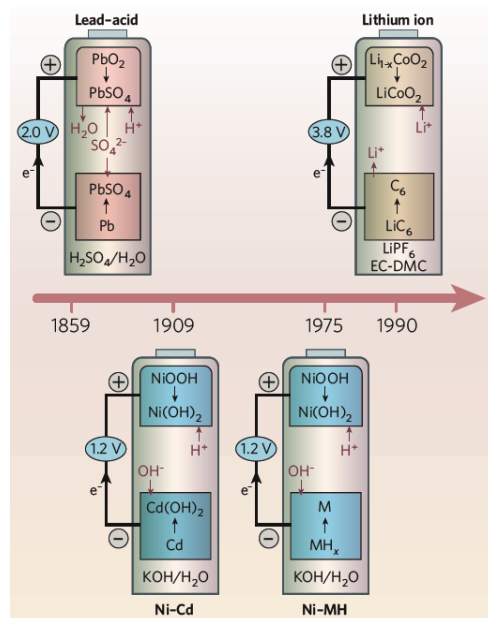
Figure 2.2 Battery chemistry through the years [2.2]

2.3 Advantages and Disadvantages of NIBs

Unlike lithium, sodium is one of the more abundant elements on Earth and exhibits similar insertion chemistries to Li, indicating that Na chemistry could be applied to a similar battery system. The use of Na instead of Li in rechargeable batteries could mitigate the expected shortage of lithium in an economic way, due to abundance of sodium sources, the ease to recover it, and its lower price. As battery applications extend to large-scale storage such as electric buses or stationary storage connected to renewable energy production, high energy density becomes less significant.

Despite the relative abundance and lower cost, electrochemical Na-ion cells will always fall short of meeting energy densities of Li-ion batteries. This is due to the equivalent weight of Na being higher than Li and the electromotive force voltage of sodium versus lithium is approximately 300 mV less. Finding a suitable host material to accommodate Na-ions and allow reversible and rapid ion insertion and extraction has also been a challenge due to a 55% larger radius than Li-ions.

2.4 Anodes for LIBs

In order for a material to be a good anode it should possess certain features, including high capacity (charge storage ability), low irreversible capacity (low capacity loss when undergoing cycling), low insertion potential (70-100 mV), long cycle life, high mixed conductivity, and be electrochemically stable with the other components in the cell. Carbonaceous materials with various consistencies and morphologies have been used for LIBs due to their availability, low cost, and good lithium intercalation/de-

8

intercalation reversibility. Carbon based materials used as active anode in LIBs are classified into two categories, according to the degree of crystallinity and stacking (1) soft carbon (graphitizable carbon) where crystallites are stacked nearly in the same direction and (2) hard carbon (non-graphitizable carbon) where crystallites have disordered orientation. The majority of lithium-ion batteries produced today use graphite as the anode; however, a major issue is the low specific capacity (372 mAh g^{-1}), which has limited its use to low power devices, including mobile phones and laptops. [2.3]

As a result, further advances in anode materials are necessary for high power consuming applications, such as electric vehicles. Other Group IV elements, including silicon (4212 mAh g^{-1}) and germanium (1624 mAh g^{-1}) possess substantially larger theoretical capacities as intercalation anodes; however, their brittleness results in rapid capacity fading. In the case of Si, the insertion process is accompanied by a large volume change of the Si matrix, which results in the structure to break after a few cycles. The breaks reduce the contact between the Si matrix and the current collector, which leads to a loss in capacity. **Table 2.1** contains a detailed list of the most commonly studied anode materials for LIBs and includes advantages/disadvantages associated with each.

Table 2.1 Common anodes used for LIBs

Active Anode Materials	Theoretical Capacity (mAh g^{-1})	Advantages	Disadvantages
Intercalation Materials			
A. Carbon			
a. Hard Carbons [2.4]	200-600	➢ Good working potential ➢ Low cost ➢ Good safety	➢ Low coulombic efficiency ➢ Large voltage hysteresis ➢ Large irreversible capacity
b. CNTs [2.5]	1116		
c. Graphene [2.6]	780		
B. Titanium Oxides		➢ Good safety ➢ Good cycle life ➢ Low cost ➢ High power capability	➢ Low capacity ➢ Low energy density
a. LiTi$_4$O$_5$ [2.7]	175		
b. TiO$_2$ [2.7]	330		
Alloy Materials		➢ High specific capacities ➢ High energy density ➢ Good safety	➢ Large irreversible capacity ➢ Dramatic capacity fading ➢ Poor cycling
a. Silicon [2.8]	4212		
b. Germanium [2.9]	1624		
c. Tin [2.10]	993		
d. Antimony [2.11]	660		
e. Tin Oxide [2.12]	790		
f. SiO [2.13]	1600		
Conversion Materials			
a. Metal Oxides [2.14]	500-1200	➢ High specific capacities ➢ High energy density ➢ Low cost ➢ Environmentally compatible ➢ Low operating potential	➢ Low coulombic efficiency ➢ Unstable SEI formation ➢ Large voltage hysteresis ➢ Poor cycle life ➢ Poor capacity retention
b. Metal phosphides/sulfides/nitrides [2.15]	500-1800		

2.5 Anodes for NIBs

Unlike Li, only a limited amount of Na can be stored in graphite (~NaC_{70}). Hard carbons remain the main candidate to be used as anode for NIBs, although their performance is far from that achieved by graphite in LIBs. Recent advancements to improve cyclability have included the use of hierarchically porous carbons prepared by templating routes. [2.16] Other commonly studied anodes for NIBs include the titanates, tin and antimony alloys, and binary compounds reacting through conversion reactions. **Table 2.2** lists the most relevant anode materials for NIBs. [2.17]

Table 2.2 Common anodes used for NIBs

Active Anode Materials	Experimental Reversible Capacity (mAh g^{-1})	Voltage range (V)
Hard Carbon	350	0-1.0
$Na_2Ti_3O_7$	177	0.3
Sn	850	0.2-1.0
Sb	580	0.04-1.5
Fe_3O_4	350	0.04-3.0

2.6 Cathodes for LIBs

In order for a material to be a good cathode it should possess certain features, including high capacity (charge storage ability), low irreversible capacity (low capacity loss when undergoing cycling), high insertion potential (> 4 V), long cycle

11

life, high mixed conductivity, and be electrochemically stable with the other components in the cell. Commercialized cathodes for the lithium-ion battery include $LiCoO_2$, $LiFePO_4$, and $LiMn_2O_4$ among others. **Table 2.3** provides the theoretical capacity and insertion potential of different cathode materials for LIBs.

Table 2.3 Common cathodes used for LIBs

Active Cathode Materials	Theoretical Capacity (mAh g^{-1})	Average Operating Voltage vs. Li/Li$^+$ (V)
$LiCoO_2$	140	3.7
$LiMn_2O_4$	100	4.0
$LiFePO_4$	150	3.3
$Li[Li_aNi_xMn_yCo_z]O_2$	220	4.2

2.7 Cathodes for NIBs

A great range of compounds are being investigated as possible cathodic materials for NIBs, these include oxides, phosphates, and fluorophosphates. The layered oxides $NaMO_2$ (M=Ni,Mn,Fe,Co,Cr,V, etc.) are considered to be among the most promising cathode system for Na due to their high capacity, low material cost, and safety. **Table 2.4** lists the most relevant cathode materials for NIBs.

Table 2.4 Common cathodes used for NIBs

Active Cathode Materials	Experimental Reversible Capacity (mAh g^{-1})	Average Operating Voltage vs. Na/Na$^+$ (V)
P2-Na$_x$[Fe$_{1/2}$Mn$_{1/2}$]O$_2$	200	2.75
O3-Na[Ni$_{1/3}$Fe$_{1/3}$Mn$_{1/3}$]O$_2$	100	2.75
Na$_{0.44}$MnO$_2$	160	2.75
Na$_2$FePO$_4$F	124	2.9-3.0
Prussian Blue analogues	200	3.3

2.8 Electrolytes

The electrolyte is the medium which conducts ions between electrodes. It separates both electrodes to prevent direct electrical contact while still allowing mutual ionic exchange. The electrolyte phase can consist of a liquid salt solution, polymer gel, or a glassy solid. The characteristics of a good electrolyte are a wide and stable electrochemical window, an ionic conductivity of $>10^{-4}$ S/cm over the temperature range of operation, an electronic conductivity $<10^{-10}$ S/cm so that electrons find the route through the external circuit to be the path of least resistance. Additionally, the electrolyte should be chemically stable with respect to the electrodes, including the ability to rapidly form a passivating solid-electrolyte interface layer to minimize the effect of interfacial resistance. The electrolyte should also be non-flammable, non-explosive in the event of a short circuit, non-toxic, and inexpensive.

2.9 Reaction Mechanism in Rechargeable Batteries

The anode supplies electrons to the external circuit during discharge and is oxidized. The cathode accepts electronics and is reduced. The anode is the source of electrons, thus is called the negative electrode, while the cathode is the positive electrode. In a secondary battery, the anode and cathode are soaked in electrolyte and separated by an ionic conductive separator. The ions (Li+ or Na+) migrate between the cathode and anode through the separator during charge and discharge. Electrons migrate through the external circuit to avoid internal short-circuit of the battery. During charge, the cations diffuse toward the anode and electrons are released to the external circuit. The reverse process occurs during discharge, where cations are transported back to the cathode from the anode and electrons move back to the cathode through the external circuit. A schematic of a LIB is shown in **Figure 2.3**.
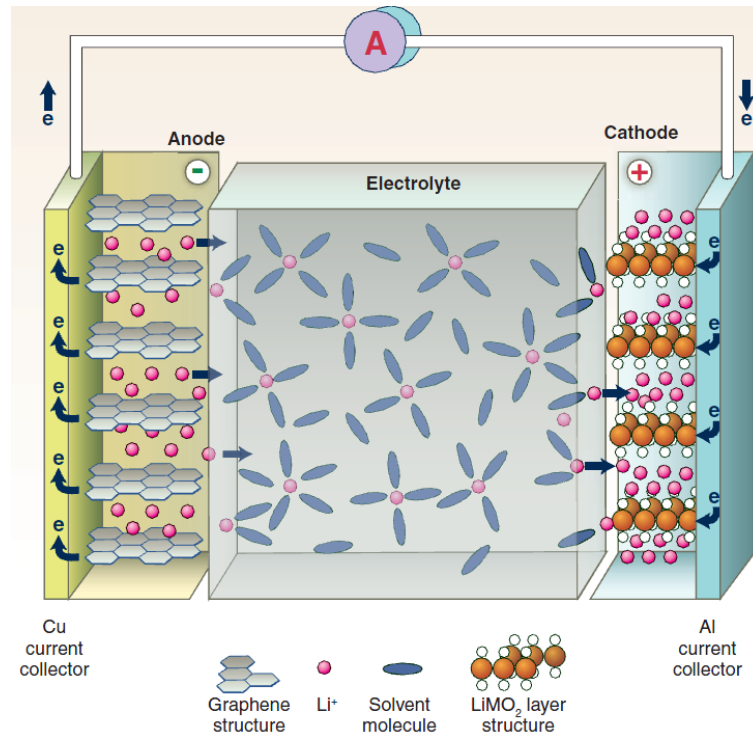
Figure 2.3 Schematic of a LIB [2.18]

2.10 Electrochemistry Overview

The theoretical electromotive force of a battery, E_{th}, is related to the Gibbs free energy:

$$\Delta G = -nFE_{th} \tag{2.1}$$

where n is the charge number of the ionic species (n=1 for Li^+ or Na^+) and F is Faraday's constant or the charge on a mole of electrons (96,500 C mol^{-1}). The voltage of a cell is determined by the chemical potential difference between the positive and negative electrodes. For LIBs, the voltage of a cell is determined by the difference of chemical potentials of lithium atoms in positive and negative electrodes. When these electrodes are connected by means of an external device, electrons spontaneously flow from the more negative to the more positive potential. Ions are transported through the electrolyte, maintaining the charge balance and electrical energy is tapped by the external circuit. A larger voltage applied in the opposite direction can cause the battery to recharge. The cell can maintain an electrostatic potential with extremely slow self-discharge since the separator only allows the penetration of cations. Since the electrolyte and separator are ionic conductors, the transportation of electrons between the two electrodes is eliminated. The practical voltage of a battery E_p is not always equivalent to E_{th} as impedance exists due to the transport of ions causing a voltage drop. The impedance Z is the instantaneous ratio of applied voltage to the current, I, across the circuit, when time dependent changes in structure or composition occur. The practical voltage can be written as:

$$E_p = E_{th} - I\,Z \tag{2.2}$$

Several parameters are important when studying the electrochemical performance of a battery or an electrode material. *Specific energy density* is the energy available per unit mass (Wh kg^{-1}), while *energy density* refers to the amount of energy per unit volume (Wh L^{-1}). Energy density is crucial for electric vehicles where limited space is available for battery packs. In galvanic cells, *specific capacity*, or simply *capacity* (mAh g^{-1}) is normally used. The theoretical capacity, Q, can be calculated from the chemistry of the reactant taking part in the reaction:

$$Q = \frac{x\,n\,F}{3.6\,MW} \qquad\qquad (2.3)$$

where x is the equivalent of lithium or sodium in the formula unit, n is the net charge of the ionic species ($n=1$ for Li$^+$ or Na$^+$), F is Faraday's constant or the charge on a mole of electrons (96,500 C mol^{-1}), and MW is the molecular weight of the compound.

There are three main ways to maximize the stored energy content of a battery:

(1) by having a large chemical potential difference between the two electrodes

(2) by minimizing the mass or volume of the reactants per exchanged electron

(3) by ensuring that the electrolyte is not consumed in the chemistry of the battery

Cycle life is another term used when analyzing secondary batteries and refers to the number of times a cell can be effectively recharged before its capacity becomes too low. *Coulombic efficiency*, η, is the fraction of the prior charge capacity that is available during the discharge:

$$\eta = \frac{n^{th}\ discharge}{n^{th}\ charge} * 100\% \qquad\qquad (2.4)$$

16

Higher coulombic efficiency corresponds to better cycleability of a battery. The irreversible capacity loss, Q_{irr}, refers to the amount of capacity lost after each cycle:

$$Q_{irr} = \frac{n^{th}\ charge - n^{th}\ discharge}{n^{th}\ charge} * 100\% \qquad (2.5)$$

Another important parameter is the *C-rate*, the rate at which a battery is charged/discharged. C-rate is expressed as C/t, where t is the number of hours required to completely charge/discharge a battery.

The four most common battery configurations along with their components are shown in **Figure 2.4**.
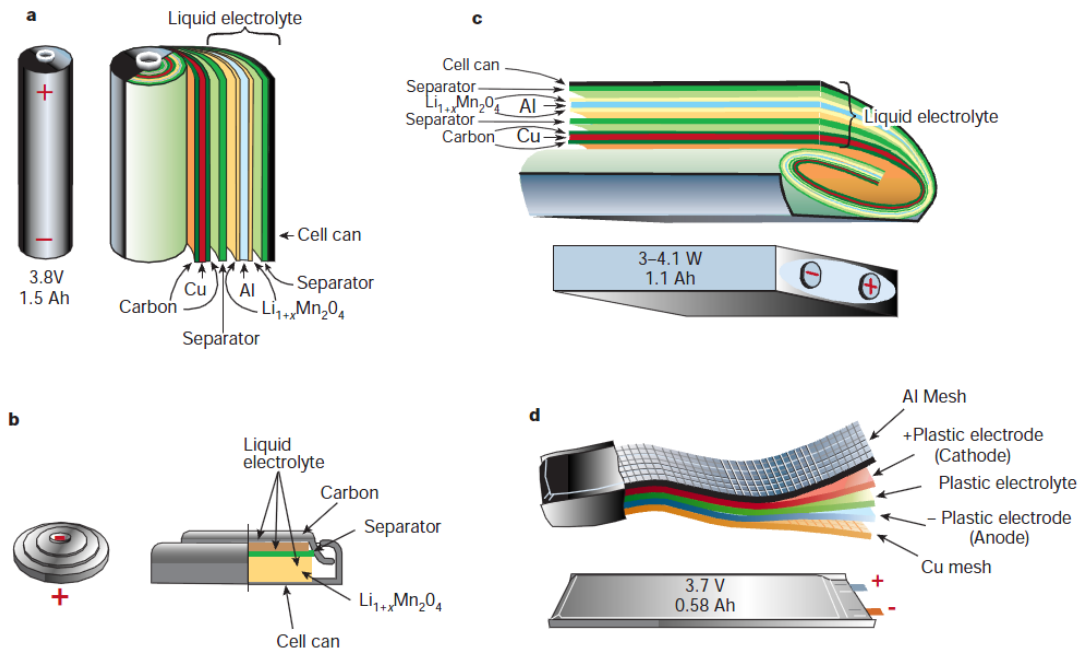
Figure 2.4 Common battery configurations (a) cylindrical, (b) coin, (c) prismatic, (d) pouch [2.1]

Copper foil is widely used as the anode current collector, since it does not react with lithium or sodium ions at low electrical potential. Aluminum foil is used as the cathode current collector, since it is resistant to an oxidizing potential. Fine, porous, thin films of polyethylene or polypropylene are used as separators.

Half cells are often assembled for fundamental research of LIB/NIB electrodes. The term half cell refers to a cell consisting of a single electrode (either positive or negative) as the working electrode (WE) and pure lithium/sodium metal as the counter electrode (CE). In this type of cell, the CE is also used as a reference electrode (RE), whose electrochemical potential does not change and is set to zero. In this study 2032 coin cells were assembled for all battery tests (**Figure 2.5**).
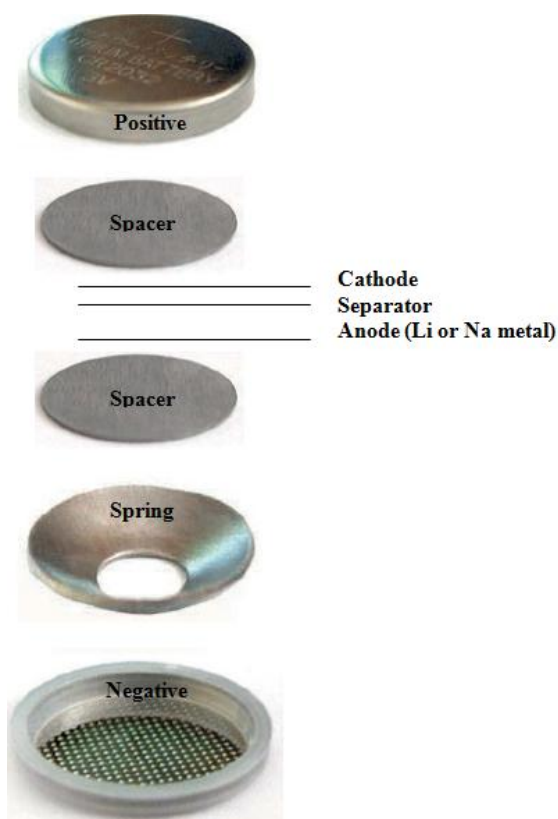
Figure 2.5 Coin cell assembly

2.11 Synthesis Methods for Electrode Materials

The most straightforward method for producing electrode materials is the solid-state reaction, which requires the addition of no solvent during the chemical reaction. This

method is widely used in industry due to the low process costs and simplicity of the procedure. The properties of the powders are affected by the purity of the precursors and long calcinations time is required for complete reaction and grain growth. Prolonged mechanical grinding is needed to obtain the desired particle size. Consequently, it is difficult to control particle size, morphology, and homogeneity. A more sophisticated method for producing materials with desired chemical composition and morphology are wet-chemical processes which require solvents and in some cases additives. The three main wet-chemistry processes are (1) sol-gel, (2) hydrothermal, and (3) coprecipitation methods. Unlike solid-state reactions, wet-chemistry is a low temperature synthesis process which can produce submicron size powders with unique morphologies, including aggregates, wires, flakes, and spheres. The sol-gel process involves the following steps:

- Mixing of the precursors (metal hydrates, nitrates, etc.) and gelation agents (citric acid, polyacrylic acid and polyvinylpyrrolidone etc.) while controlling the pH

- Sol formation

- Gel formation (applying heat at ~80 °C)

- Calcination of the gel to form solid ceramic powders

- Post-calcination at a higher temperature to obtain the desired crystalline phase

The hydrothermal process is similar to the sol-gel process, except no gelation agent is used and different heating temperatures are used. The precursor (metal salts and surfactant) is placed in a low temperature environment, often in an autoclave heated between 120 °C and 400 °C for several hours. Once the reaction is complete, the

19

resulting precipitates are cooled, washed, dried, and further calcined at a higher temperature to obtain the desired crystalline phase and remove the carbonaceous surfactant. Both the sol-gel and hydrothermal methods require a sustained moderate heating temperature along with organic gelation or surfactant, which adds to the material manufacturing cost. As a result, these methods tend not to be used for large scale industrial applications. More recently, the most commonly used wet-chemistry method is the coprecipitation process since the organic gelation agent or surfactant is not needed. Additionally, under certain conditions spherical particles can be produced, which promotes good packing density of the electrodes. In the initial step, the precursors (metal salts, chelating agent) are pumped in a continuous stirred tank reactor. The temperature, pH, stirring speed and concentration are controlled to form homogenous precipitates of carbonate powders, which serve as a solid precursor for further synthesis. The resulting powders are collected, washed, and dried under vacuum for several hours to remove residual chemicals and water. A stoichiometric amount of lithium or sodium carbonate is mixed with the original precipitate, which is calcined to decompose the precursor. Although electrochemical performance from the coprecipitation method has been good, the process suffers from reproducibility issues during scale-up resulting from phase separation during synthesis. In summary, wet-chemistry is a multi-step process which requires precise control over precursor chemistry, reaction temperature, pH, and long calcinations time. Control over the stoichiometry is challenging, especially when scaling the process up.

2.12 Ultrasonic Spray Pyrolysis

An ultrasonic spray pyrolysis (USP) technique was employed to synthesize various electrode materials due to its simplicity and ability to obtain unique morphology. USP involves the following major steps: ultrasonic generator which produces high frequency ultrasonic waves, beyond the range of human hearing. This high frequency signal is applied to a piezoelectric transducer. The transducer converts the high frequency signals to mechanical energy. The resulting energy is used to convert the precursor solution into a fine mist. Two major hypotheses have been proposed to explain the mechanism of liquid disintegration during ultrasonic atomization, namely the cavitation hypothesis and capillary wave hypothesis. Cavitation hypothesis is generally applied to high frequency and high energy intensity systems. When the solution is sonicated, cavitation bubbles are formed. During the collapse of these bubbles high intensity hydraulic shocks are generated, which initiate the disintegration of liquid film and cause the direct ejection of droplets. The capillary wave hypothesis assumes the liquid capillary waves are composed of crests and troughs. Atomization takes place when unstable oscillations tear the crests (peaks) of surface capillary waves away from the bulk liquid. As a result, droplets are produced at the crests whose size is proportional to wavelength. Capillary wavelength decreases with increasing frequency of ultrasound and thereby producing fine droplets at higher frequency. Bouguslavskii and Eknadiosyants [2.19] combined these two theories to propose a conjunction theory according to which the periodic hydraulic shock from cavitation disturbances interacts with finite amplitude capillary waves and excite them to form droplets.

The mist then passes through a quartz tube for pyrolysis. To transport the mist

droplets through the quartz tube, ambient pressure carrier gas is used. The quartz

tube is placed in a tubular furnace. The droplets when transported into a tubular

reactor under the pyrolysis condition yield one particle per drop. Inside the furnace

the solvent evaporates and intraparticle reactions occur that form the product material.

The spherical nonagglomerated powder with a narrow size distribution is then

collected. The variables affecting the particle morphology are drying rate of droplets,

pyrolysis temperature, residence time, and the properties of the starting materials.

Composition of the final particles is determined by the ratio between reactants

dissolved in the precursor solution. The average size and size distribution roughly

depend on the size of the atomized droplets and the precursor concentrations in the

starting solution. Properties of precursors, carrier gas flow rate (i.e., residence time in

the hot zone) and temperature will mainly affect the morphology of particles and their

extent of agglomeration, as seen in **Figure 2.6**.
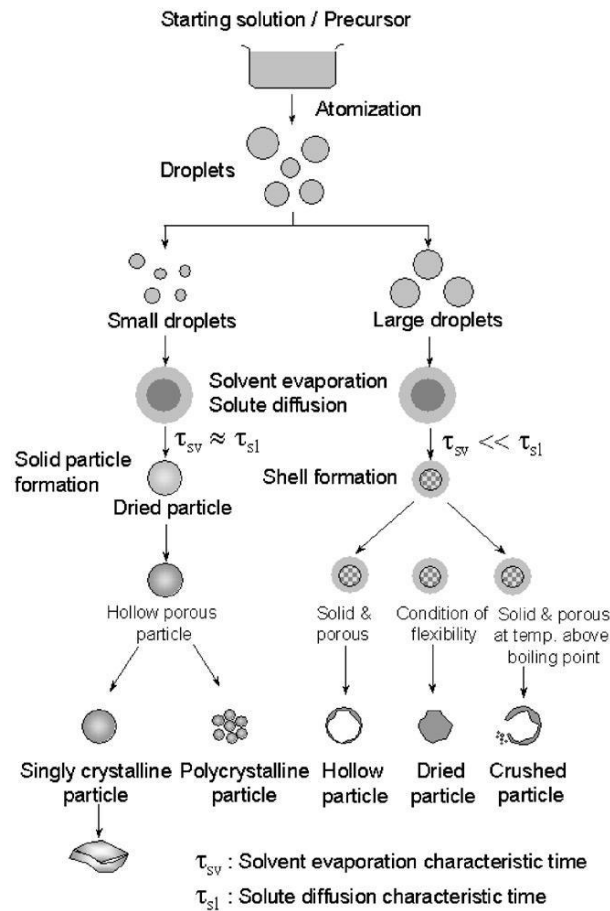
Figure 2.6 Morphology of particles prepared by spray pyrolysis [2.20]

Spray pyrolysis offers several advantages over conventional material processing techniques. The main advantage is the high purity of the product powder, which is dependent only on the precursor solution purity. Additionally, particles produced by spray pyrolysis are more uniform in size and composition, since the reaction is confined to a micrometer scale (within the droplet). Also, multicomponent materials are easily made by spray pyrolysis as each droplet contains precursors in the same stoichiometry as desired in the product. The relative simplicity of the process and continuous nature has allowed scale-up to ton quantities. Interesting particle

23

morphologies, including hollow particles can form when a solute concentration gradient is created during evaporation. The solute precipitates initially at the more highly supersaturated surface if sufficient time is unavailable for solute diffusion in the droplet. If the shell that is formed is impermeable to solvent, the pressure builds within the particle upon further heating and fragments can result. On the other hand, factors that promote dense solid particles formation, include high-solubility precursors, low evaporation rates, small droplet sizes, low solution concentrations, long residence times, and precursors that form permeable salts. For industrial purposes, low solution concentrations and long residence times are impractical, thus the choice of precursor with the desired physical properties is an important parameter for morphological control. [2.21]

Under the assumption that the prepared particle is dense, the average particle size can be calculated by the following equation:

$$D_p = D_O \left[\frac{C\ MW}{\rho_{solid}} \right]^{1/3} = \propto C^{1/3} \qquad (2.6)$$

where D_p is the final obtained particle size, MW the molecular weight of particle, C the concentration of precursor, ρ_{solid} the density of solid, and D_0 is the droplet size. Thus, the size of the particles is easily controlled by the concentration of salt solution.

The mean diameter of the aerosol droplets decreases with increase in the ultrasound frequency according to the relationship:

$$D_O = 0.34 \left[\frac{8\pi\gamma}{\rho f^2} \right]^{1/3} \qquad (2.7)$$

where 0.34 is an experimentally determined coefficient, γ is the solution surface tension (dyne cm^{-1}), ρ precursor density (g ml^{-1}), and f is the frequency of the ultrasound (Hz).

Because the above equation is not dependent on viscosity, in contrast to what is observed experimentally, Rajan and Pandit proposed an empirical correlation considering the dependence on all physicochemical properties of the liquid atomized: [2.22]

$$D_O = constant\ (f)^{-0.66}(Q)^{0.207}(\gamma)^{0.11}(\rho)^{-0.274}(\eta)^{0.166}\left(\frac{Power}{Area}\right)^{-0.4} \qquad (2.8)$$

where Q is the volumetric flow rate of liquid (m^3 s^{-1}) and η is the liquid viscosity (cP).

Another important property to be considered in industrial applications is the atomization efficiency. Though atomization efficiency can be increased by using multiple transducers, it is also affected by atomization power, precursor temperature, and carrier gas flow rates according to Wang et. al. [2.23]

In summary, by using an aerosol synthesis process, spherical, submicrometer- to micrometer-size particles with a unique, porous morphology can be obtained. The size, shape, and porous structure of the powders produced by spray-pyrolysis are considered superior to those produced by solid-state reactions and wet-chemistry processes. The materials from spray pyrolysis have high consistency in different batches and can preserve the stoichiometry of the material. The intraparticle and interparticle composition of the powders is also uniform.

References

[2.1] Tarascon J.M., Armand M. *Nature*, 414 (**2001**) 359.

[2.2] Tarascon J.M., Armand M. *Nature*, 451 (**2008**) 652.

[2.3] Rotem M., Amalraj S.F., Leifer N., Jacob D., Aurbach D., J. Mater. Chem., 21 (**2011**) 9938.

[2.4] Fujimoto H., Tokumitsu K., Mabuchi A., Chinnasamy N., Kasuh T., J. Power Sources 195 (**2010**) 7452.

[2.5] Meunier V., Kephart J., Roland C., Bernholc J., Phys. Rev. Lett. 88 (**2002**) 075506.

[2.6] Hou J., Shao Y., Ellis M.W., Moore R.B., Yi B., Phys. Chem. Chem. Phys. 13 (**2011**) 15384.

[2.7] Chen Z., Belharouak I., Sun Y.K., Amine K., Adv. Funct. Mater. 23 (**2013**) 959.

[2.8] Szczech J.R., Jin S., Energy Environ. Sci. 4 (**2011**) 56.

[2.9] Rudawski N.G., Yates B.R., Holzworth M.R., Jones K.S., Elliman R.G., Volinsky A.A., J. Power Sources 223 (**2013**) 336.

[2.10] Bruce P.G., Scrosati B., Tarascon J.-M., Angew. Chem. Int. Ed. 47 (**2008**) 2930.

[2.11] Park C.-M., Kim J.-H., Kim H., Sohn H.-J., Chem. Soc. Rev. 39 (**2010**) 3115.

[2.12] Wang Z., Zhou L., Lou X.W., Adv. Mater. 24 (**2012**) 1903.

[2.13] Yang J., Takeda Y., Imanishi N., Capiglia C., Xie J.Y., Yamamoto O., Solid State Ionics 152 (**2002**) 125.

[2.14] Jiang J., Li Y., Liu J., Huang X., Yuan C., Lou X.W., Adv. Mater. 24 (**2012**) 5166.

[2.15] Lai C.-H., Lu M.-Y., Chen L.-J., J. Mater. Chem. 22 (**2012**) 19.

[2.16] Wenzel S., Hara T., Janek J., Adelhelm P., *Energy Environ. Sci.* 4 (**2011**) 3342.

[2.17] Palomares V., Casas-Cabanas M., Castillo-Martínez E., Han M. H., Rojo T.*, Energy Environ. Sci.*, 6 (**2013**) 2312.

[2.18] Dunn B., Kamath H., Tarascon J.M., *Science* 334 (**2011**) 928.

[2.19] Bouguslavskii Y., Eknadiosyants O., Soviet Phys. Acoust. 15 (**1969**) 14.

[2.20] Zhang, L. "Preparation of Multi-component Ceramic Nanoparticles." Literature Review. Center for Industrial Sensors and Measurements Department Materials Science & Engineering Group Inorganic Materials Science, Ohio State University, **2004**.

[2.21] Gurav A., Kodas T., Pluym T., Xiong Y., Aerosol Sci. and Tech., 19.4 (**1993**) 411.

[2.22] Ranjan R., Pandit A., Ultrasonics 39 (**2001)** 235.

[2.23] Wang W., Purwanto A., Lenggoro I., Okuyama K., Chang H., Jang H., Industrial & Engineering Chem. Research 47.5 (**2008**) 1650.

Chapter 3: 5V Spinel for LIB Cathodes

3.1 Introduction

Lithium-ion batteries are the technology of choice for future hybrid electric and full electric vehicles due to their high energy density. Currently $LiCoO_2$ is the most widely used cathode material in commercial lithium-ion batteries. However, due to the economical and environmental issues associated with $LiCoO_2$ low cost and environmentally friendly alternatives are being developed. One such alternative is the spinel $LiMn_2O_4$ material, which has become a promising cathode for next generation lithium-ion batteries because of its high voltage (4.7 V vs. Li), acceptable stability, and good cycling performance.[3.1-3.4] The isotropic spinel structure provides a 3-D network for lithium-ion diffusion, thus this material is suitable for fast lithium insertion and deinsertion reactions (i.e. improved kinetics). However, the material suffers from poor cycling behavior, especially at elevated temperature. In $LiMn_2O_4$, the average valence state of Mn is 3.5 due to the presence of an equal amount of Mn^{4+} and Mn^{3+}. The Mn^{3+} concentration in the spinel $LiMn_2O_4$ is large enough to induce the Jahn-Teller distortion and consequently the capacity fading. In an effort to overcome this problem, many research groups have investigated the partial substitution of Mn for other transition metals to form $LiM_xMn_{2-x}O_4$ (M=Co,Cr,Ni,Fe,Cu,etc.).[3.5-3.11] During the course of intensive research it was found that a Ni-doped spinel oxide $LiNi_{0.5}Mn_{1.5}O_4$ is among the most promising because of its good cycling behavior and relatively high capacity (147 mAh/g) [3.12-3.15] due to the elimination of the Jahn-Teller disordering of Mn^{3+} since Mn is mainly tetravalent and

the $Ni^{4+/2+}$ redox couple drives the reaction across the two electrodes. This spinel has two different crystal structures of the space groups of Fd3m (non-stoichiometric disordered $LiNi_{0.5}Mn_{1.5}O_{4-\delta}$) in which Mn ions are present in mainly Mn^{4+} with little Mn^{3+} and $P4_332$ (stoichiometric ordered $LiNi_{0.5}Mn_{1.5}O_4$) in which Mn ions are present only in Mn^{4+}. The non-stoichiometric $LiNi_{0.5}Mn_{1.5}O_{4-\delta}$ has face centered cubic spinel structure, like pure spinel $LiMn_2O_4$, the Ni and Mn, Li, and O atoms occupy the 16d octahedral sites, 8a tetrahedral sites and 32e sites, respectively. In this structure, Ni and Mn atoms are randomly distributed in the 16d octahedral sites. In contrast, the stoichiometric $LiNi_{0.5}Mn_{1.5}O_4$ has the primitive simple cubic structure in which the Ni, Mn, and Li atoms are occupied in the 4a, 12d, and 4c sites with O ions occupying the 8c and 24e sites. In this structure Ni and Mn atoms are ordered regularly.[3.16] The disordered spinel structure was found to exhibit better electrochemical performance than the ordered structure.[3.17] The diffusion path of lithium in the disordered spinel is shown in **Figure 3.1**.[3.18]
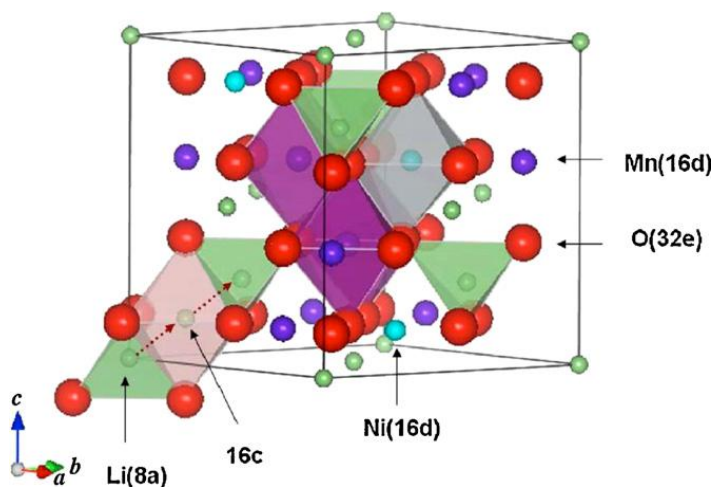
Figure 3.1 Spinel structure of $LiNi_{0.5}Mn_{1.5}O_4$ (Fd3m) showing diffusion path of lithium

In this chapter, we report the improved electrochemical performance of

$LiNi_{0.5}Mn_{1.5}O_4$ synthesized by ultrasonic spray pyrolysis (USP) for application as the

positive electrode in lithium-ion batteries. In a typical process, ultrasonic waves are

applied to precursor solution in order to create an aerosol that is then swept through a

furnace by a carrier gas. Upon heating, the precursor solvent evaporates and

precursors decompose resulting in a product with a generally spherical shape. Since

each droplet in the aerosol is an individual microreactor, the particle size,

composition and structure can be controlled. USP has been widely used in industry

for large-scale production of particles.

3.2 Experimental

3.2.1 Ultrasonic Spray Pyrolysis Reactor System

The ultrasonic spray pyrolysis (USP) reactor system is shown in **Figure 3.2**. The

system is composed of a precursor solution reservoir, an ultrasonic droplet generator

(1.7 MHz), two tube furnaces in series, a quartz tube reactor (diameter 22/25 mm x

810 mm) , and a filtration system for particle collection. Spray pyrolysis enables the

production of spherical particles with compositional homogeneity with respect to the

precursor solution. A frequency generator device is used to form ultrasonic vibrations,

thereby creating fine aerosol droplets with stoichiometric composition. The fine

aerosol is transported via carrier gas into a tubular furnace at a given temperature.

Once in the furnace, processes of diffusion, dehydration, and decomposition occur

simultaneously to form nanoparticles of controlled size, morphology, and

composition.

Figure 3.2 Schematic of spray pyrolysis process

3.2.2 Material Synthesis

The synthesis of $LiNi_{0.5}Mn_{1.5}O_4$ was carried out by mixing the stoichiometric amount of lithium nitrate, nickel nitrate hexahydrate, and manganese nitrate tetrahydrate dissolved in water along with 50 wt% sucrose. The total species precursor molar concentration was 0.35 M, and the spray pyrolysis temperature was 500 ˚C, while nitrogen carrier gas and quench gas flow rates were held constant at 3 lpm and 10 lpm, respectively. 500 ˚C was chosen as the optimum pyrolysis temperature, which corresponds to a residence time of approximately 3 seconds. Particles were collected on a polytetrafluoroethylene (PTFE) filter using a brush. The as prepared materials were then annealed at 800 ˚C for 5 hours in air to obtain the desired phase.

3.2.3 Cathode Preparation

Electrochemical performance of $LiNi_{0.5}Mn_{1.5}O_4$ was tested in a coin cell using lithium metal as the counter electrode and 1 M $LiPF_6$ in a mixture of fluoroethylene carbonate-dimethyl carbonate (FEC/DMC, 1:1 by volume) as the electrolyte and Celgard®3501 (Celgard LLC Corp., USA) as the separator. $LiNi_{0.5}Mn_{1.5}O_4$ cathodes consisted of 80 wt% $LiNi_{0.5}Mn_{1.5}O_4$, 10 wt% acetylene black, and 10 wt% sodium alginate, which were mixed with water and pasted on Al foil, and then dried at 100 °C in vacuum. The active material loading is 0.5-0.6 mg cm^{-2}. The charge/discharge behavior was tested using an ArbinBT2000 workstation (Arbin Instruments, TX, USA). Rate capability was examined by charging and discharging at different rates (1C= 147 mA g^{-1}).

3.2.4 Cathode Characterization

Structural studies were performed by x-ray diffraction (XRD) on D8 Advance with LynxEye and SolX (Bruker AXS, WI, USA) using CuKα radiation, scanning electron microscopy on a Hitachi (Tokyo, Japan) SU- 70 HR-SEM with FFT images.

3.3 Results and Discussion

3.3.1 Structural and Morphological Analysis

Post heat-treatment is necessary to remove any impurities and reduce the oxygen defect. Annealing is also crucial to optimize the crystal structure of the powder. As

previously mentioned, $LiNi_{0.5}Mn_{1.5}O_4$ can have two different space group structures: disordered *Fd3m* with weak oxygen deficiency, or ordered *P4₃32* space group with no oxygen deficiency, and these structures are highly dependent on the heat treatment temperature. A high temperature, above 600 °C, tends to favor the disordered structure. XRD pattern of the annealed sample (**Figure 3.3**) demonstrates that single phase disordered $LiNi_{0.5}Mn_{1.5}O_4$ is obtained after heat treatment.
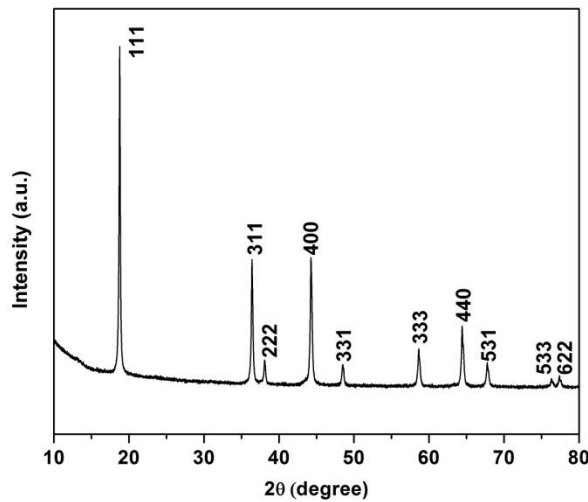
Figure 3.3 XRD full-pattern fitting of $LiNi_{0.5}Mn_{1.5}O_4$ sample after heat treatment

Figure 3.4 shows typical particle morphology after annealing in air at 800 ˚C for 5 hours. $LiNi_{0.5}Mn_{1.5}O_4$ particles prepared using USP are spherical in shape with average particle size of 1.2 um (ranging from 700 nm to 1.7 µm). After heat treatment, the particles maintain the spherical morphology.
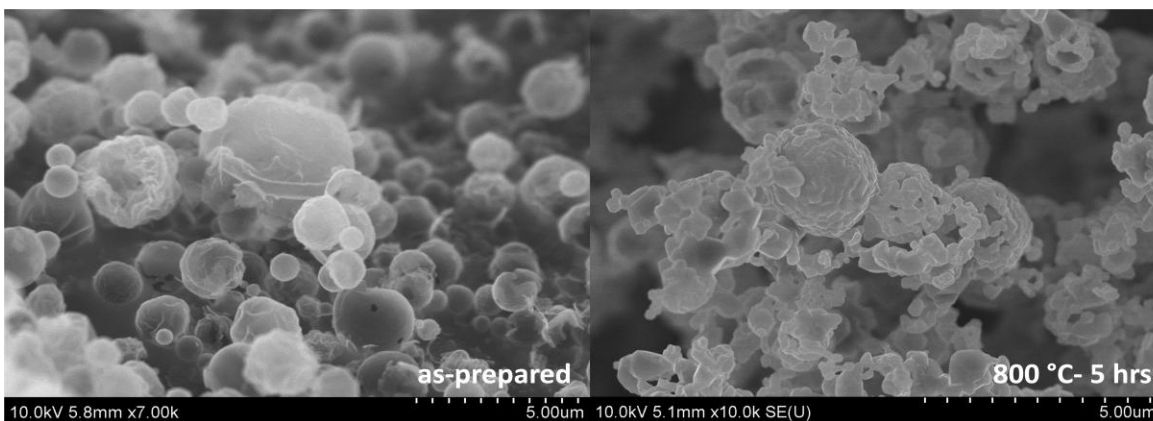
Figure 3.4 SEM images of $LiNi_{0.5}Mn_{1.5}O_4$ particles prepared by USP before and after heat treatment

3.3.2 Electrochemical Characterization

Galvanostatic charge/discharge performance of $LiNi_{0.5}Mn_{1.5}O_4$ cathode materials was tested in a voltage window of 3.5-5.0 V. **Figure 3.5** shows typical voltage profiles of $LiNi_{0.5}Mn_{1.5}O_4$ during the first 100 cycles at a rate of 0.1 C. Two distinct plateaus are observed near 4.7 V corresponding to a Ni^{2+}/Ni^{4+} redox couple. A slight plateau is also seen around 4.0 V during both charge and discharge. This 4 V plateau is attributed to the $Mn^{3+}/^{4+}$ redox couple. For the ordered spinel structure (*P4$_3$32* space group), the average oxidation state of the Mn is 4+. For the disordered *Fd*3*m* structure, $LiNi_{0.5}Mn_{1.5}O_4$ remains as an oxygen-deficient spinel, which results in the average oxidation state of Mn to be slightly lower than 4+. This means a small portion of the Mn appears as 3+ instead of 4+ and the $Mn^{3+/4+}$ redox reaction, as seen in spinel $LiMn_2O_4$, will also be seen here at 4 V.
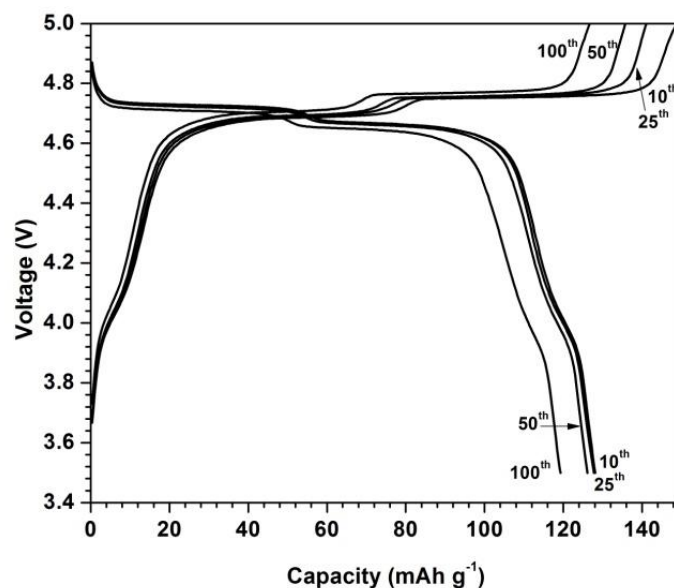
Figure 3.5 Galvanostatic charge/discharge curves of $LiNi_{0.5}Mn_{1.5}O_4$ cell cycled at a rate of 0.1 C

$LiNi_{0.5}Mn_{1.5}O_4$ demonstrates exceptional cycling stability as seen in **Figure 3.6**. $LiNi_{0.5}Mn_{1.5}O_4$, when cycled at 0.1C can deliver approximately 125 mAh g^{-1} and retain 96% of capacity after 100 cycles. The coulombic efficiency for the first cycle is low, due to the SEI layer formation. When the cycle test continues, the coulombic efficiency increases rapidly and is stabilized at 95%.
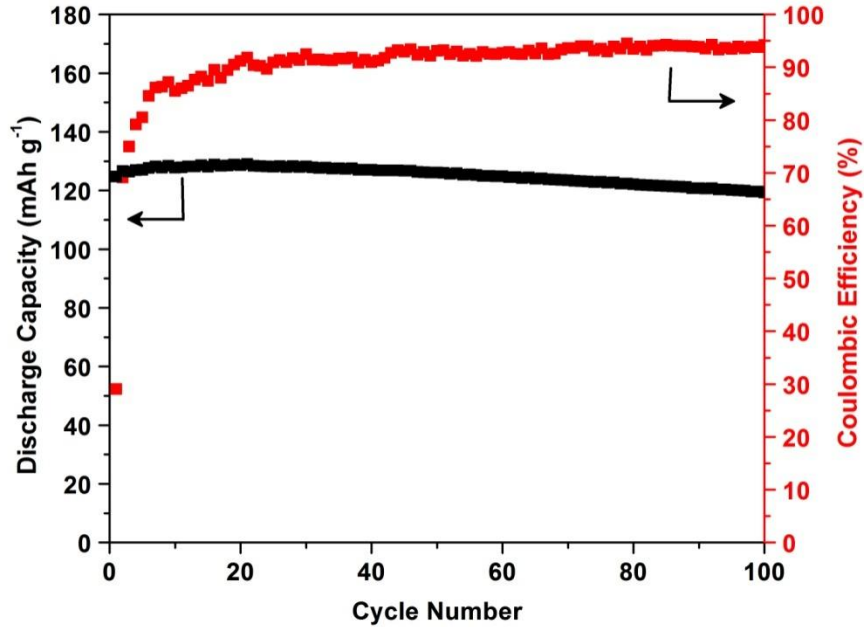
Figure 3.6 Capacity retention of $LiNi_{0.5}Mn_{1.5}O_4$ cycled at a rate of 0.1 C

The $LiNi_{0.5}Mn_{1.5}O_4$ cathodes were subjected to rate testing protocol in which the cells were both charged and discharged at the same high rates in the voltage window of 3.5-5.0 V. As shown in **Figure 3.7**, under this stringent condition, $LiNi_{0.5}Mn_{1.5}O_4$ can deliver approximately 99 mAh g^{-1} at 2C, which is 85% of initial capacity. After returning the current density to 0.1C, the capacity of $LiNi_{0.5}Mn_{1.5}O_4$ electrode is nearly identical to the capacity at the first few cycles at 0.1C rate. Therefore, no irreversible capacity loss occurred. The discharge curves at the various C-rates are given in **Figure 3.8**. The operating voltage drops slightly from 4.7 V at 0.1C to 4.6 V at 2C due to kinetic limitations
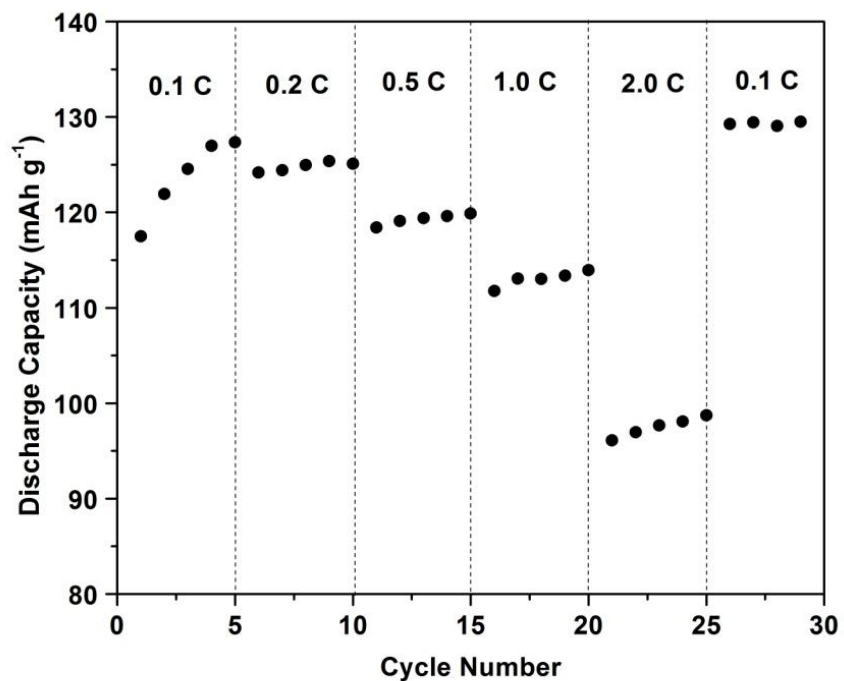
Figure 3.7 Rate capability of LiNi$_{0.5}$Mn$_{1.5}$O$_4$
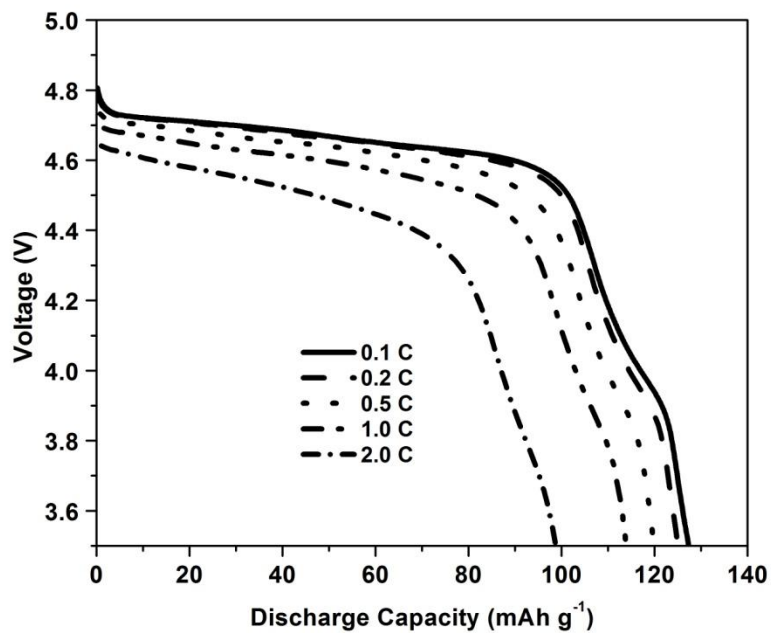
Figure 3.8 Discharge curves of LiNi$_{0.5}$Mn$_{1.5}$O$_4$ at various C-rates

Because of the excellent stability of the material at a low C-rate (0.1C), much longer charge/discharge cycles were tested for $LiNi_{0.5}Mn_{1.5}O_4$ cathodes. The cell was subjected to a high rate of 1C as shown in **Figure 3.9**. The initial capacity of $LiNi_{0.5}Mn_{1.5}O_4$ is 114 mAh g^{-1} at 1C. After 100 cycles, the capacity decreases to 108 mAh g^{-1} which corresponds to capacity retention of 95%. The coulombic efficiency increases at the elevated C rate, exceeding 99%. This work represents a significant advance in $LiNi_{0.5}Mn_{1.5}O_4$ cathode materials for Li-ion batteries.
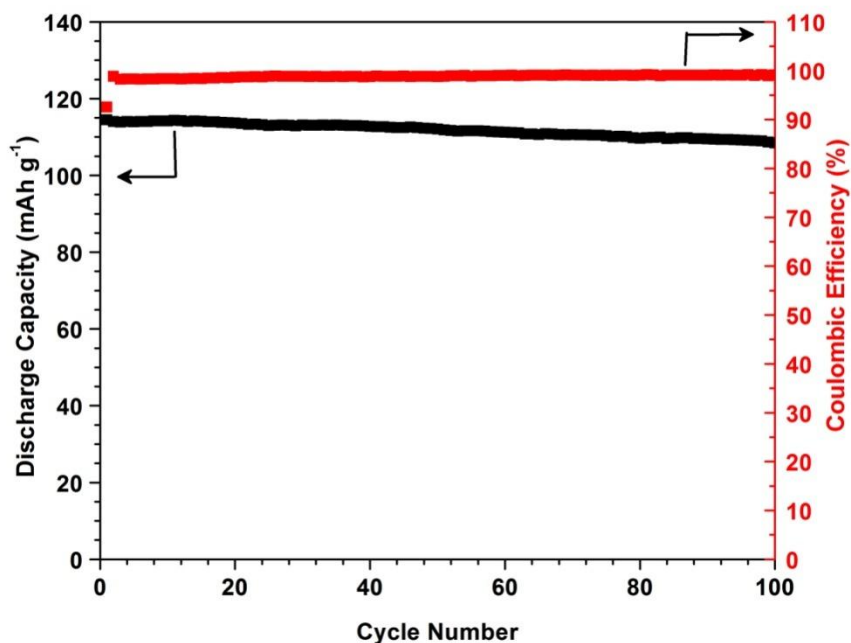
Figure 3.9 Capacity retention of $LiNi_{0.5}Mn_{1.5}O_4$ cycled at a rate of 1.0 C

3.4 Conclusion

In summary, $LiNi_{0.5}Mn_{1.5}O_4$ particles were synthesized using an USP process. The XRD spectrum showed that the annealed material was a single phase spinel with the disordered Fd3m structure. The $LiNi_{0.5}Mn_{1.5}O_4$ cathodes can deliver 125 mAh g^{-1}

capacity at a low rate of 0.1C, and 114 mAh g^{-1} at 1C, and maintains 85% of capacity at 2C. After 100 cycles at 1C, $LiNi_{0.5}Mn_{1.5}O_4$ cathodes can still provide 108 mAh g^{-1}, which is 95% of initial capacity. From these results, ultrasonic spray pyrolysis has the potential to produce valuable energy storage materials with excellent electrochemical properties.

References

[3.1] Wu, Yongmin, Zhenhai Wen, Hongbin Feng, and Jinghong Li. *Small* 8.6 (**2012**) 858.

[3.2] Xi, Liu Jiang, Hong-En Wang, Zhou Guang Lu, Shi Liu Yang, Ru Guang Ma, Jian Qiu Deng, and C.Y. Chung. *J. Power Sources* 198 (**2012**) 251.

[3.3] Cabana, J., T. Valdessolis, M. Palacin, J. Orosole, A. Fuertes, G. Marban, and A. Fuertes. *J. Power Sources* 166.2 (**2007**) 492.

[3.4] Ding, Yuan-Li, Jian Xie, Gao-Shao Cao, Tie-Jun Zhu, Hong-Ming Yu, and Xin-Bing Zhao. *Adv. Funct. Mater* 21 (**2011**) 348.

[3.5] Huang, Xingkang, Min Lin, Qingsong Tong, Xiuhua Li, Ying Ruan, and Yong Yang. *J. Power Sources* 202 (**2012**) 352.

[3.6] Moon, Hee-Soo, and Jong-Wan Park. *J. Power Sources* 119-121 (**2003**) 717.

[3.7] Sigala, C., D. Guyomard, A. Verbaere, Y. Piffard, and M. Tournoux. *Solid State Ionics* 81.3-4 (**1995**) 167.

[3.8] Gu, Xin, Xiaowei Li, Liqiang Xu, Huayun Xu, Jian Yang, and Yitai Qian. *Int. J. Electrochem. Sci* 7 (**2012**) 2504.

[3.9] Amine, K., H. Tukamoto, H. Yasuda, and Y. Fujita. *J. Power Sources* 68 (**1997**) 604.

[3.10] Shigemura, H., H. Sakaebe, H. Kageyama, H. Kobayashi, A. R. West, R. Kanno, S. Morimoto, S. Nasu, and M. Tabuchi. *J. Electrochem. Soc.* 148.7 (**2001**) A730.

[3.11] Eli, Yair Ein, W. F. Howard, Jr., Sharon H. Lu, Sanjeer Mukerjee, James McBreen, John T. Vaughey, and Michael M. Thackeray. *J. Electrochem. Soc.* 145.4 (**1998**) 1238.

[3.12] Zhou, Liang, Dongyuan Zhao, and XiongWen Lou. *Angew. Chem. Int. Ed.* 51 (**2012**) 239.

[3.13] Akao, Shinsuke, Motofumi Yamada, Takayuki Kodera, Kenichi Myoujin, and Takashi Ogihara. *Advances in Materials Science and Engineering* 2011 (**2011**) 1.

[3.14] Zhang, Minghao, Jun Wang, Yonggao Xia, and Zhaoping Liu. *J. Alloys and Compounds* 518 (**2012**) 68.

[3.15] Yi, Ting-Feng, and Xin-Guo Hu. *J. Power Sources* 167.1 (**2007**) 185.

[3.16] Santhanam, R., and B. Rambabu. *J. Power Sources* 195 (**2010**) 5442.

[3.17] Kim, J.-H., S.-T. Myung, C. S. Yoon, S. G. Kang, and Y.-K. Sun. *Chem. Mater.* 35.21 (**2004**) 906.

[3.18] Xia, H., Y. S. Meng, L. Lu, and G. Ceder. *J. Electrochem. Soc.* 154.8 (**2007**) A737.

Chapter 4: $Li_{1.2}Mn_{0.54}Co_{0.13}Ni_{0.13}O_2$ for LIB Cathodes

4.1 Introduction

Lithium-ion batteries are used as energy storage devices in portable devices such as cell phones and laptop computers and in electric vehicles due to their high energy density. However, only half of the theoretical capacity (140 mAh g^{-1}) of the conventional layered $LiCoO_2$ cathode could be used in practical cells due to structural and chemical instabilities at deep charge.[4.1] Recently, solid solutions between layered $LiMO_2$ (M = Mn, Co, and Ni) and layered Li_2MnO_3 have become attractive as cathodes for lithium-ion batteries since they exhibit much higher capacities (> 250 mAh g^{-1}) compared to commercially available cathodes, such as $LiCoO_2$ or $LiMn_2O_4$.[4.2] Solid solution cathodes with more than one lithium per formula unit are commonly referred to as lithium-rich layered oxides. The remarkably high capacity achieved with this class of solid solution cathodes is due to an irreversible loss of oxygen and extraction of octahedral Li^+ from the layered lattice during first charge with a net loss of Li_2O, occurring beyond 4.5 V. Following the first discharge process, a fraction of the insulating Li_2MnO_3 component is transformed from a layered structure to a spinel-like region. This phase transformation can reduce the rate of free migration of Li ions, leading to poor rate capability.[4.3] Li_2MnO_3 is not electrochemically active since the oxidation state of Mn is +4 and it cannot increase to +5 when Li is extracted from the structure. Upon discharge, Mn ions are reduced to +3 states and then oxidized to +4 valence state in subsequent charging cycle. The

capacity is increased due to the excess lithium ion in transition metal site and occurrence of both Mn^{3+}/Mn^{4+} along with the redox couples Ni^{2+}/Ni^{4+} and Co^{3+}/Co^{4+} in these integrated cathodes.[4.4] The synthesis route employed will deeply affect the morphology and particle size. Many methods have been used to synthesize xLi_2MnO_3-$(1-x)LiMO_2$ (M=Mn,Co,Ni), including coprecipitation[4.5], microwave heating[4.6], sol-gel[4.7], ion-exchange[4.8], solid reaction[4.9], and combustion processing.[4.10]

In this chapter, we report the improved electrochemical performance of xLi_2MnO_3-$(1-x)LiMn_{0.33}Co_{0.33}Ni_{0.33}O_2$ (x=0.5), equivalently $Li_{1.2}Mn_{0.54}Co_{0.13}Ni_{0.13}O_2$, synthesized by ultrasonic spray pyrolysis (USP) for application as the positive electrode in lithium-ion batteries.

4.2 Experimental

4.2.1 Ultrasonic Spray Pyrolysis Reactor System

The ultrasonic spray pyrolysis (USP) reactor system shown in **Figure 3.2** is composed of a precursor solution reservoir, an ultrasonic droplet generator (1.7 MHz), two tube furnaces in series, a quartz tube reactor (diameter 22/25 mm x 810 mm) , and a filtration system for particle collection. Spray pyrolysis enables the production of spherical particles with compositional homogeneity with respect to the precursor solution. A frequency generator device is used to form ultrasonic vibrations, thereby creating fine aerosol droplets with stoichiometric composition. The fine aerosol is transported via carrier gas into a tubular furnace at a given temperature. Once in the furnace, processes of diffusion, dehydration, and decomposition occur

simultaneously to form nanoparticles of controlled size, morphology, and composition.

4.2.2 Material Synthesis

The synthesis of $Li_{1.2}Mn_{0.54}Co_{0.13}Ni_{0.13}O_2$ was carried out by mixing the stoichiometric amount of lithium nitrate, manganese nitrate tetrahydrate, cobalt nitrate hexahydrate, and nickel nitrate hexahydrate dissolved in water along with 70 wt% sucrose. The total species precursor molar concentration was 0.40 M, and the spray pyrolysis temperature was 600 ˚C, while nitrogen carrier gas and quench gas flow rates were held constant at 3 lpm and 10 lpm, respectively. 600 ˚C was chosen as the optimum pyrolysis temperature, which corresponds to a residence time of approximately 3 seconds. Particles were collected on a polytetrafluoroethylene (PTFE) filter using a brush. The as prepared materials were then annealed at 600, 700, or 800 ˚C for 6 hours in air to obtain the desired phase.

4.2.3 Cathode Preparation

Electrochemical performance of $Li_{1.2}Mn_{0.54}Co_{0.13}Ni_{0.13}O_2$ was tested in a coin cell using lithium metal as the counter electrode and 1 M $LiPF_6$ in a mixture of fluoroethylene carbonate-dimethyl carbonate (FEC/DMC, 1:1 by volume) as the electrolyte and Celgard®3501 (Celgard LLC Corp., USA) as the separator. $Li_{1.2}Mn_{0.54}Co_{0.13}Ni_{0.13}O_2$ cathodes consisted of 80 wt% $Li_{1.2}Mn_{0.54}Co_{0.13}Ni_{0.13}O_2$, 10 wt% acetylene black, and 10 wt% sodium alginate, which were mixed with water and pasted on Al foil, and then dried at 100 °C in vacuum. The active material loading is

0.6-0.8 mg cm^{-2}. The charge/discharge behavior was tested using an ArbinBT2000 workstation (Arbin Instruments, TX, USA). The charge/discharge characteristics of the samples were measured by cycling them in the 2.0–4.8 V potential range at a constant current density of 20 mA g^{-1}.

4.2.4 Cathode Characterization

Structural studies were performed by x-ray diffraction (XRD) on D8 Advance with LynxEye and SolX (Bruker AXS, WI, USA) using CuKα radiation and scanning electron microscopy on a Hitachi (Tokyo, Japan) SU- 70 HR-SEM with FFT images.

4.3 Results and Discussion

4.3.1 Structural and Morphological Analysis

XRD pattern of the annealed samples (**Figure 4.1**) demonstrates that single phase $Li_{1.2}Mn_{0.54}Co_{0.13}Ni_{0.13}O_2$ is obtained after heat treatment at temperatures as low as 600 °C. All the XRD spectrums of composite materials show a broad peak between 20-25° indicating the superlattice ordering of Li and Mn cations in transition metal layers for Li_2MnO_3. The 018 and 110 peaks near 65° start to split as the x value increases due to the growing of the parent hexagonal cells with R3m symmetry and formation of a more compact structure. The Li_2MnO_3 structure plays a significant role in maintaining structural stability and consequently the electrochemical properties of the composite materials.
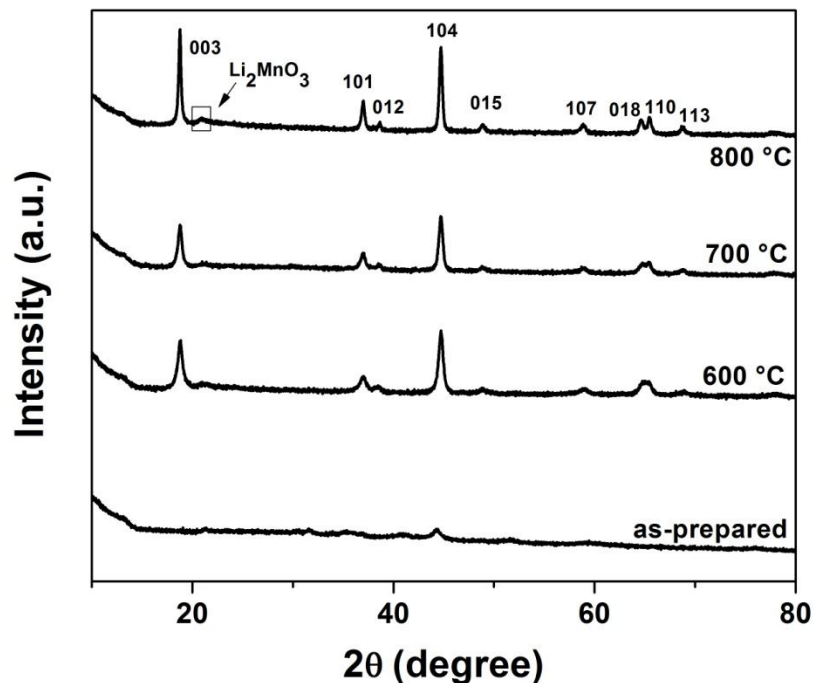
Figure 4.1 XRD full-pattern fitting of $Li_{1.2}Mn_{0.54}Co_{0.13}Ni_{0.13}O_2$ sample before and

after heat treatment

Figure 4.2 shows typical particle morphology before and after annealing in air at

600-800 ˚C for 6 hours. $Li_{1.2}Mn_{0.54}Co_{0.13}Ni_{0.13}O_2$ particles prepared using USP are

spherical in shape with average particle size of 1.0 um (ranging from 400 nm to 1.6

µm). The as-prepared powder is nanocrystalline, and shows nano- to mesoporous

morphology. After heat treatment, the particles retain the spherical morphology and

the particles appear to be more porous and coarsened. The heat treatment process is

crucial to refine the crystal structure and grow the crystallites in the materials.

46
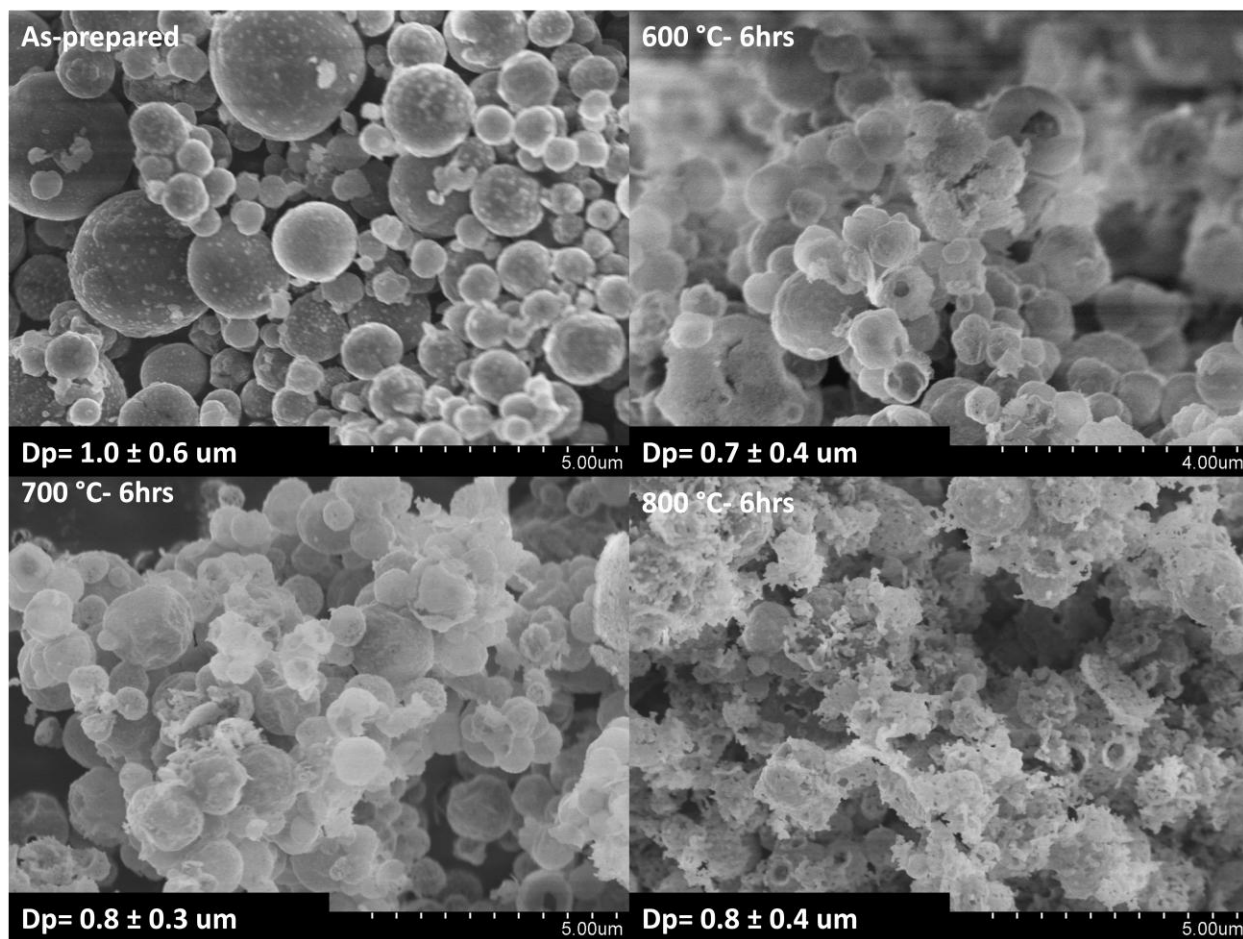
Figure 4.2 SEM images of $Li_{1.2}Mn_{0.54}Co_{0.13}Ni_{0.13}O_2$ particles prepared by USP before

and after heat treatment

4.3.2 Electrochemical Characterization

Galvanostatic charge/discharge performance of $Li_{1.2}Mn_{0.54}Co_{0.13}Ni_{0.13}O_2$ cathode

materials was tested in a voltage window of 2.0-4.8 V. **Figure 4.3** shows typical

voltage profiles of $Li_{1.2}Mn_{0.54}Co_{0.13}Ni_{0.13}O_2$ during the initial cycle at a current density

of 20 mA g^{-1}. The coulombic efficiency for the first cycle is over 80% for all three

heat treated samples. All the cells show a two-step charge profile and a smooth

discharge profile between 2.0 and 4.6 V. The shape of the voltage climb from 3.5 V

47

to 4.5 V is due to the Ni^{2+}/Ni^{4+} redox couple during lithium extraction. At 4.5 V, a voltage plateau appears which is due to the removal of Li and O from Li_2MnO_3. The reactions associated with the two-step charge profile are as follows:

$$LiMO_2 \rightarrow Li^+ + MO_2 + e^- \ (M=Ni_{0.33}Co_{0.33}Mn_{0.33})$$

$$Li_2MnO_3 \rightarrow 2Li^+ + MnO_2 + \tfrac{1}{2} O_2 + 2e^-$$
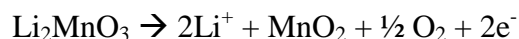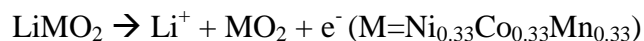
The overall loss in the two-step charge reactions is Li_2O from the Li_2MnO_3, after which the electrochemically active MnO_2 component is formed (see **Figure A.1**).[4.11] The slope of the voltage profile near the end of charge, exceeding 4.7 V, is due to the oxidation of electrolyte, which can provide additional capacity.
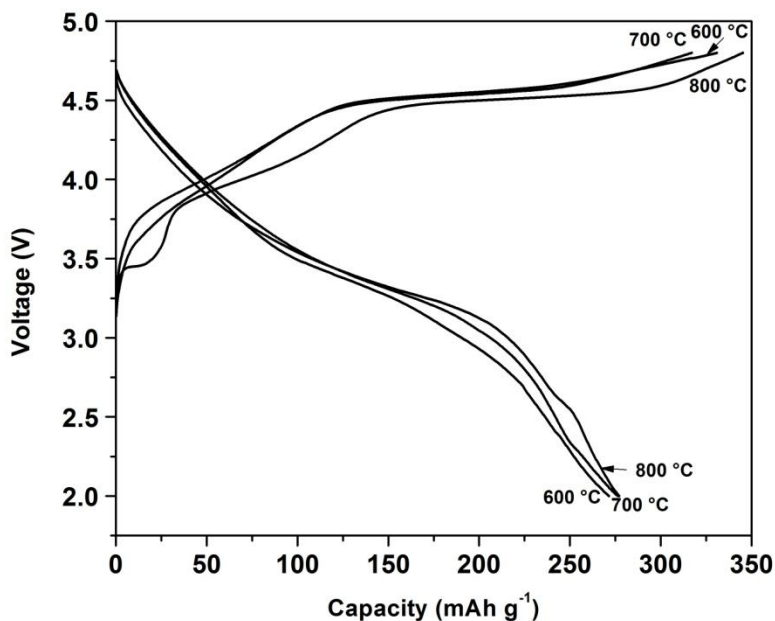
Figure 4.3 Galvanostatic charge/discharge curves of $Li_{1.2}Mn_{0.54}Co_{0.13}Ni_{0.13}O_2$ cells cycled at a current density of 20 mA g^{-1}

$Li_{1.2}Mn_{0.54}Co_{0.13}Ni_{0.13}O_2$ heat treated at 800 °C has the highest initial capacity and
demonstrates good cycling stability. $Li_{1.2}Mn_{0.54}Co_{0.13}Ni_{0.13}O_2$, can deliver
approximately 277 mAh g^{-1} and retain 75% of capacity after 50 cycles. **Figure 4.4**
shows the galvonstatic charge/discharge curves during the first 50 cycles for the
sample heat treated at 800 °C. One possible explanation for the capacity fading could
be the sub-micron primary particle size, which provides a sufficiently large surface
area for side reactions, including dissolution of active species and oxidation of
electrolyte.
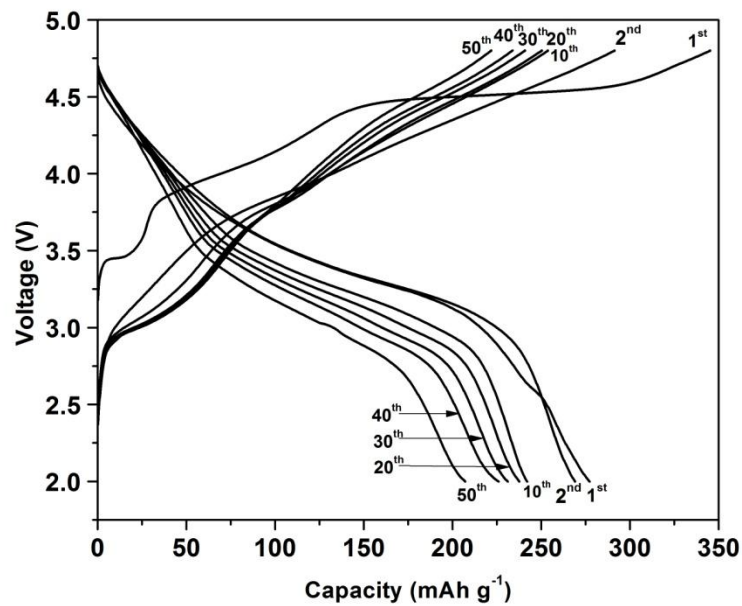
Figure 4.4 Galvanostatic charge/discharge curves of $Li_{1.2}Mn_{0.54}Co_{0.13}Ni_{0.13}O_2$ heat
treated at 800 °C during the first 50 cycles

Figure 4.5 shows the cycling stability of the post treated $Li_{1.2}Mn_{0.54}Co_{0.13}Ni_{0.13}O_2$

cathodes. The sample post treated at 800 °C demonstrates superior cycle life,

retaining 75% of initial capacity after 50 cycles.
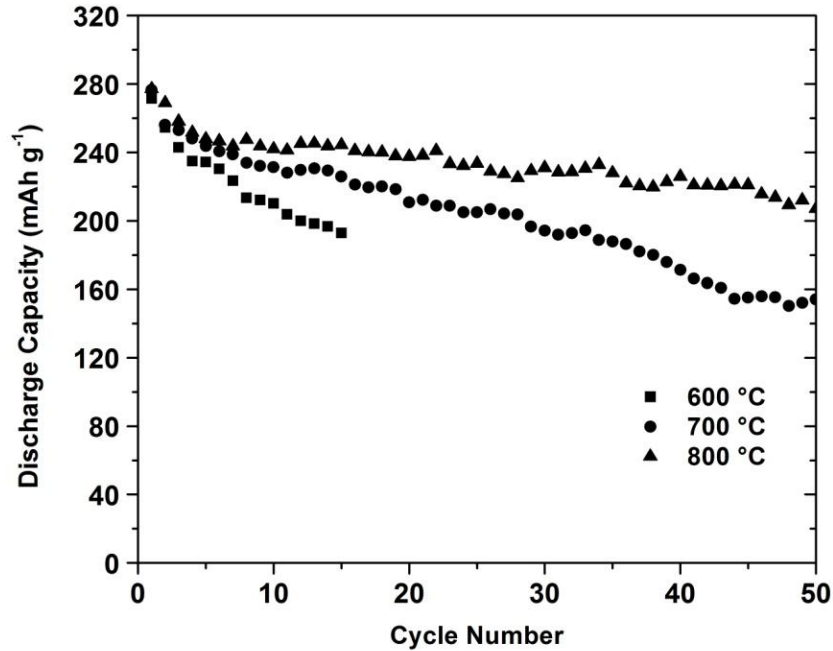
Figure 4.5 Capacity retention of $Li_{1.2}Mn_{0.54}Co_{0.13}Ni_{0.13}O_2$ heat treated at various

temperatures

4.4 Conclusion

In summary, $Li_{1.2}Mn_{0.54}Co_{0.13}Ni_{0.13}O_2$ particles were synthesized using an USP

process with post annealing (600-800 °C for 6 hrs). All the powders produced are

spherical in shape and submicron in size. According to the XRD spectra,

electrochemically inactive Li_2MnO_3 is observed for the composite material. During

the initial charge, the composite materials exhibit a smooth increase in voltage due to

the $Ni^{2+}/^{4+}$ redox couple. A voltage plateau around 4.5 V is due to the electrochemical

extraction of Li_2O from Li_2MnO_3. Among the composites tested,

$Li_{1.2}Mn_{0.54}Co_{0.13}Ni_{0.13}O_2$ cathodes heat treated at 800 °C can deliver a discharge

capacity of 277 mAh g^{-1} at a current density of 20 mA g^{-1} with an initial coulombic

efficiency of 80% and maintains 75% of capacity after 50 cycles.

References

[4.1] Chebaim, R. V., Prado, F., Manthiram, A. *Chem. Mater.* 13 (**2001**) 2951.

[4.2] Kim D., Sandi G., Croy J.R., Gallagher K.G., Kang S.H., Lee E., Slater M.D., Johnson C.S., Thackeray M.M., *J. Electrochem. Soc.* 160.1 (**2013**) A31.

[4.3] Song B., Lai M.O., Lu L., *Electrochim. Acta* 80 (**2012**) 187.

[4.4] Johnson C. S., Kim J. S., Lefief C., Li N., Vaughey J. T., Thackeray M. M., *Electrochem. Commun.*, 6, (**2004**) 1085.

[4.5] Kang S.H., Thackeray M.M., *Electrochem. Commun.* 11 (**2009**) 748.

[4.6] Peng Q.W., Tang Z.Y., Zhang L.Q., Liu X.J., *Mater. Res. Bull.* 44 (**2009**) 2147.

[4.7] Sivaprakash S., Majumder S.B., *Solid State Ionics* 181 (**2010**) 730.

[4.8] Kim D., Kang S.-H., Balasubramanian M., Johnson C.S., *Electrochem. Commun.*12 (**2010**) 1618.

[4.9] Shi S.J., Tu J.P., Tang Y.Y., Yu Y.X., Zhang Y.Q., Wang X.L., *J. Power Sources* 221(**2013**) 300.

[4.10] Haik O., Martha S.K., Sclar H., Samuk-Fromovich Z., Zinigrad E., Markovsky B., Kovacheva D., Saliyski N., Aurbach D., *Thermochim. Acta* 493 (**2009**) 96.

[4.11] Yabuuchi N., Yoshii K., Myung S.T., Nakai I., Komaba S., J. Am. Chem. Soc. 133 (**2011**) 4404.

Chapter 5: Carbon Coated Porous Hollow Na$_2$FePO$_4$F Cathode

5.1 Introduction

The sodium ion battery is a promising alternative to the widely studied lithium ion

battery for smart electric grids that integrate discontinuous renewable energy sources

due to low cost of sodium which is more abundant than Li.[5.1] Since the weight and

footprint requirement for electrical grid storage is less important, the lower energy

density of Na-ion batteries compared to that of lithium ion technology is not an

issue.[5.2] However, Na ions are about 55% larger in radius than Li ions, which makes

it difficult to find a suitable host material to accommodate Na ions and allow

reversible and rapid ion insertion and extraction. Only a few Li-ion battery cathode

materials are suitable for the Na-ion battery. Among them, Na$_2$FePO$_4$F can provide

124 mAh g^{-1} at a very low charge/discharge rate, demonstrating potential as a cathode

material for Na-ion cells. However, it can only provide 12% of 0.1C capacity at 8C

and can maintain the capacity only in 20 charge/discharge cycles.[5.3,5.4] The rate

performance and cycling stability of Na$_2$FePO$_4$F need to be largely improved before

practical application in Na-ion batteries.

A number of methods have been used for enhancing the cycling stability and rate

performance of ion insertion materials. Among them, carbon coating and particle size

reduction are the most common strategies to enhance both the cycling stability and

rate performance of cathode electrodes due to low electronic conductivity and poor

53

ion diffusivity. These two methods have been successfully adapted to Na_2FePO_4F

cathodes to improve the electrochemical performance in Na-ion batteries. The carbon

coated nano-sized C/Na_2FePO_4F cathodes prepared using solid-state reaction showed

promising capacity of 110 mAh g^{-1} at a low rate of 1/20C.[5.4] However, it can deliver

only 50% of 0.05C capacity at 1C and can only be charged/discharged for 20 cycles

even though the particle size of C/Na_2FePO_4F was reduced to 30-200 nm and the

particles were coated with carbon.[5.4] Therefore, reducing particle size and coating

carbon, which are very effective for $LiFePO_4$ in Li-ion batteries, are not sufficient to

enhance the performance of C/Na_2FePO_4F cathodes in Na-ion batteries due to the

large size of Na-ions.

Recently, it was reported that porous materials with porous hollow structure (hollow

spheres, nanotubes) have exceptional rate capability and cycling stability in Li-ion

batteries, even for those materials which experience large volume change (270% for

Si, Sn) during lithiation/delithiation.[5.5,5.6] Hollow and porous spheres offer several

advantages over dense particles, including fast mass transfer and large reaction area,

thus improving the electrochemical reaction kinetics. In addition, the interior void of

hollow spheres can effectively accommodate the volume change, enhancing the

structural stability by releasing the strain[5.6], thus improving the cycling stability.

Conventional methods for fabrication of hollow spheres utilize sacrificial

templates.[5.5,5.6] However, template synthesis methods suffer from high cost and

tedious synthetic procedures, which may prevent their use in large-scale applications.

Ultrasonic spray pyrolysis (USP) is a one-step template-free synthetic method for the

fabrication of hollow structure material.[5.7] In a typical process, ultrasonic waves are applied to precursor solution in order to create an aerosol that is then swept through a furnace by a carrier gas. Upon heating, the precursor solvent evaporates and precursors decompose resulting in a product with a generally spherical shape. If the precursors also generate gas, it would escape from the product spheres to create a hollow structure or porous hollow structure, leaving large cavities and small pores. Since each droplet in the aerosol is an individual microreactor, the particle size, composition and structure can be controlled. USP has been widely used in industry for large scale production of hollow particles.

In this chapter, carbon coated porous hollow C/Na_2FePO_4F spheres with 500 nm diameter and 80 nm wall thickness (**Figure 5.1**) are synthesized through an ultrasonic spray pyrolysis process using nitrates and sucrose as the gas and carbon source.
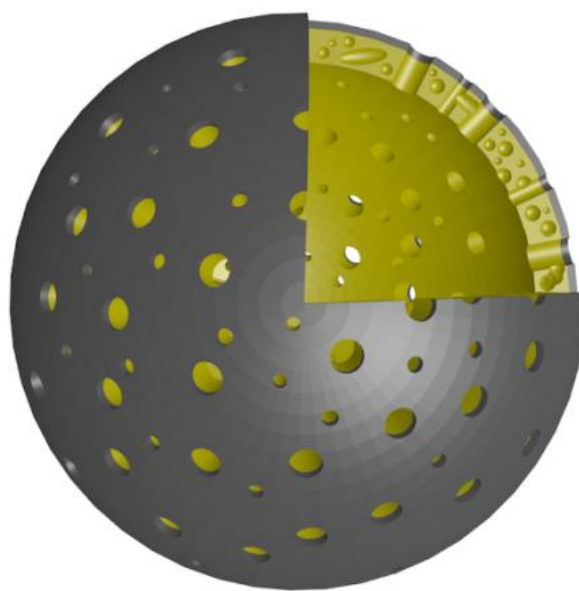
Figure 5.1 Schematic of porous hollow C/Na_2FePO_4F

Nano-sized pores crossing the C/Na_2FePO_4F wall allows electrochemical reaction to take place on the outside and inside surface and also inside of the wall, enhancing the rate capability, while the nano-pores in the wall and micro-cavities in the center provide space to accommodate the volume change, thereby improving the cycling stability. The carbon coated porous hollow C/Na_2FePO_4F spheres can provide 89 mAh g^{-1} at 0.1C, deliver 33% of capacity at a high rate of 9C, and maintain 80% of initial capacity after 750 full charge/discharge cycles at 1C, demonstrating a significant advance in cycling stability of C/Na_2FePO_4F cathode materials from 20 cycles (solid-state reaction)[5.4] to 750 cycles (aerosol spray).

5.2 Experimental

5.2.1 Ultrasonic Spray Pyrolysis Reactor System

The ultrasonic spray pyrolysis (USP) reactor system is shown in **Figure 3.2**. The system is composed of a precursor solution reservoir, an ultrasonic droplet generator (1.7 MHz), two tube furnaces in series, a quartz tube reactor (diameter 22/25 mm x 810 mm) , and a filtration system for particle collection. Spray pyrolysis enables the production of spherical particles with compositional homogeneity with respect to the precursor solution. A frequency generator device is used to form ultrasonic vibrations, thereby creating fine aerosol droplets with stoichiometric composition. The fine aerosol is transported via carrier gas into a tubular furnace at a given temperature. Once in the furnace, processes of diffusion, dehydration, and decomposition occur

simultaneously to form nanoparticles of controlled size, morphology, and composition.

5.2.2 Material Synthesis

The synthesis of C/Na_2FePO_4F was carried out by mixing the stoichiometric amount of sodium fluoride, sodium nitrate, iron nitrate nonahydrate, phosphoric acid, and sucrose (35 wt%) dissolved in water. The species precursor molar concentration was 0.05 M, and the spray pyrolysis temperature was 500 ˚C, while nitrogen carrier gas and quench gas flow rates were held constant at 3 lpm and 10 lpm, respectively. 500 ˚C was chosen as the optimum pyrolysis temperature, which corresponds to a residence time of approximately 3 seconds. Particles were collected on a polytetrafluoroethylene (PTFE) filter using a brush. The as prepared materials were then annealed at 600 ˚C for 8 hours in argon to obtain the desired phase.

5.2.3 Cathode Preparation

Electrochemical performance of C/Na_2FePO_4F was tested in a coin cell using sodium metal as the counter electrode and 1 M $NaClO_4$ in EC/DMC (1:1 by volume) as the electrolyte. C/Na_2FePO_4F cathodes consisted of 80 wt% C/Na_2FePO_4F, 10 wt% acetylene black, and 10 wt% poly(vinylidene fluoride), which were mixed with NMP and pasted on Al foil, and then dried at 80 °C in vacuum. The active material loading is 0.5-0.6 mg cm^{-2}. The charge/discharge behavior was tested using an ArbinBT2000 workstation (Arbin Instruments, TX, USA).

5.2.4 Cathode Characterization

Structural studies were performed by x-ray diffraction (XRD) on D8 Advance with

LynxEye and SolX (Bruker AXS, WI, USA) using CuKα radiation, scanning electron

microscopy on a Hitachi (Tokyo, Japan) SU- 70 HR-SEM with FFT images, and

transmission electron microscopy on a JEOL 2100F field emission TEM (Tokyo,

Japan). Raman spectra of the material were collected using a Raman microscope.

Energy dispersive x-ray spectroscopy (EDS) and thermogravimetric analysis (TGA)

were carried out to determine the amount of carbon. BET measurements were

performed using a Micromeritics physisorption analyzer.

5.3 Results and Discussion

5.3.1 Structural and Morphological Analysis

The crystal structure of C/Na_2FePO_4F hollow particles after annealing in argon at 600

˚C for 8 hours were analyzed by X-ray diffraction. XRD patterns of the annealed

sample (**Figure 5.2**) demonstrates single phase Na_2FePO_4F, which is isostructural to

both Na_2FePO_4OH and Na_2CoPO_4F.
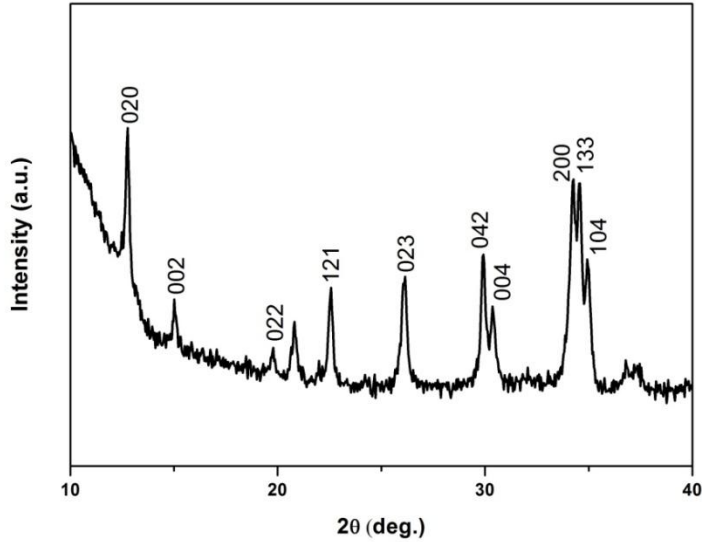
Figure 5.2 XRD full-pattern fitting of C/Na$_2$FePO$_4$F sample

Figure 5.3 shows typical particle morphology after annealing in argon at 600 ˚C for 8 hours. Na$_2$FePO$_4$F particles prepared using USP are spherical in shape with average particle size of 500 nm (ranging from 100 nm to 1 μm, Figure 5.3a). A hollow structure inside of C/Na$_2$FePO$_4$F spherical particles can be clearly observed by a broken hollow sphere and fragments (Figure 5.3b). The thickness of the wall is around 80 nm. The wall is formed by sintering of aggregated nanoparticles (Figure 5.3b and 5.3d) thus leaving many micro-sized cavities (Figure 5.3b) and nanopores inside the wall. The nanopores with size of around 2.5 nm can be more clearly observed in SEM images of the C/Na$_2$FePO$_4$F particle surface (Figure 5.3c). Figure 5.3e clearly shows the presence of a thin layer of carbon coated on the surface of the C/Na$_2$FePO$_4$F particle. The carbon coating thickness is about 10 nm.
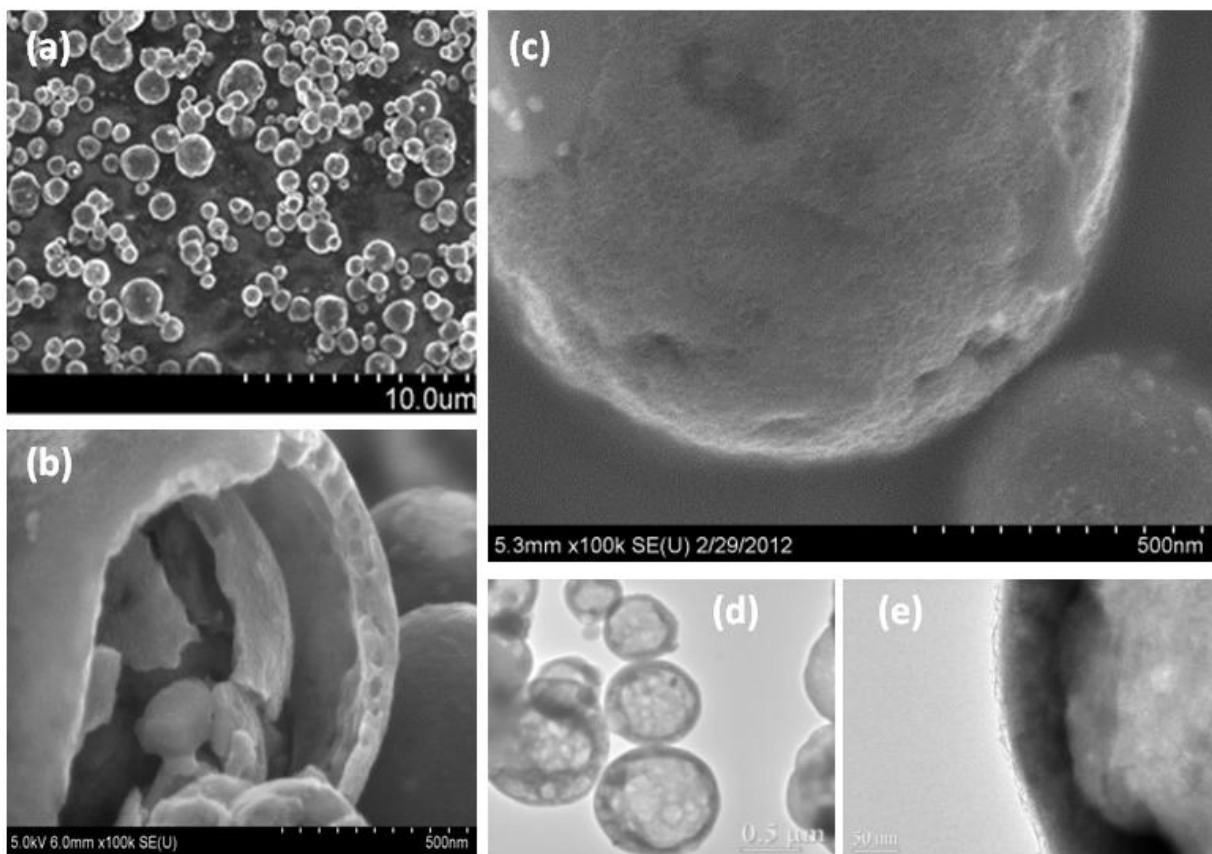
Figure. 5.3 (a) SEM image of C/Na$_2$FePO$_4$F particles prepared by USP with average particle size of 0.5 um (b) Broken shell depicting hollow nature of particles (c) SEM image showing nanoporous structure of particles (d) TEM image showing nanopores and aggregated nature of particle wall (e) TEM image of particle edge depicting a thin carbon layer

According to energy dispersive x-ray spectroscopy (EDS) and thermogravimetric analysis (TGA), the amount of carbon is between 6 to 8 wt%. Raman spectroscopy was used as an additional measurement to confirm the presence of carbon on C/Na$_2$FePO$_4$F hollow particles (**Figure 5.4**). Strong D (defective graphitic structures)

and G-bands (graphitic layers) from elemental carbon on the materials are observed at 1330 cm^{-1} and 1570 cm^{-1}, respectively.
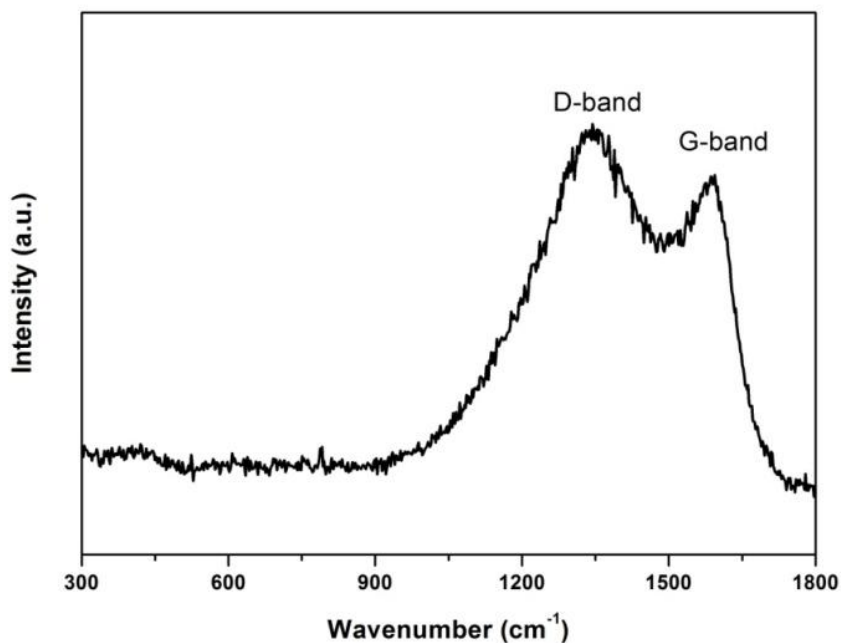
Figure 5.4 Raman spectra of C/Na$_2$FePO$_4$F sample

The pore size distribution and specific surface areas of hollow C/Na$_2$FePO$_4$F particles were characterized using BET (**Figure 5.5**). The BET specific surface area of the particles is 8.7 m^2 g^{-1}. The Barret-Joyner-Halenda (BJH) desorption shows that most of the pores are 2.5 nm and some large pores with average size of 10 nm also exist, which is consistent with SEM observations in Figures 5.3b and 5.3c. The pores in the wall will allow the liquid electrolyte to penetrate through the wall to the inside of the hollow sphere. Therefore, the electrochemical charge transfer reaction can take place on both sides of the wall and in the pores.
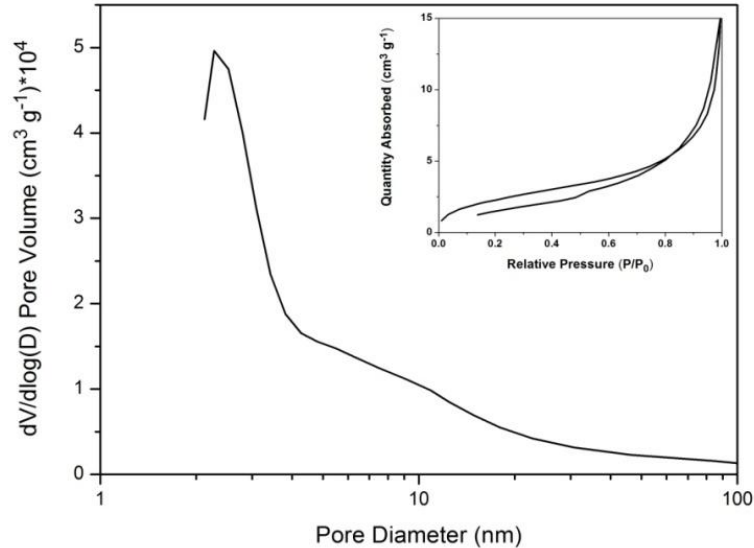
Figure 5.5 Pore size distribution and N_2 adsorption-desorption isotherm (inset) of

C/Na_2FePO_4F sample

The possible formation mechanism of C/Na_2FePO_4F porous hollow particles is shown

in **Figure 5.6**. The initial step in the spray pyrolysis process is the evaporation of a

solution droplet. As precursor droplets move through the furnace (dotted line), water

evaporates and solute concentration is higher at the surface than at the center since

evaporation occurs from the droplet's surface. Therefore, the precursor solution

becomes supersaturated and solute precipitation at the droplet's surface forms a

viscous shell on the surface of the precursor droplet.[5.8] During the formation of

C/Na_2FePO_4F shell, the large amount of gas generated in the center of C/Na_2FePO_4F

shell due to solvent evaporation and CO and CO_2 generation from decomposition of

sucrose in the droplet at high temperatures, results in high internal gas pressure.

When the internal pressure is greater than the mechanical strength of the

C/Na_2FePO_4F shell, the shell breaks resulting in gas escaping from the C/Na_2FePO_4F spheres to form an inner hollow structure and small pores in the wall of hollow C/Na_2FePO_4F spheres.[5.9] The decomposition of sucrose also forms carbon, which is coated on the surface of hollow C/Na_2FePO_4F spheres.
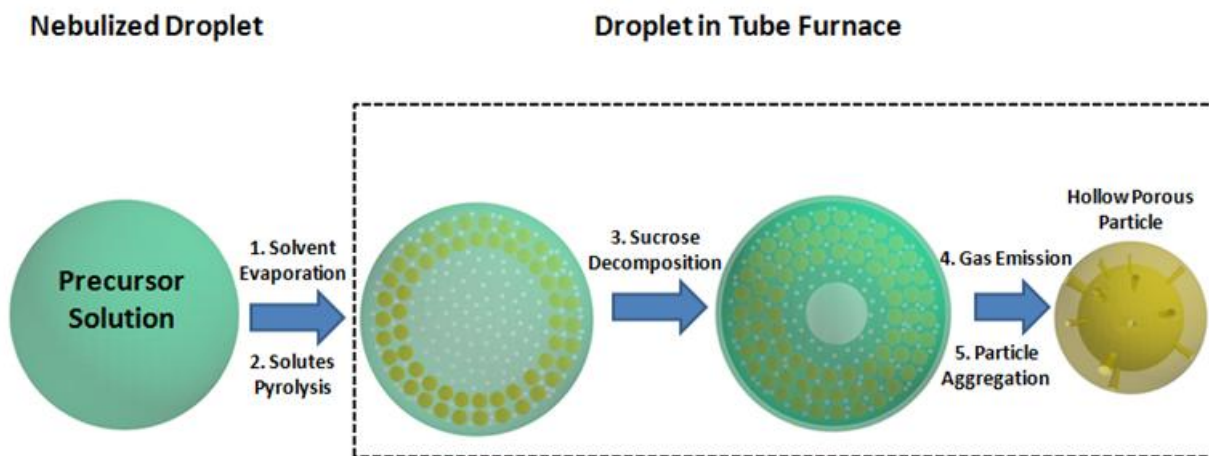
Figure 5.6 Schematic illustration of the formation process of hollow C/Na_2FePO_4F spheres fabricated by USP. The dotted line represents inside the furnace. Yellow spheres are the particles while white spheres are the gaseous species.

5.3.2 Electrochemical Characterization

Galvanostatic charge/discharge performance of carbon coated C/Na_2FePO_4F cathode materials was tested in a voltage range of 2.0-3.8 V in a Na-ion coin cell. **Figure 5.7** shows the typical voltage profiles of C/Na_2FePO_4F cathode during the 5th cycle at a rate of 0.1C. Two well-defined reversible voltage plateaus are evident at 2.9 V and 3.1 V, which represent two reversible phase transformations of $Na_2FePO_4F \leftrightarrow Na_{1.5}FePO_4F$ and $Na_{1.5}FePO_4F \leftrightarrow NaFePO_4F$. An intermediate phase $Na_{1.5}FePO_4F$

has lattice parameters between the two end members, and its structure undergoes a slight change in symmetry to a monoclinic unit cell.[5.2]
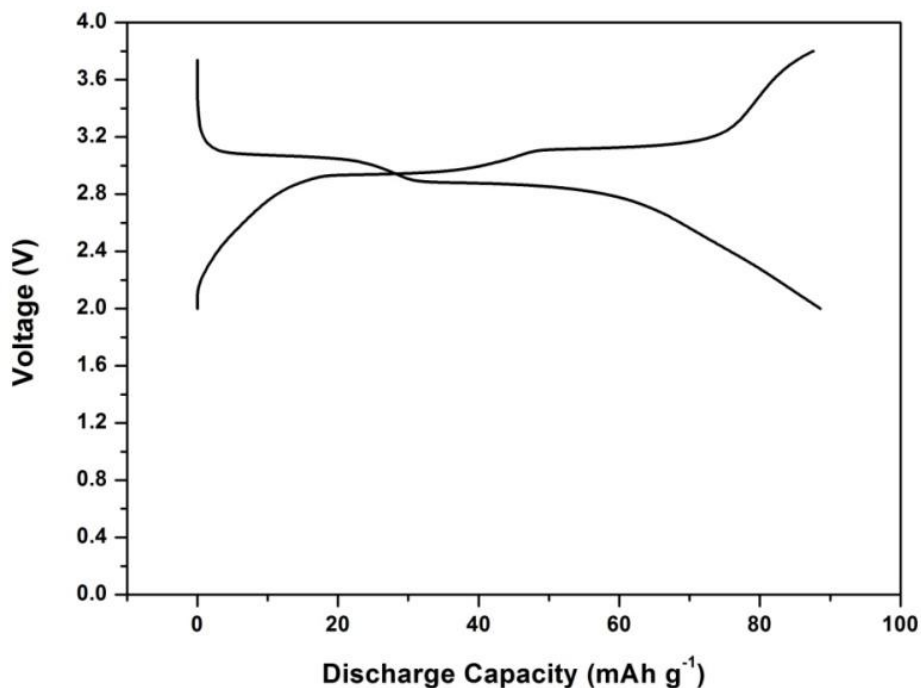
Figure 5.7 Galvanostatic charge/discharge curves of a Na/Na$_2$FePO$_4$F cell cycled at a rate of 0.1C

Due to the unique carbon coated porous hollow structure, C/Na$_2$FePO$_4$F shows exceptional cycling stability as demonstrated in **Figure 5.8**. C/Na$_2$FePO$_4$F can deliver approximately 90 mAh g^{-1} of reversible capacity and retain 90% of capacity after 100 cycles.
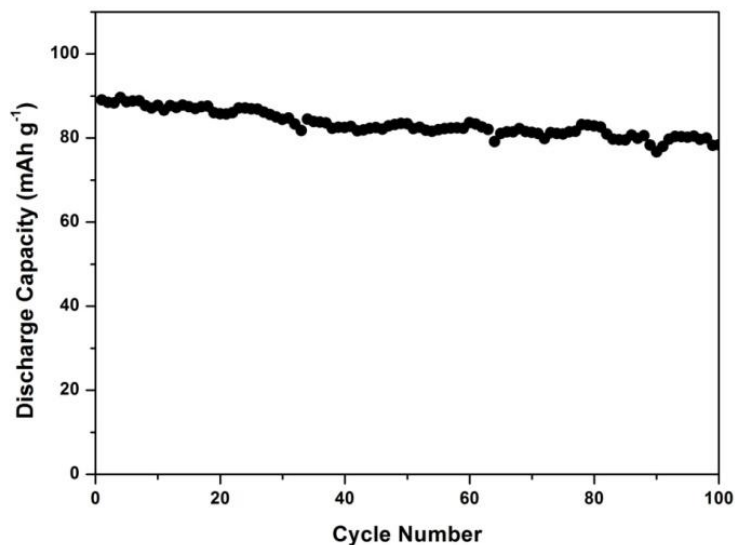
Figure 5.8 Capacity retention of C/Na$_2$FePO$_4$F cycled at a rate of 0.1C

Because of the excellent stability of the material at a low C-rate (0.1C), much longer

charge/discharge cycles were tested for C/Na$_2$FePO$_4$F cathodes at a high rate of 1C

and also shown in **Figure 5.9**. The initial capacity of C/Na$_2$FePO$_4$F is 75 mAh g^{-1} at

1C. After 750 cycles, the capacity decreases to 60 mAh g^{-1} which corresponds to

capacity retention of 80%, while the C/Na$_2$FePO$_4$F synthesized using solid-state

reaction can retain 75% of capacity after only 20 cycles. This work represents a

significant advance in C/Na$_2$FePO$_4$F cathode materials for Na-ion batteries.
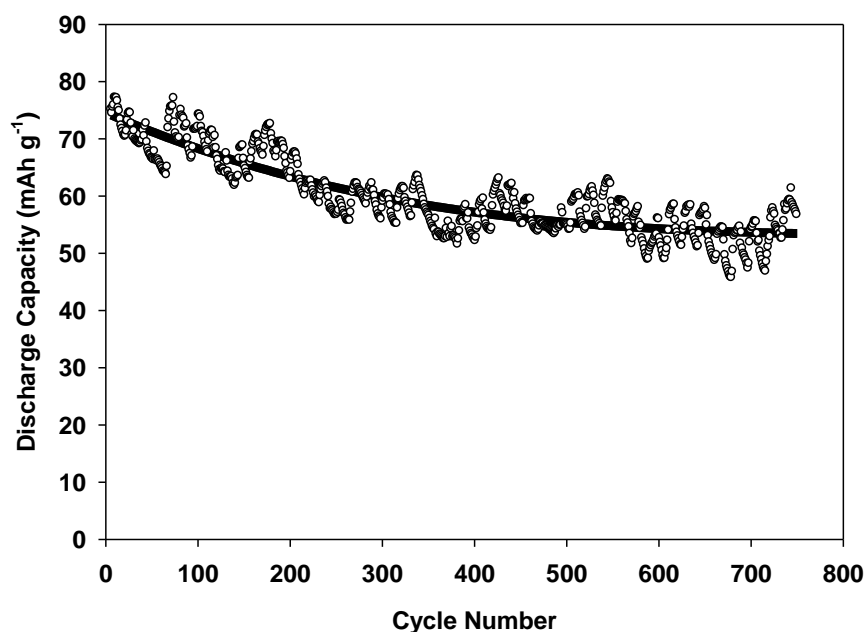
Figure 5.9 Capacity retention of C/Na$_2$FePO$_4$F cycled at a rate of 1C

The C/Na$_2$FePO$_4$F cathodes after experiencing 100 charge/discharge cycles at 0.1C (the sample in Figure 5.8) were subjected to a rather abusive high rate testing protocol in which the cells were both charged and discharged at the same high rates. As shown in **Figure 5.10**, under this stringent condition, C/Na$_2$FePO$_4$F can deliver approximately 80 mAh g^{-1} of reversible capacity at 0.1C and 26 mAh g^{-1} at 9C. Even after 100 charge/discharge cycles, C/Na$_2$FePO$_4$F can still provide 33% of the capacity at 9C. The C/Na$_2$FePO$_4$F synthesized using solid state reaction can only provide 15 mAh/g at the rate of 8C.[5.4]

66
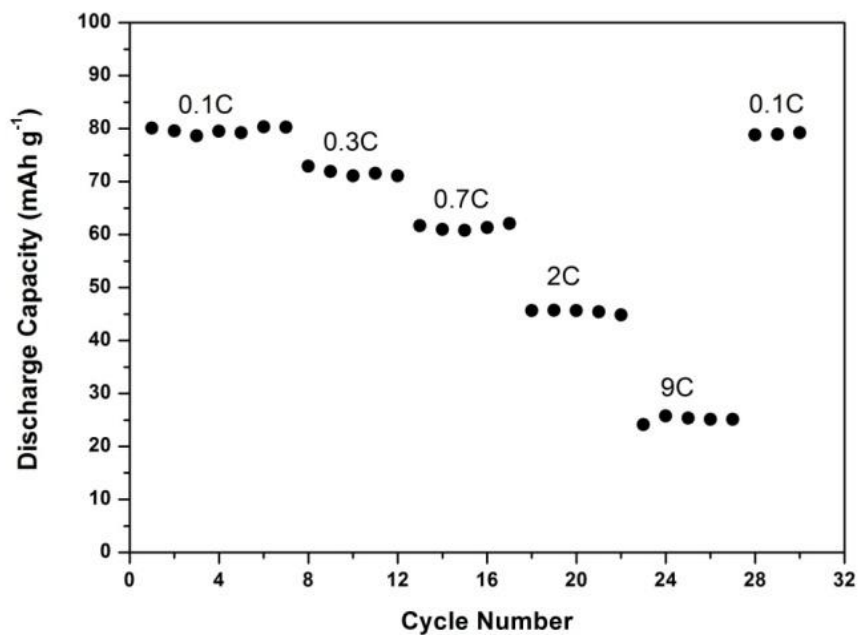
Figure 5.10 Rate capability of C/Na$_2$FePO$_4$F. Before rate capacity test, the C/Na$_2$FePO$_4$F cathode was charged and discharged at 0.1C for 100 cycles

The discharge curves at the various C-rates are given in **Figure 5.11**. Such a high rate capability and long cycling stability of C/Na$_2$FePO$_4$F cathodes in Na-ion cells have not been reported before, demonstrating a great potential for commercialization of Na-ion batteries.
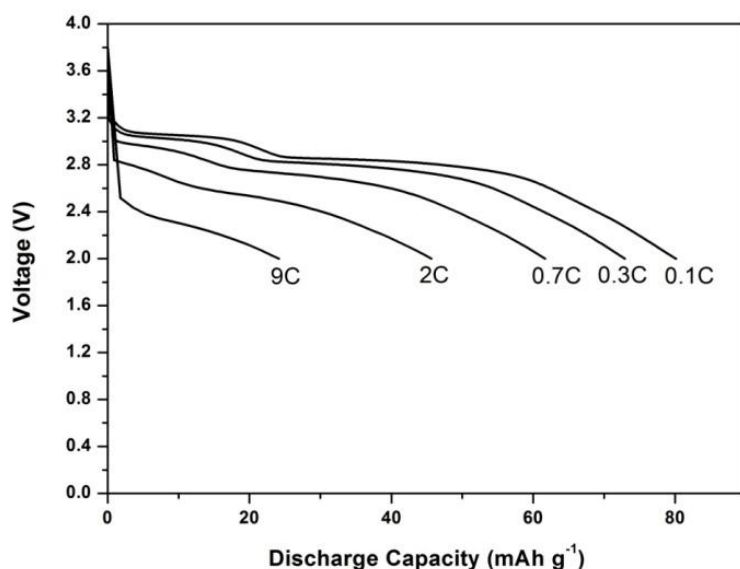
Figure 5.11 Discharge curves of C/Na$_2$FePO$_4$F at various C-rates after 100 cycles at

0.1C

Although the Na$^+$ ion is much larger than Li$^+$ the carbon coated hollow

C/Na$_2$FePO$_4$Fcathode materials synthesized using an USP process demonstrated a

high rate capability and long cycling stability in Na-ion batteries, which is

comparable to the lithium-ion batteries. The high rate performance of C/Na$_2$FePO$_4$F

is attributed to (1) high interface area between liquid electrolyte and C/Na$_2$FePO$_4$F

due to penetration of the liquid electrolyte into pores and center hole of hollow

C/Na$_2$FePO$_4$F, (2) carbon coating increasing the charge transfer reaction kinetics, and

(3) hollow structure shortening the diffusion length of Na$^+$ ion. Hollow C/Na$_2$FePO$_4$F

is also structurally very robust to withstand the volume change (3.7%) during Na$^+$

insertion/extraction, resulting in a long cycling life.

5.4 Conclusion

In summary, carbon coated hollow C/Na$_2$FePO$_4$F particles with pores in the shell were synthesized using an USP process. The C/Na$_2$FePO$_4$F cathodes can deliver 89 mAhg^{-1} capacity at a low rate of 0.1C, and 75 mAh g^{-1} at 1C, and maintains 33% of capacity at 9C. After 750 cycles at 1C, C/Na$_2$FePO$_4$F cathodes can still provide 60 mAh g^{-1}, which is 80% of initial capacity. This enhanced electrochemical performance is attributed to the unique hollow spherical and porous structure of the material inherent to the spray pyrolysis process. Additionally the presence of a thin carbon layer acts to enhance the rate capability and cycling stability.

References

[5.1] Dunn B., Kamath H., Tarascon J.M.. *Science* 334, (**2011)** 928.

[5.2] Palomares V., Serras P., Villaluenga I., Hueso K.B., Carretero-Gonzalez J., Rojo T. *Energy and Environmental Science* 5 (**2012**) 5884.

[5.3] Vidal-Abarca C., Lavela P., Tirado J.L., Chadwick A.V., Alfredsson M., Kelder E. *J. Power Sources* 197 (**2012**) 314.

 [5.4] Kawabe Y., Yabuuchi N., Kajiyama M., Fukuhara N., Inamasu T., Okuyama R., Nakai I., Komaba S. *Electrochem.Commun.*13.11 (**2011**) 1225.

 [5.5] Yao, Y., McDowell M. T., Ryu I., Wu H., Liu N., Hu L., Nix W. D., Cui Y. *Nano Letters*, 11 (**2011**) 2949.

[5.6] Wu H., Chan G., Choi J. W., Ryu I., Yao Y., McDowell M. T., Lee S.W., Jackson A., Yang Y., Hu L., Cui Y. *Nature Nanotechnology*, 7 (**2012**) 310.

[5.7] Dong, F., Huang Y., Zou S., Liu J., Lee S. C. *J. Physical Chem. C* 115 (**2011**) 241.

[5.8] Ortega, J., Kodas T.T.. *J. Aerosol Science* 23 (**1992**) 253.

[5.9] Patil, L.A., Shinde M.D., Bari A.R., Deo V.V. *Sensors and Actuators B: Chem.* 143 (**2009**) 316.

Chapter 6: P2-Type Transition Metal Oxides for NIB Cathodes

6.1 Introduction

Lithium-ion batteries are of great interest because of their role in consumer electronics and vehicles. As the demand for lithium rises, more abundant alternatives such as sodium will play an ever more important role.[6.1] Smart electric grids that integrate discontinuous renewable energy sources are one such application for sodium-ion batteries, where weight and footprint is less important.[6.2] Finding a suitable host material to accommodate Na-ions and allow reversible and rapid ion insertion and extraction has been a challenge due to a 55% larger radius than Li-ions. Sodium has a molar mass of ~23 g mol^{-1} which is roughly three times as heavy as lithium (~7 g mol^{-1}) and the electromotive force voltage of sodium versus lithium is approximately 300 mV less. These factors result in a lower energy density for sodium compared to lithium cells. Another limitation of sodium insertion materials stems from the large cation radius of Na$^+$ (1.02 Å) versus Li$^+$ (0.76 Å), which results in sodium insertion materials favoring octahedral or prismatic coordination. The abundance of sodium (4th most abundant element in the Earth's crust) could provide a low-cost energy storage alternative to the mature lithium-ion technology.

Researchers have studied sodium ion batteries in terms of the active materials that can be used for anodes and cathodes. The use of porous carbon,[6.3-6.5] low potential metal phosphates,[6.6] low potential metal oxides,[6.7] and alloys have all been investigated for use as negative electrodes in sodium-ion batteries.[6.8] Materials such as

fluorophosphates [6.9-6.15] and layered oxides [6.16-6.20] have been investigated as the

positive electrode. Among the number of layered oxide materials of potential interest

identified, Na_xMnO_2 ($0<x\leq1$) phases, initially reported by Parant et al.[6.21] are

promising due to the low cost of precursors and ease of synthesis. In these

compounds, alkali metals are coordinated to six oxygen atoms in either a trigonal

prismatic (P) or octahedral geometry (O). Additional numbers are included in the

nomenclature of these layered compounds to discern the alkali metal layers. For

example, P2 denotes the environment is prismatic and the unit cell is comprised of

two MnO_2 sheets. The P2 phase has shown the most promise in regards to battery

performance among the various Na_xMnO_2 phases studied.[6.22] Various synthetic

pathways have been investigated to produce the structural P2 type, (i) high-

temperature methods under oxygen pressure;[6.21] (ii) thermal decomposition of

$NaMnO_4$;[6.23] (iii) hydrothermal synthesis;[6.24] and (iv) a sol–gel approach.[6.25] These

solution procedures involve multistep chemical reactions and tend to lead to hydrated

phases. Raising the temperature to remove the water and increase the crystallinity is

often unsuccessful as it causes a structural rearrangement that yields tunnel-like

structures or even degradation.[6.25]

In the literature, much attention has been paid to the layered transition metal oxides as

cathode materials for affordable sodium ion batteries. Specifically, combinations of

Mn, Fe, and/or Ni-based oxide cathode materials have been reported. [6.26-6.31]

Yabuuchi et al. [6.26] were the first to report the electrochemical sodium insertion

reaction of P2 and O3-type $Na_x[Fe_{0.5}Mn_{0.5}]O_2$. Mortemard de Boisse et al. [6.27] also

studied the electrochemical performance of P2 and O3-$Na_x[Fe_yMn_{1-y}]O_2$ with varying

stoichiometries of Na, Fe, and Mn. It was shown that the oxide with a higher Mn content can deliver more capacity and provide better structural stability. [6.27] Both studies showed that P2-type oxides have higher reversible capacity than those of O3-type; however, the cycling stability needed improvement. Yuan et al. [6.29] added nickel to the P2-$Na_{0.67}Mn_{0.65}Fe_{0.35}O_2$ structure to achieve a reversible capacity of 208 mAh g^{-1}, improved cycling performance (capacity retention of 71% after 50 cycles) and high rate capability (119 mAh g^{-1}at 8 C). However, the capacity fading in the voltage window of 1.5-4.3 V is still evident. It is widely known that the Jahn-Teller distortion of Mn^{3+} is a crucial factor on the structural stability for Mn based oxides during ion insertion. The Jahn-Teller effect occurs if the lowest energy level of a molecule is degenerate, in which case it will distort spontaneously so as to remove the degeneracy and make one energy level more stable. To alleviate this effect, foreign metallic ions are introduced to decrease the Mn^{3+} content and stabilize the crystal structure. [6.32] An added benefit of introducing dopants is to provide more reversible redox capacity. The structural, morphological, and electrochemical properties of the $NaMO_2$ type oxides were investigated to demonstrate the effect of Ni and Fe substitution on the reversible capacity and cycling stability of the electrode.

In this chapter, we report the improved electrochemical properties of P2-type sodium layered oxides ($Na_{0.67}MnO_2$ and $Na_{0.67}Fe_{0.20}Ni_{0.15}Mn_{0.65}O_2$) synthesized by ultrasonic spray pyrolysis (USP) for application as the positive electrode in sodium-ion batteries.

6.2 Experimental

6.2.1 Ultrasonic Spray Pyrolysis Reactor System

The ultrasonic spray pyrolysis (USP) reactor system is composed of a precursor solution reservoir, an ultrasonic droplet generator (1.7 MHz), two tube furnaces in series, a quartz tube reactor (diameter 22/25 mm x 810 mm) , and a filtration system for particle collection. Spray pyrolysis enables the production of spherical particles with compositional homogeneity with respect to the precursor solution. A frequency generator device is used to form ultrasonic vibrations, thereby creating fine aerosol droplets with stoichiometric composition. The fine aerosol is transported via carrier gas into a tubular furnace at a given temperature. Once in the furnace, processes of diffusion, dehydration, and decomposition occur simultaneously to form nanoparticles of controlled size, morphology, and composition.

6.2.2 Material Synthesis

The synthesis of each material was carried out by mixing the stoichiometric amount of sodium nitrate and corresponding metal nitrates dissolved in water. In each case, the total species precursor molar concentration was 0.08 M, and the spray pyrolysis temperature was 600 ˚C, while nitrogen carrier gas and quench gas flow rates were held constant at 3 lpm and 10 lpm, respectively. 600 ˚C was chosen as the optimum pyrolysis temperature, which corresponds to a residence time of approximately 3 seconds. Particles were collected on a polytetrafluoroethylene (PTFE) filter using a brush. The as prepared materials were then annealed at 800 °C for 6 hours in air to obtain the desired phase.

6.2.3 Cathode Preparation

Electrochemical performance was tested in a coin cell using sodium metal as the counter electrode and 1 M $NaClO_4$ in a mixture of fluoroethylene carbonate-dimethyl carbonate (FEC/DMC, 1:1 by volume) as the electrolyte and Celgard®3501 (Celgard LLC Corp., USA) as the separator. Cathodes consisted of 70 wt% active material, 20 wt% acetylene black, and 10 wt% sodium alginate, which were mixed with water and pasted on Al foil, and then dried at 100 °C in vacuum. The active material loading is 0.5-0.6 mg cm^{-2}. The charge/discharge behavior was tested using an ArbinBT2000 workstation (Arbin Instruments, TX, USA). Rate capability was examined by charging and discharging at different rates (1C= 260 mA g^{-1}). The cyclic voltammogram scanned at 0.1 mV s^{-1} between 2.0-3.8 V was recorded using a Solatron 1260/1287 Electrochemical Interface (Solatron Metrology, UK).

6.2.4 Cathode Characterization

Structural studies were performed by x-ray diffraction (XRD) on D8 Advance with LynxEye and SolX (Bruker AXS, WI, USA) using CuKα radiation, scanning electron microscopy on a Hitachi (Tokyo, Japan) SU- 70 HR-SEM with FFT images, and transmission electron microscopy on a JEOL 2100F field emission TEM (Tokyo, Japan).

Results and Discussion

6.3.1 Structural and Morphological Analysis

XRD patterns of the as prepared and annealed samples demonstrate that single phase $Na_{0.67}MnO_2$ (**Figure 6.1**) and $Na_{0.67}Mn_{0.65}Fe_{0.20}Ni_{0.15}O_2$ (**Figure 6.2**) is obtained after heat treatment.
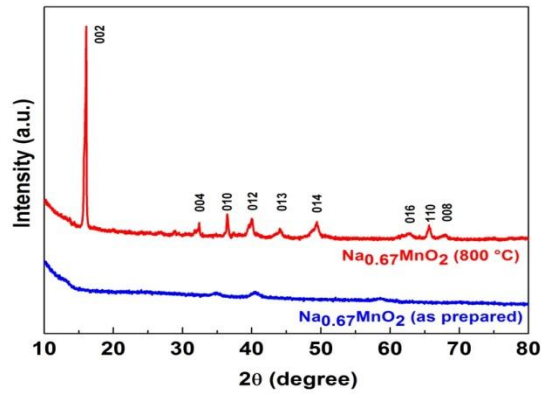
Figure 6.1 XRD full-pattern fitting of $Na_{0.67}MnO_2$ sample before and after heat treatment
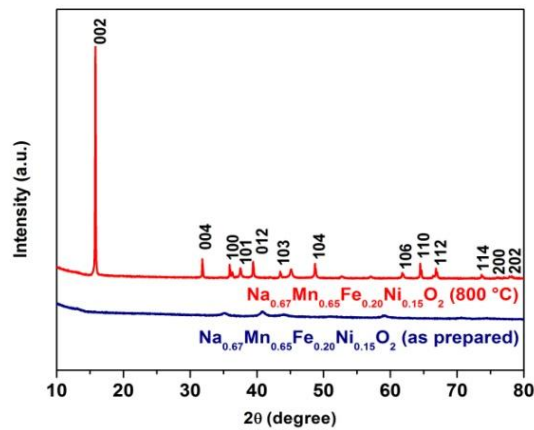
Figure 6.2 XRD full-pattern fitting of $Na_{0.67}Mn_{0.65}Fe_{0.20}Ni_{0.15}O_2$ sample before and after heat treatment

Figure 6.3 shows typical particle morphology before and after annealing in air at 800

˚C for 6 hours. Particles prepared using USP are spherical in shape with average

particle size of 700 nm (ranging from 400 nm to 1 μm). After heat treatment, the

particles adopt a regular lamella-like morphology.
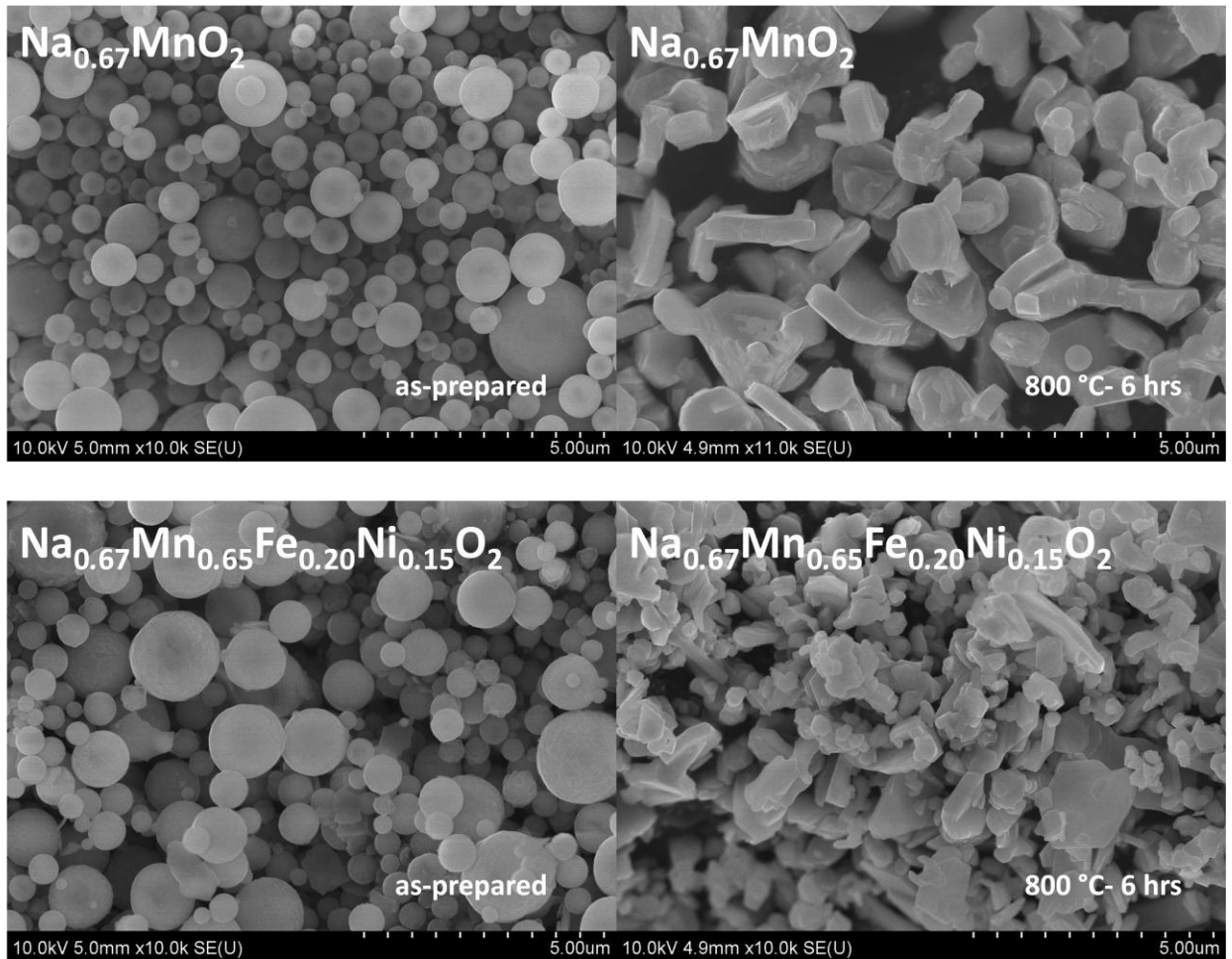
Figure 6.3 SEM images of particles prepared by USP before and after heat treatment

Transmission electron microscopy (TEM) after annealing shows that the $Na_{0.67}MnO_2$ and $Na_{0.67}Mn_{0.65}Fe_{0.20}Ni_{0.15}O_2$ particles are dense, while energy dispersive x-ray spectroscopy (EDS) mapping demonstrates that the composition remains uniform throughout the particle (**Figure 6.4 and Figure 6.5**).
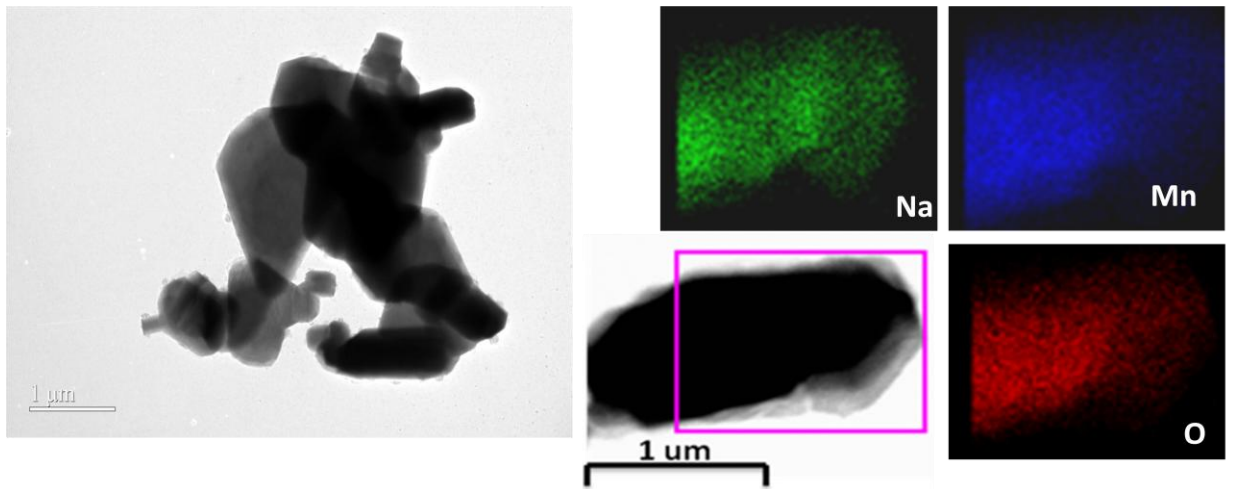
Figure 6.4 TEM image and EDS mapping of $Na_{0.67}MnO_2$ particles after heat treatment
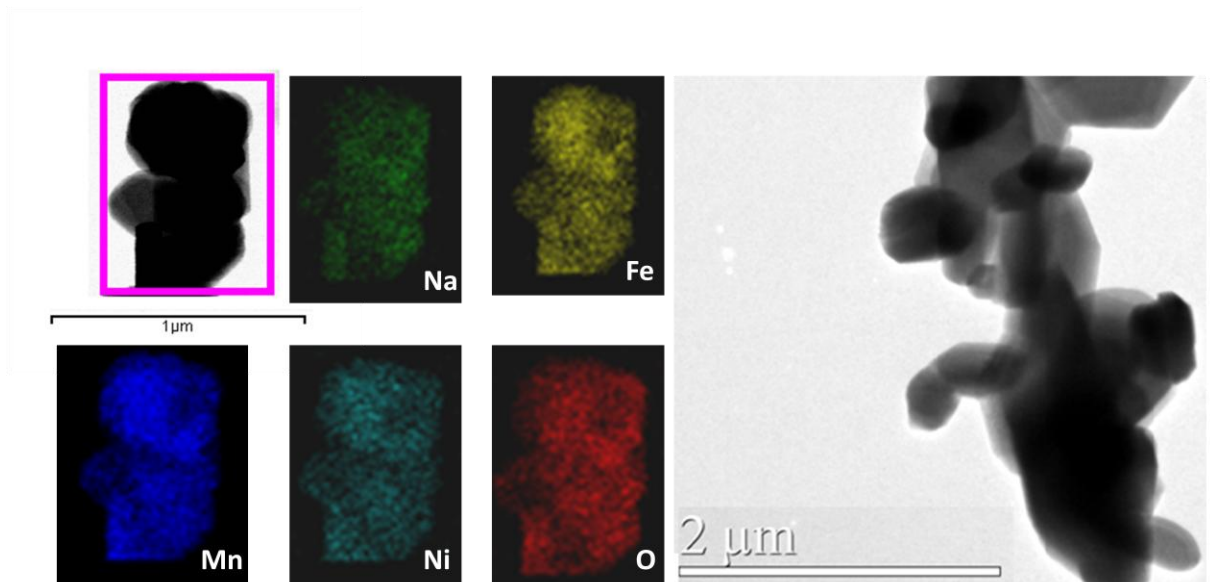
Figure 6.5 TEM image and EDS mapping of $Na_{0.67}Mn_{0.65}Fe_{0.20}Ni_{0.15}O_2$ particles after heat treatment

6.3.2 Electrochemical Characterization

Electrochemical properties of two P2-type layered samples for the sodium-ion insertion reaction were characterized by cyclic voltammogram (CV) as shown in **Figure 6.6**. The partial substitution of Ni and Fe for Mn decreases the number of peaks seen by CV. Galvanostatic charge/discharge performance of cathode materials was tested in a voltage window of 2.0-3.8 V and an expanded window of 1.5-4.3 V in an effort to increase the capacity. **Figure 6.7** shows typical voltage profiles of $Na_{0.67}MnO_2$ during the 5th cycle at a rate of 0.1 C for the narrow voltage window and expanded window. The voltage versus capacity shows pronounced features with strong voltage steps and plateaus indicative of phase transitions upon desodiation. Phase changes in Na_xMnO_2 can be due to Na-vacancy ordering or transitions that involve the gliding of oxygen planes, which is attributed to the thermodynamic instability of prismatic sites without sodium ions. Na prefers both octahedral and trigonal prismatic environments and the trigonal prismatic coordination can only be achieved in an O3 stacking by sliding some of the oxygen layers (see **Figure A.2**).[6.33]
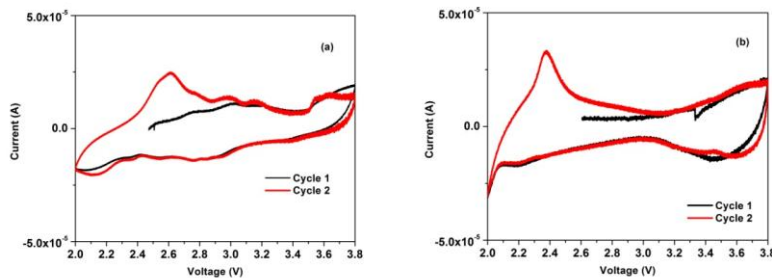
Figure 6.6 Cyclic voltammograms of (a) $Na_{0.67}MnO_2$ and (b) $Na_{0.67}Mn_{0.65}Fe_{0.20}Ni_{0.15}O_2$ in the initial two cycles scanned between 2.0–3.8 V at a rate of 0.1mV/s
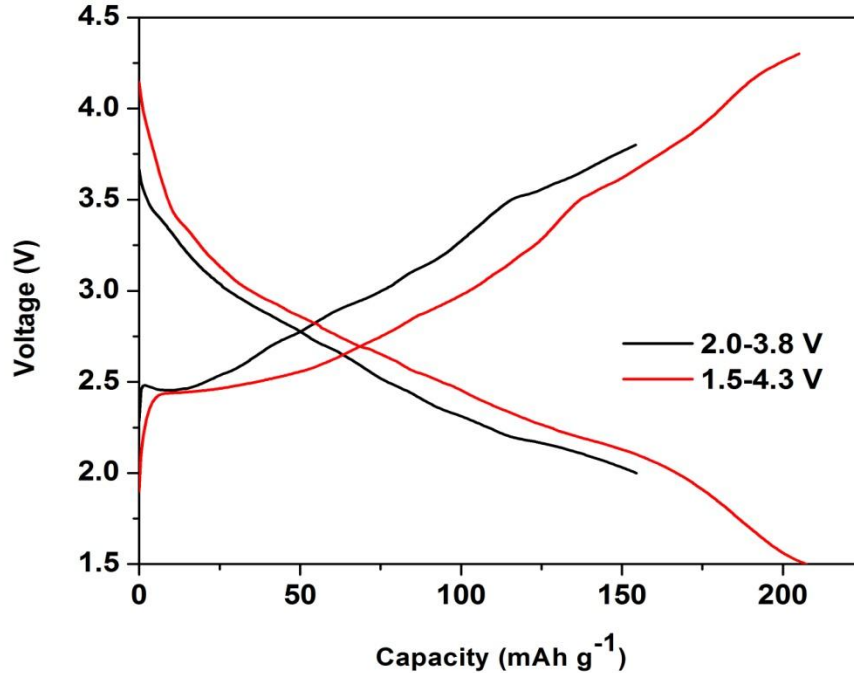
Figure 6.7 Galvanostatic charge/discharge curves of $Na_{0.67}MnO_2$ cell cycled at a rate

of 0.1 C

Figure 6.8 shows typical voltage profiles of $Na_{0.67}Mn_{0.65}Fe_{0.20}Ni_{0.15}O_2$ during the 1st

and 5th cycles at a rate of 0.1 C for the narrow voltage window and expanded

window. The material when cycled in the expanded window exhibited three

charge/discharge plateaus at ~4.20, 3.50 and 2.30 V, corresponding to the redox

reactions of Ni^{2+}/Ni^{4+}, Fe^{3+}/Fe^{4+}, and Mn^{3+}/Mn^{4+} components, respectively. This also

indicates three steps of phase transformations occurring during the Na-

insertion/extraction reactions. Multiple metals in the transition-metal layer can

stabilize the P2-phase structure so as to alleviate slight transitions of the different

phases.
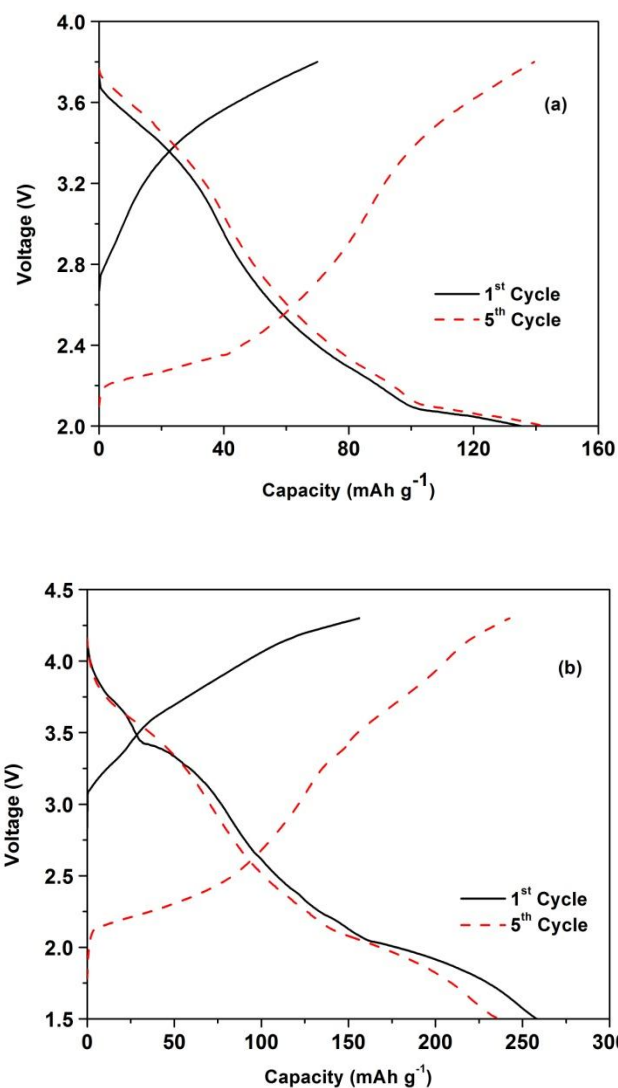
Figure 6.8 Galvanostatic charge/discharge curves of $Na_{0.67}Mn_{0.65}Fe_{0.20}Ni_{0.15}O_2$ cell

cycled at a rate of 0.1 C in the (a) narrow and (b) expanded voltage window

$Na_{0.67}MnO_2$ demonstrates exceptional cycling stability as seen in **Figure 6.9**.

$Na_{0.67}MnO_2$, when cycled in the expanded window can deliver approximately 205

mAh g^{-1} and retain 86% of capacity after 30 cycles. A stable capacity of 176 mAh g^{-1}

is achieved in the narrow window after 30 cycles. The increase in capacity from the first cycle is due to the insufficient wetting of electrolyte intially.
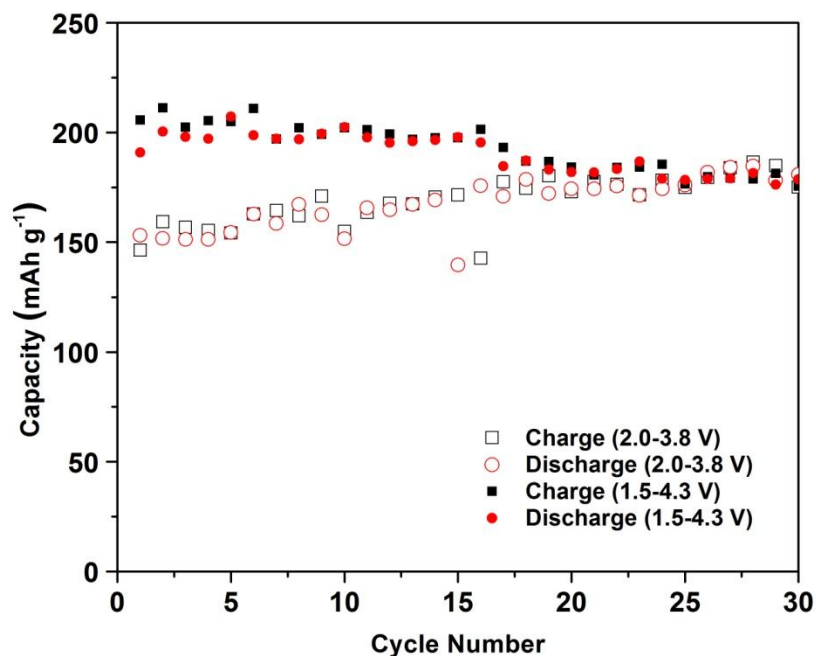
Figure 6.9 Capacity retention of $Na_{0.67}MnO_2$ cycled at a rate of 0.1 C

$Na_{0.67}Mn_{0.65}Fe_{0.20}Ni_{0.15}O_2$ also demonstrates exceptional cycling stability as seen in **Figure 6.10**. $Na_{0.67}Mn_{0.65}Fe_{0.20}Ni_{0.15}O_2$, when cycled in the expanded window can deliver approximately 258 mAh g^{-1} and retain 65% of capacity after 25 cycles. A stable capacity of 150 mAh g^{-1} is achieved in the narrow window after 100 cycles.
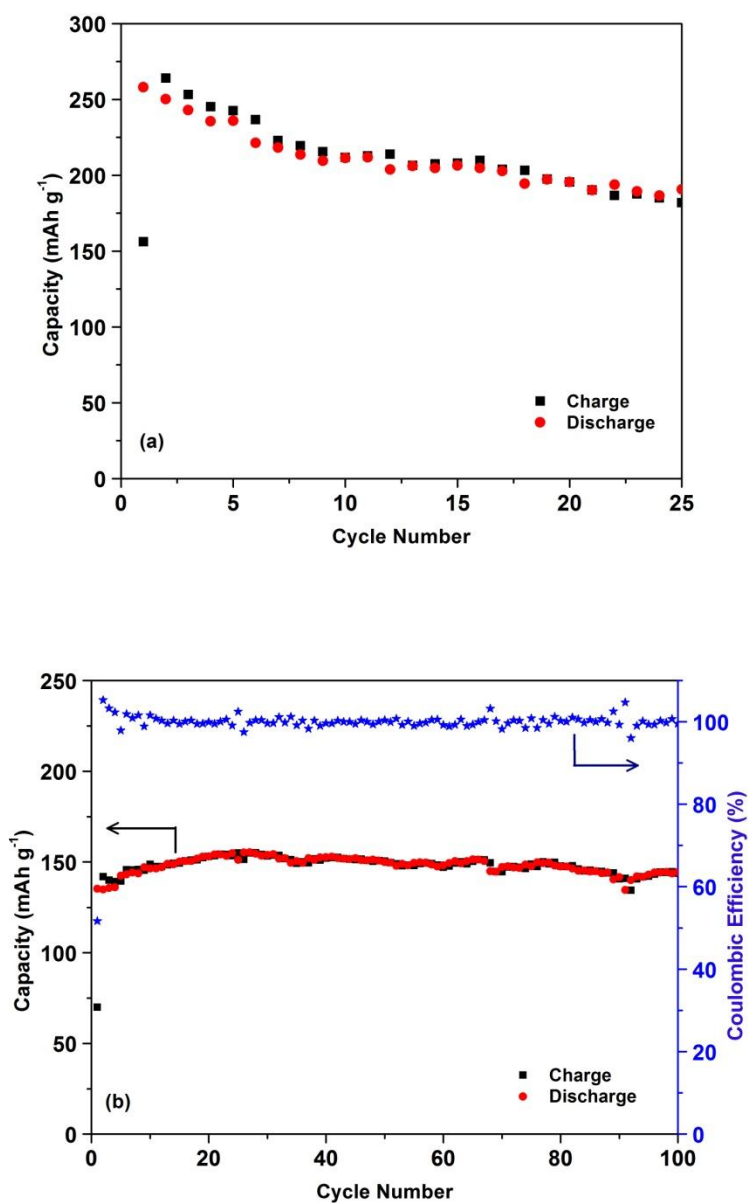
Figure 6.10 Capacity retention of $Na_{0.67}Mn_{0.65}Fe_{0.20}Ni_{0.15}O_2$ cycled at a rate of 0.1 C

in the (a) expanded and (b) narrow voltage window

The $Na_{0.67}MnO_2$ cathodes were subjected to rate testing protocol in which the cells

were both charged and discharged at the same high rates in the narrow voltage

window. As shown in **Figure 6.11**, under this stringent condition, $Na_{0.67}MnO_2$ can deliver approximately 116 mAh g^{-1} at 2C, which is 73% of initial capacity. The discharge curves at the various C-rates are given in **Figure 6.12**.
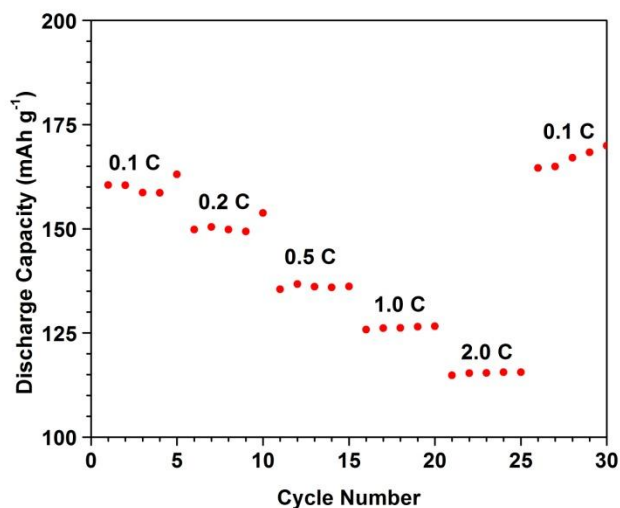
Figure 6.11 Rate capability of $Na_{0.67}MnO_2$
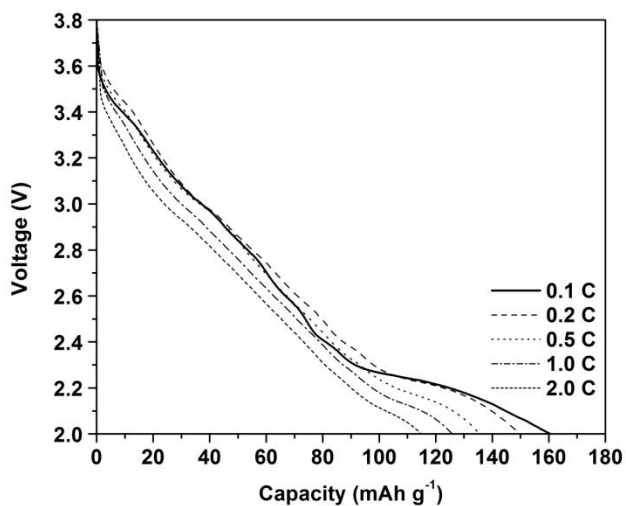
Figure 6.12 Discharge curves of $Na_{0.67}MnO_2$ at various C-rates

The $Na_{0.67}Mn_{0.65}Fe_{0.20}Ni_{0.15}O_2$ cathodes were subjected to rate testing protocol in which the cells were both charged and discharged at the same high rates in the narrow voltage window. As shown in **Figure 6.13**, under this stringent condition, $Na_{0.67}Mn_{0.65}Fe_{0.20}Ni_{0.15}O_2$ can deliver approximately 91 mAh g^{-1} at 2C, which is 61% of initial capacity. The discharge curves at the various C-rates are given in **Figure 6.14**.
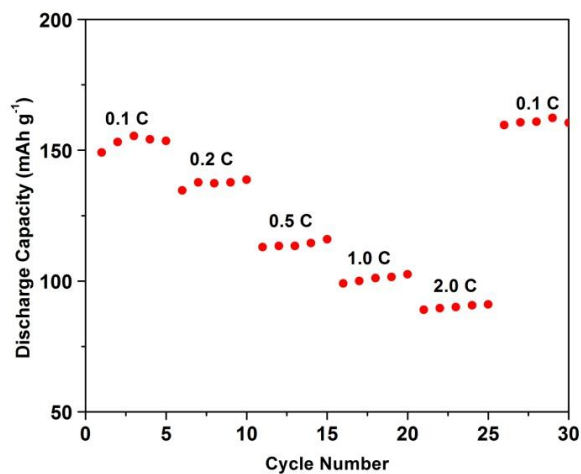
Figure 6.13 Rate capability of $Na_{0.67}Mn_{0.65}Fe_{0.20}Ni_{0.15}O_2$
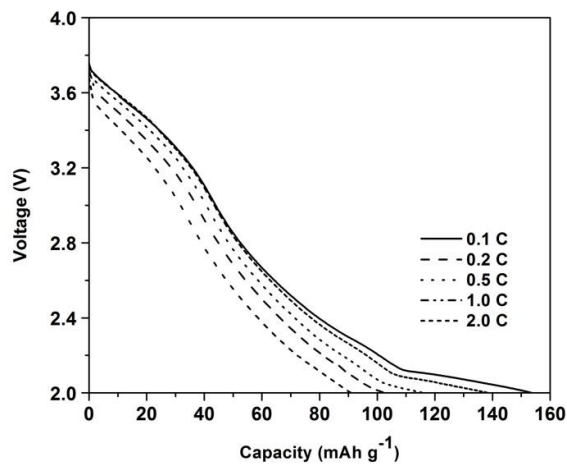
Figure 6.14 Discharge curves of $Na_{0.67}Mn_{0.65}Fe_{0.20}Ni_{0.15}O_2$ at various C-rates

Because of the excellent stability of the material at a low C-rate (0.1C), much longer charge/discharge cycles were tested for $Na_{0.67}MnO_2$ cathodes. After the rate test, the cell was subjected to a high rate of 1C as shown in **Figure 6.15**. The initial capacity of $Na_{0.67}MnO_2$ is 138 mAh g^{-1} at 1C. After 225 cycles, the capacity decreases to 134 mAh g^{-1} which corresponds to capacity retention of 97%.
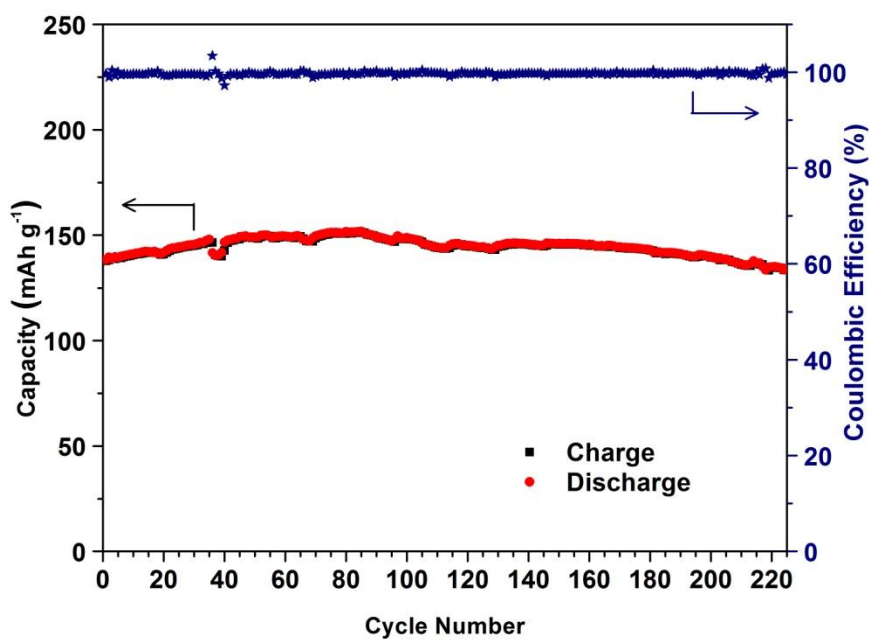
Figure 6.15 Capacity retention of $Na_{0.67}MnO_2$ cycled at a rate of 1.0 C after rate test

A similar procedure was followed for $Na_{0.67}Mn_{0.65}Fe_{0.20}Ni_{0.15}O_2$. After the rate test, the cells were subjected to a high rate of 1C as shown in **Figure 6.16**. The initial capacity of $Na_{0.67}Mn_{0.65}Fe_{0.20}Ni_{0.15}O_2$ is 106 mAh g^{-1} at 1C. After 350 cycles 100% of capacity is retained.
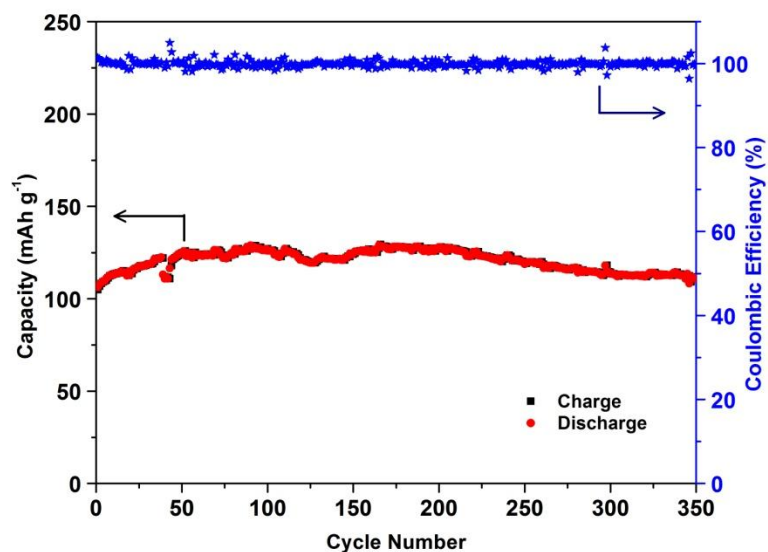
Figure 6.16 Capacity retention of $Na_{0.67}Mn_{0.65}Fe_{0.20}Ni_{0.15}O_2$ cycled at a rate of 1.0 C

after rate test

Although the reversible capacity of $Na_{0.67}Mn_{0.65}Fe_{0.20}Ni_{0.15}O_2$ is lower than

$Na_{0.67}MnO_2$ the stability and capacity retention is improved with the addition of

multiple transition metals. The introduction of Ni^{2+} and Fe^{2+} with low valence raises

the average valence of Mn to alleviate the Jahn-Teller distortion.

Such a high rate capability and long cycling stability of P2-type transition metal oxide

cathodes in Na-ion cells have not been reported before, demonstrating a great

potential for commercialization of Na-ion batteries. XRD patterns of $Na_{0.67}MnO_2$ after

the initial charge and after 45 cycles (**Figure 6.17**) demonstrates the robustness of the

crystal structure. The possible phase transition is from P2 to OP4 in which the

octahedral and prismatic layers are piled up alternately along the c-axis direction.

During the charge process, the sodium ions are selectively extracted from one of the two layers, resulting in the P2-OP4 phase transition. The formation of the intermediate OP4 phase reduces the damage by gliding of layers, at least when compared with the P2-O2 direct phase transition. Although the OP4 phase transition process still, in part, requires the gliding of layers, the P2-OP4 phase transition is highly reversible. [6.26] The peaks at 45°, 65°, and 78° correspond to the aluminum from the current collector. **Figure 6.18** shows SEM images of $Na_{0.67}MnO_2$ after 45 cycles. Particle morphology remains the same from before cycling, indicating the ability of the material to accommodate the continuous strains and distortions associated with sodiation and desodiation.
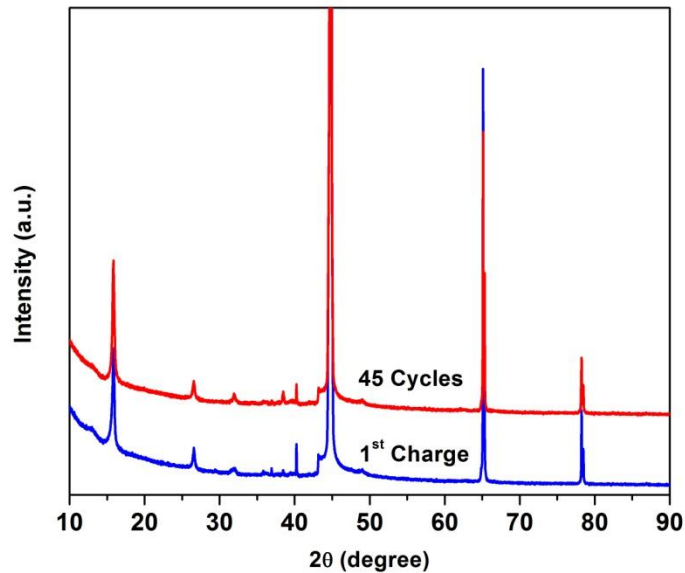
Figure 6.17 XRD patterns of $Na_{0.67}MnO_2$ after the initial charge and after 45 cycles
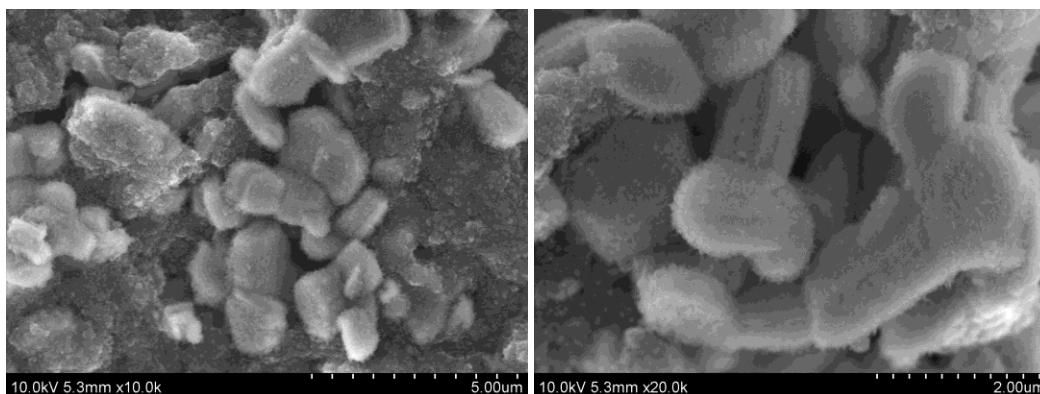
Figure 6.18 SEM images of $Na_{0.67}MnO_2$ after cycling

6.4 Conclusion

In summary, $Na_{0.67}MnO_2$ and $Na_{0.67}Mn_{0.65}Fe_{0.20}Ni_{0.15}O_2$ particles were synthesized using an USP process. The $Na_{0.67}MnO_2$ cathodes can deliver 176 mAh g^{-1} capacity at a low rate of 0.1C, and 138 mAh g^{-1} at 1C, and maintains 73% of capacity at 2C. After 225 cycles at 1C, $Na_{0.67}MnO_2$ cathodes can still provide 134 mAh g^{-1}, which is 97% of initial capacity. The $Na_{0.67}Mn_{0.65}Fe_{0.20}Ni_{0.15}O_2$ cathodes can deliver 150 mAh g^{-1} capacity at a low rate of 0.1C, and 106 mAh g^{-1} at 1C, and maintains 61% of capacity at 2C. After 350 cycles at 1C, $Na_{0.67}Mn_{0.65}Fe_{0.20}Ni_{0.15}O_2$ cathodes can provide 100% of initial capacity. This enhanced electrochemical performance is attributed to stability of the crystal structure as well as the micron size particles that can accommodate the continuous strains and distortions resulting from the insertion and extraction of Na^+ ions in the host material. Sodium ion batteries using P2- layered oxides are suitable for application in large-scale energy storage with moderate voltage windows.

References

[6.1] Dunn B., Kamath H., Tarascon J.M., Science. 334 **(2011)** 928.

[6.2] Palomares V., Serras P., Villaluenga I., Hueso K.B., Carretero-Gonzalez J.,

Rojo T., Energy Environ. Sci. 5 **(2012)** 5884.

[6.3] Wenzel S., Hara T., Janek J., Adelhelm P., Energy Environ Sci. 4 **(2011)** 3342.

[6.4] Stevens D. A., Dahn J. R., J. Electrochem Soc. 147 **(2000)** 4428.

[6.5] Wenzel S., Hara T., Janek J., Adelhelm P., Energy Environ. Sci. 4 **(2011)** 3342.

[6.6] Park S., Gocheva I., Okada S., Yamaki J., J. Electrochem Soc. 158 **(2011)**

A1067.

[6.7] Xiong H., Slater M., Balasubramanian M., Johnson C., Rajh T., J. Phys Chem

Lett. 2 **(2011)** 2560.

[6.8] Chevrier V., Ceder G., J Electrochem Soc. 158 **(2011)** A1011.

[6.9] Langrock A., Xu Y., Liu Y., Ehrman S., Manivannan A., Wang C., J. Power

Sources 223 **(2013)** 62.

[6.10] Ellis B., Makahnouk W., Makimura Y., Toghill K., Nazar L., Nature Mat. 6

(2007) 749.

[6.11] Kawabe Y., Yabuuchi N., Kajiyama M., Fukuhara N., Inamasu T., Okuyama

R., Nakai I., Komaba S., *Electrochem. Commun.* 13.11 **(2011)** 1225.

[6.12] Barker J., Saidi M., Swoyer J., *Electrochemical and Solid-State Letters* 6

(2003) A1.

[6.13] Meins J., J. Solid State Chem. 148 **(1999)** 260.

[6.14] Zhuo H., Wang X., Tang A., Liu Z., Gamboa S., Sebastian P., J. Power

Sources 160 **(2006)** 698.

[6.15] Liu Z., Wang X., Wang Y., Tang A., Yang S., He L., Trans. Nonferrous Met. Soc. China 18 (**2008**) 346.

[6.16] Ding J., Zhou Y., Sun Q., Fu Z., Electrochem.Commun. 22 (**2012**) 85.

[6.17] D'Arienzo M., Ruffo R., Scotti R., Morazzoni F., Mari C., Polizzi S., *Phys. Chem.* 14 (**2012**) 5945.

[6.18] Ding J.J., Zhou Y.N., Sun Q., Yu X.Q., Yang X.Q., Fu Z.W., *Electrochimica Acta* 87 (**2013**) 388.

[6.19] Komaba S., Yabuuchi N., Nakayama T., Ogata A., Ishikawa T., Nakai I., *Inorg. Chem.* 51 (**2012**) 6211.

[6.20] Kim D., Lee E., Slater M., Lu W., Rood S., Johnson C., *Electrochem. Commun.* 18 (**2012**) 66.

[6.21] Parant J., Olazcuaga R., Devallete M., Fouassier C., Hagenmuller P., J. Solid State Chem. 3 (**1971**) 1.

[6.22] Paulsen J., Thomas C., Dahn J., J. Electrochem. Soc. 146 (**1999**) 3560.

[6.23] Bach S., Pereira-Ramos J. P., Baffier N., J. Solid State Chem. 120 (**1995**) 70.

[6.24] Chen R., Chiragyl T., Zavalij P., Whittingham M., Solid State Ionics 1 (**1996**) 86.

[6.25] Caballero A., Hernan L., Morales J., Sanchez L., Santos Pena J., Aranda M., J. Mater. Chem. 12 (**2002**) 1142.

[6.26] Yabuuchi N., Kajiyama M., Iwatate J., Nishikawa H., Hitomi S., Okuyama R., Usui R., Yamada Y., Komaba S., Nature Materials 11 (**2012**) 512.

[6.27] Mortemard de Boisse B., Carlier D., Guignard M., Delmas C., J. Electrochem. Soc. 160 (**2013**) A569.

[6.28] Thorne J.S., Dunlap R.A., Obrovac M.N., J. Electrochem. Soc. 160 **(2012)** A361.

[6.29] Yuan D., Hu X., Qian J., Pei F., Wu F., Mao R., Ai X., Yang H., Cao Y., Electrochimica Acta 116 **(2014)** 300.

[6.30] Kim D., Lee E., Slater M., Lu W., Rood S., Johnson C.S., Electrochemistry Communications 18 **(2012)** 66.

[6.31] Wang H., Yang B., Liao X.-Z., Xu J., Yang D., He Y.-S., Ma Z.-F., Electrochimica Acta 113 **(2013)** 200.

[6.32] Lu Z., Beaulieu L.Y., Donaberger R.A., Thomas C.L., Dahn J.R., J. Electrochem. Soc. 149 **(2002)** A778.

[6.33] Ma X., Chen H., Ceder G., J. Electrochem. Soc. 158 **(2011)** A1307.

Chapter 7: Conclusion and Future Work

7.1 Conclusion

The principle motivation behind this dissertation is the development of cathode materials to enhance the performance of lithium and sodium ion batteries. To accomplish this, an ultrasonic spray pyrolysis (USP) technique was utilized. Four separate studies were conducted with the view of improving the electrochemical performance of $LiNi_{0.5}Mn_{1.5}O_4$, lithium-rich, Na_2FePO_4F, and P2-type layered oxide cathodes.

In the first study, $LiNi_{0.5}Mn_{1.5}O_4$ particles were synthesized using an USP process. The XRD spectrum showed that the annealed material was a single phase spinel with the disordered Fd3m structure. The $LiNi_{0.5}Mn_{1.5}O_4$ cathodes can deliver capacity close to the theoretical value at 0.1 C, while maintaining excellent cycle stability. From these results, ultrasonic spray pyrolysis has the potential to produce valuable energy storage materials with excellent electrochemical properties.

The second study investigated $Li_{1.2}Mn_{0.54}Co_{0.13}Ni_{0.13}O_2$ particles synthesized using an USP process with post annealing (600-800 °C for 6 hrs). All the powders produced are spherical in shape and submicron in size. According to the XRD spectra, electrochemically inactive Li_2MnO_3 is observed for the composite material. During the initial charge, the composite materials exhibit a smooth increase in voltage due to

the $Ni^{2+/4+}$ redox couple. A voltage plateau around 4.5 V is due to the electrochemical extraction of Li_2O from Li_2MnO_3. Among the composites tested, $Li_{1.2}Mn_{0.54}Co_{0.13}Ni_{0.13}O_2$ cathodes heat treated at 800 °C were the most promising, exhibiting high capacity of 277 mAh g^{-1} at a current density of 20 mA g^{-1} with an initial coulombic efficiency of 80% and good cycle stability.

The third study demonstrates the ability to synthesize hollow porous carbon coated material using USP. Specifically, Na_2FePO_4F spheres with 500 nm diameter and 80 nm wall thickness are synthesized using sucrose as the carbon source. Nano-sized porous hollow Na_2FePO_4F spheres allow electrolyte to penetrate into the hollow structure, and thus the electrochemical reaction can take place on both the outside and inside surface and in the pores. Also, the carbon coating on Na_2FePO_4F hollow spheres enhances the electronic conductivity and charge transfer reaction kinetics.

The fourth study aimed to significantly increase the capacity of NIB cathodes by investigating the P2-type layered oxide class. $Na_{0.67}MnO_2$ and $Na_{0.67}Mn_{0.65}Fe_{0.20}Ni_{0.15}O_2$ particles were synthesized using an USP process. The $Na_{0.67}MnO_2$ cathodes can deliver 176 mAh g^{-1} capacity at a low rate of 0.1C, and 138 mAh g^{-1} at 1C. After 225 cycles at 1C, $Na_{0.67}MnO_2$ cathodes can still provide 97% of initial capacity. The $Na_{0.67}Mn_{0.65}Fe_{0.20}Ni_{0.15}O_2$ cathodes can deliver 150 mAh g^{-1} capacity at a low rate of 0.1C, and 106 mAh g^{-1} at 1C. After 350 cycles at 1C, $Na_{0.67}Mn_{0.65}Fe_{0.20}Ni_{0.15}O_2$ cathodes can provide 100% of initial capacity. This enhanced electrochemical performance is attributed to stability of the crystal structure

as well as the micron size particles that can accommodate the continuous strains and distortions resulting from the insertion and extraction of Na^+ ions in the host material. Sodium ion batteries using P2- layered oxides are suitable for application in large-scale energy storage with moderate voltage windows.

These four studies demonstrate the versatility of the spray pyrolysis process to produce a range of complex multicomponent ceramic cathode materials, each exhibiting excellent electrochemical performance. The method has the added benefit of continuous formation of particles in one step, thus it can be applied to industry. As a result, spray pyrolysis is ideal for synthesizing electrode materials for batteries.

7.2 Future Work

As demonstrated by the Na_2FePO_4F study, a thin carbon coating is beneficial to the electrochemical performance of the material. Specifically, carbon coating decreases both surface layer resistance and charge transfer reaction, indicating an enhancement in the kinetics of both lithium-ion and sodium-ion diffusion. This leads to an increase in rate capability. The carbon coating has the added benefit of preventing the dissolution of transition metals into the electrolyte, which favors cycle stability. Traditionally it has been a challenge to coat cathode materials with carbon since the majority requires heat treatment in air to obtain the electrochemically active phase, thus eliminating any carbon that may have formed prior. A novel ultrasonic spray pyrolysis system can be used to effectively coat any electrode with a thin layer of carbon. The design is shown in **Figure 7.1**.
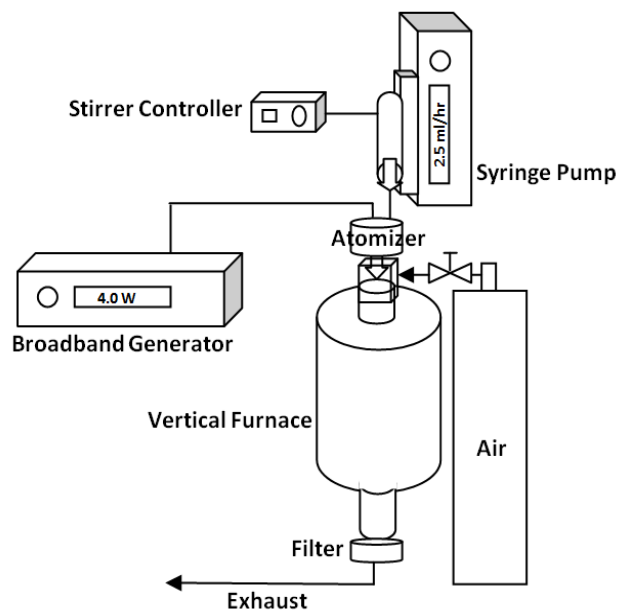
Figure 7.1 Schematic of vertical spray pyrolysis system

The slurry solution consists of heat treated cathode powder suspended in water. Sucrose is dissolved in the water as carbon source. The system is comprised of a broadband generator which provides the power to the atomizer, while a magnetic stirring syringe enables the effective mixing of the slurry as it is fed to the atomizer. The residence time in air is sufficiently short to allow the decomposition of the carbon source (sucrose) without further reduction of the cathode material. A vertical configuration allows the solid particles to reach the filter for collection with high efficiency.

The lithium-rich material presented in Chapter 4 has been successfully carbon coated as demonstrated by the Raman spectroscopy in **Figure 7.2**. Strong D (defective

graphitic structures) and G-bands (graphitic layers) from elemental carbon on the materials are observed at 1330 cm^{-1} and 1570 cm^{-1}, respectively.
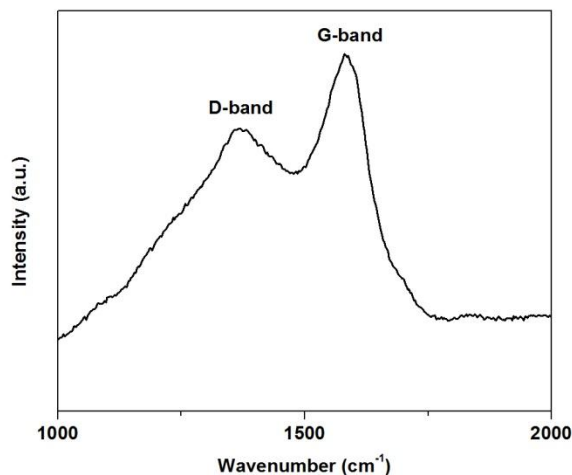
Figure 7.2 Raman spectra of C/Li$_{1.2}$Mn$_{0.54}$Co$_{0.13}$Ni$_{0.13}$O$_2$ sample

The precursor ratio of active cathode material to sucrose was 1 to 5 by weight, while the furnace temperature was set to 700 ˚C. Air was used as carrier gas to prevent the reduction of the cathode material during pyrolysis of the sucrose. According to the XRD pattern **(Figure 7.3)** the correct phase is maintained after the respray experiment.
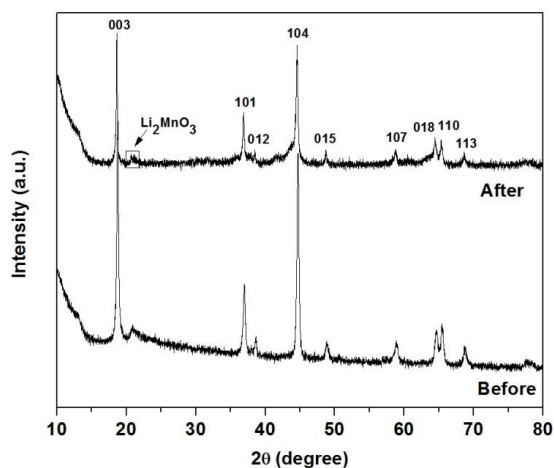
Figure 7.3 XRD full-pattern fitting of $Li_{1.2}Mn_{0.54}Co_{0.13}Ni_{0.13}O_2$ sample before and

after the respray experiment

Cycle life data for the lithium-rich cathode material before and after carbon coating is

shown in **Figure 7.4**. The first ten cycles show a similar trend when cycled at the

current density of 20 mA g^{-1}.
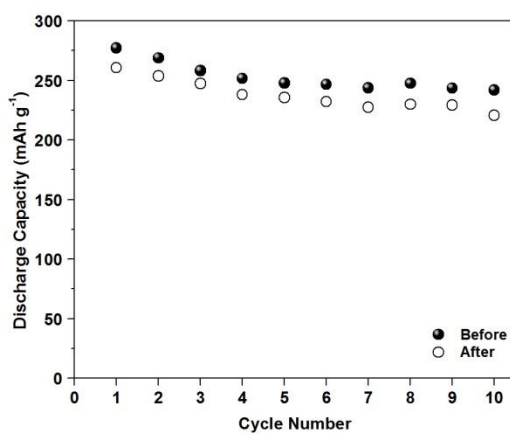
Figure 7.4 Capacity retention of $Li_{1.2}Mn_{0.54}Co_{0.13}Ni_{0.13}O_2$ cycled at 20 mA g^{-1}

before and after carbon coating

Prior to carbon coating the rate test showed no performance when cycled at a current density exceeding 20 mA g^{-1}. The poor kinetics is due to a fraction of the insulating Li$_2$MnO$_3$ component being transformed from a layered structure to a spinel-like region. This phase transformation can reduce the rate of free migration of Li ions. The carbon coating increases the electronic conductivity thus enhancing the rate capability. As demonstrated by **Figure 7.5** the carbon coated Li$_{1.2}$Mn$_{0.54}$Co$_{0.13}$Ni$_{0.13}$O$_2$ can be cycled at a current density of 200 mA g^{-1} and shows excellent cycle life.
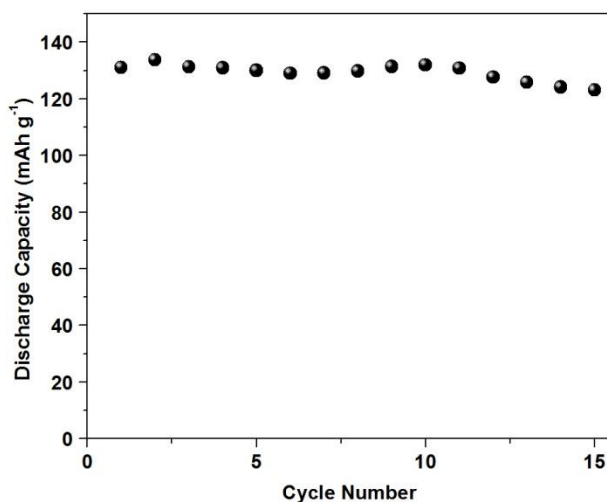
Figure 7.5 Capacity retention of C/Li$_{1.2}$Mn$_{0.54}$Co$_{0.13}$Ni$_{0.13}$O$_2$ cycled at 200 mA g^{-1}

Additional respray experiments for the P2-type layered oxides discussed in Chapter 6 will be carried out to enhance the rate capability. Due to the short residence time, this unique approach enables for the first time oxide materials to be carbon coated without being reduced.

Appendix

Change in Crystal Structures
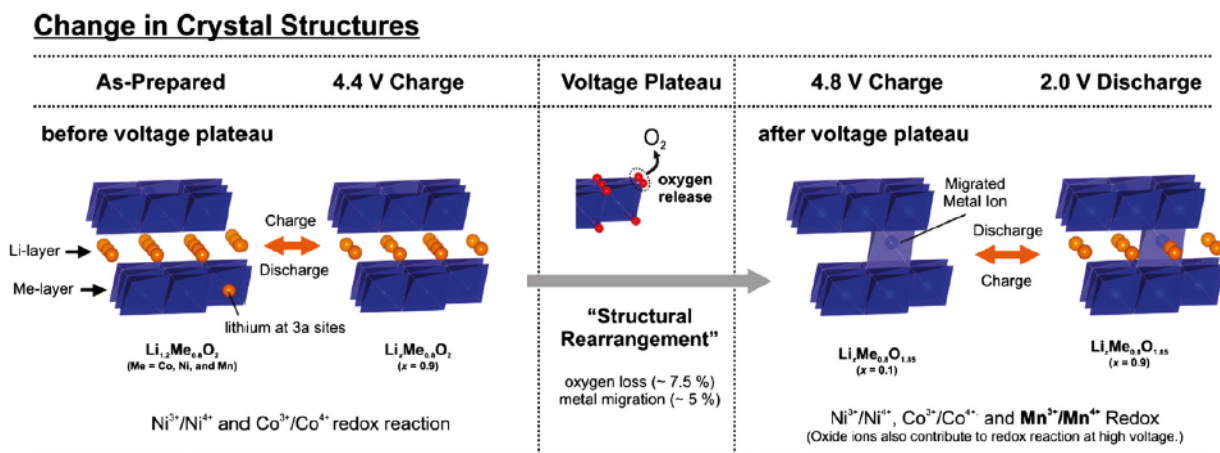
Figure A.1 Schemes of the crystal structural change mechanisms of $Li_{1.2}Ni_{0.13}Co_{0.13}Mn_{0.54}O_2$ charged/discharged between 2.0 and 4.8 V [4.11]
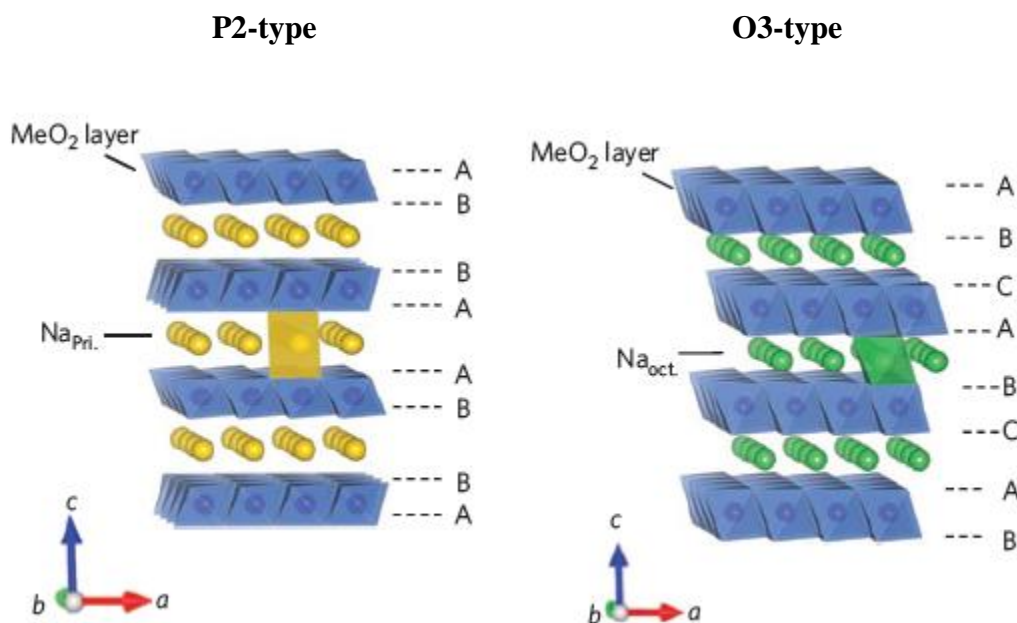
P2-type   **O3-type**

Figure A.2 Schematic illustrations of P2-type and O3-type crystal structures. Symbols A, B and C in the schematics represent the three different oxygen layers. A greater interlayer spacing is observed for the P2 phase because of the repulsive electrostatic interaction of the AA-type oxygen stacking to form prismatic sites. [6.33]

Publications

1. Luo C., Xu Y., Zhu Y., Liu Y., Zheng S., Liu Y., Langrock A., Wang C., *ACS Nano*, 9 (**2013**) 8003.

2. Xu Y., Liu Q., Zhu Y., Liu Y., Langrock A., Zachariah M., Wang C., *Nano Letters*, 13 (**2013**) 470.

3. Wen Y., Zhu Y., Langrock A., Manivannan A., Ehrman S., Wang C., *Small*, 9 (**2013**) 2810.

4. Langrock A., Xu Y., Liu Y., Ehrman S., Manivannan A., Wang C., *J. Power Sources*, 223 (**2013**) 62.

5. Chen X., Guo J., Gerasopoulos K., Langrock A., Brown A., Ghodssi R., Culver J. N., Wang C., *J. Power Sources*, 211 (**2012**) 129.

Conference

Langrock A. "Electrochemical Properties and Characterization of

$Li_{1.2}Mn_{0.54}Co_{0.13}Ni_{0.13}O_2$ Composite Cathode Powders Prepared by Ultrasonic Spray

Pyrolysis," (Oral) AIChE Annual Conference, San Francisco, CA, **2013**.

Innovation in This Research

1. To achieve both high power density and high energy density, nanostructured sphere particles with controlled porosity and high tapping density are desired for both Li-ion and Na-ion batteries. The versatile and facile ultrasonic spray pyrolysis method allows for the synthesis of a variety of electrode materials with sphere morphology. Work has been done to develop electrode materials through an aerosol method that can be readily applied to industry.

2. Hollow and porous spheres offer several advantages over dense particles, including fast mass transfer and large reaction area, thus improving the electrochemical reaction kinetics. In addition, the interior void of hollow spheres can effectively accommodate the volume change, enhancing the structural stability by releasing the strain, thus improving the cycling stability. Ultrasonic spray pyrolysis is a one-step template-free synthetic method for the fabrication of hollow structure material.

3. A thin carbon coating is beneficial to the electrochemical performance of the material. Specifically, carbon coating decreases both surface layer resistance and charge transfer reaction, indicating an enhancement in the kinetics of both lithium-ion and sodium-ion diffusion. This leads to an increase in rate capability. The carbon coating has the added benefit of preventing the dissolution of transition metals into the electrolyte, which favors cycle stability. Ultrasonic spray pyrolysis can be used to effectively coat any electrode, including metal oxides, with a thin layer of carbon.

References

[2.1] Tarascon J.M., Armand M. *Nature*, 414 (**2001**) 359.

[2.2] Tarascon J.M., Armand M. *Nature*, 451 (**2008**) 652.

[2.3] Rotem M., Amalraj S.F., Leifer N., Jacob D., Aurbach D., J. Mater. Chem., 21 (**2011**) 9938.

[2.4] Fujimoto H., Tokumitsu K., Mabuchi A., Chinnasamy N., Kasuh T., J. Power Sources 195 (**2010**) 7452.

[2.5] Meunier V., Kephart J., Roland C., Bernholc J., Phys. Rev. Lett. 88 (**2002**) 075506.

[2.6] Hou J., Shao Y., Ellis M.W., Moore R.B., Yi B., Phys. Chem. Chem. Phys. 13 (**2011**) 15384.

[2.7] Chen Z., Belharouak I., Sun Y.K., Amine K., Adv. Funct. Mater. 23 (**2013**) 959.

[2.8] Szczech J.R., Jin S., Energy Environ. Sci. 4 (**2011**) 56.

[2.9] Rudawski N.G., Yates B.R., Holzworth M.R., Jones K.S., Elliman R.G., Volinsky A.A., J. Power Sources 223 (**2013**) 336.

[2.10] Bruce P.G., Scrosati B., Tarascon J.-M., Angew. Chem. Int. Ed. 47 (**2008**) 2930.

[2.11] Park C.-M., Kim J.-H., Kim H., Sohn H.-J., Chem. Soc. Rev. 39 (**2010**) 3115.

[2.12] Wang Z., Zhou L., Lou X.W., Adv. Mater. 24 (**2012**) 1903.

[2.13] Yang J., Takeda Y., Imanishi N., Capiglia C., Xie J.Y., Yamamoto O., Solid State Ionics 152 (**2002**) 125.

[2.14] Jiang J., Li Y., Liu J., Huang X., Yuan C., Lou X.W., Adv. Mater. 24 (**2012**) 5166.

[2.15] Lai C.-H., Lu M.-Y., Chen L.-J., J. Mater. Chem. 22 (**2012**) 19.

[2.16] Wenzel S., Hara T., Janek J., Adelhelm P., *Energy Environ. Sci.* 4 (**2011**) 3342.

[2.17] Palomares V., Casas-Cabanas M., Castillo-Martínez E., Han M. H., Rojo T.*,*
Energy Environ. Sci., 6 (**2013**) 2312.

[2.18] Dunn B., Kamath H., Tarascon J.M., *Science* 334 (**2011**) 928.

[2.19] Bouguslavskii Y., Eknadiosyants O., Soviet Phys. Acoust. 15 (**1969**) 14.

[2.20] Zhang, L. "Preparation of Multi-component Ceramic Nanoparticles."
Literature Review. Center for Industrial Sensors and Measurements Department
Materials Science & Engineering Group Inorganic Materials Science, Ohio State
University, **2004**.

[2.21] Gurav A., Kodas T., Pluym T., Xiong Y., Aerosol Sci. and Tech., 19.4 (**1993**)
411.

[2.22] Ranjan R., Pandit A., Ultrasonics 39 (**2001)** 235.

[2.23] Wang W., Purwanto A., Lenggoro I., Okuyama K., Chang H., Jang H.,
Industrial & Engineering Chem. Research 47.5 (**2008**) 1650.

[3.1] Wu, Yongmin, Zhenhai Wen, Hongbin Feng, and Jinghong Li. *Small* 8.6 (**2012**)
858.

[3.2] Xi, Liu Jiang, Hong-En Wang, Zhou Guang Lu, Shi Liu Yang, Ru Guang Ma,
Jian Qiu Deng, and C.Y. Chung. *J. Power Sources* 198 (**2012**) 251.

[3.3] Cabana, J., T. Valdessolis, M. Palacin, J. Orosole, A. Fuertes, G. Marban, and
A. Fuertes. *J. Power Sources* 166.2 (**2007**) 492.

[3.4] Ding, Yuan-Li, Jian Xie, Gao-Shao Cao, Tie-Jun Zhu, Hong-Ming Yu, and Xin-
Bing Zhao. *Adv. Funct. Mater* 21 (**2011**) 348.

[3.5] Huang, Xingkang, Min Lin, Qingsong Tong, Xiuhua Li, Ying Ruan, and Yong Yang. *J. Power Sources* 202 (**2012**) 352.

[3.6] Moon, Hee-Soo, and Jong-Wan Park. *J. Power Sources* 119-121 (**2003**) 717.

[3.7] Sigala, C., D. Guyomard, A. Verbaere, Y. Piffard, and M. Tournoux. *Solid State Ionics* 81.3-4 (**1995**) 167.

[3.8] Gu, Xin, Xiaowei Li, Liqiang Xu, Huayun Xu, Jian Yang, and Yitai Qian. *Int. J. Electrochem. Sci* 7 (**2012**) 2504.

[3.9] Amine, K., H. Tukamoto, H. Yasuda, and Y. Fujita. *J. Power Sources* 68 (**1997**) 604.

[3.10] Shigemura, H., H. Sakaebe, H. Kageyama, H. Kobayashi, A. R. West, R. Kanno, S. Morimoto, S. Nasu, and M. Tabuchi. *J. Electrochem. Soc.* 148.7 (**2001**) A730.

[3.11] Eli, Yair Ein, W. F. Howard, Jr., Sharon H. Lu, Sanjeer Mukerjee, James McBreen, John T. Vaughey, and Michael M. Thackeray. *J. Electrochem. Soc.* 145.4 (**1998**) 1238.

[3.12] Zhou, Liang, Dongyuan Zhao, and XiongWen Lou. *Angew. Chem. Int. Ed.* 51 (**2012**) 239.

[3.13] Akao, Shinsuke, Motofumi Yamada, Takayuki Kodera, Kenichi Myoujin, and Takashi Ogihara. *Advances in Materials Science and Engineering* 2011 (**2011**) 1.

[3.14] Zhang, Minghao, Jun Wang, Yonggao Xia, and Zhaoping Liu. *J. Alloys and Compounds* 518 (**2012**) 68.

[3.15] Yi, Ting-Feng, and Xin-Guo Hu. *J. Power Sources* 167.1 (**2007**) 185.

[3.16] Santhanam, R., and B. Rambabu. *J. Power Sources* 195 (**2010**) 5442.

[3.17] Kim, J.-H., S.-T. Myung, C. S. Yoon, S. G. Kang, and Y.-K. Sun. *Chem. Mater.* 35.21 (**2004**) 906.

[3.18] Xia, H., Y. S. Meng, L. Lu, and G. Ceder. *J. Electrochem. Soc.* 154.8 (**2007**) A737.

[4.1] Chebaim, R. V., Prado, F., Manthiram, A. *Chem. Mater.* 13 (**2001**) 2951.

[4.2] Kim D., Sandi G., Croy J.R., Gallagher K.G., Kang S.H., Lee E., Slater M.D., Johnson C.S., Thackeray M.M., *J. Electrochem. Soc.* 160.1 (**2013**) A31.

[4.3] Song B., Lai M.O., Lu L., *Electrochim. Acta* 80 (**2012**) 187.

[4.4] Johnson C. S., Kim J. S., Lefief C., Li N., Vaughey J. T., Thackeray M. M., *Electrochem. Commun.*, 6, (**2004**) 1085.

[4.5] Kang S.H., Thackeray M.M., *Electrochem. Commun.* 11 (**2009**) 748.

[4.6] Peng Q.W., Tang Z.Y., Zhang L.Q., Liu X.J., *Mater. Res. Bull.* 44 (**2009**) 2147.

[4.7] Sivaprakash S., Majumder S.B., *Solid State Ionics* 181 (**2010**) 730.

[4.8] Kim D., Kang S.-H., Balasubramanian M., Johnson C.S., *Electrochem. Commun.*12 (**2010**) 1618.

[4.9] Shi S.J., Tu J.P., Tang Y.Y., Yu Y.X., Zhang Y.Q., Wang X.L., *J. Power Sources* 221(**2013**) 300.

[4.10] Haik O., Martha S.K., Sclar H., Samuk-Fromovich Z., Zinigrad E., Markovsky B., Kovacheva D., Saliyski N., Aurbach D., *Thermochim. Acta* 493 (**2009**) 96.

[4.11] Yabuuchi N., Yoshii K., Myung S.T., Nakai I, Komaba S., J. Am. Chem. Soc. 133 (**2011**) 4404.

[5.1] Dunn B., Kamath H., Tarascon J.M.. *Science* 334, (**2011)** 928.

[5.2] Palomares V., Serras P., Villaluenga I., Hueso K.B., Carretero-Gonzalez J., Rojo T. *Energy and Environmental Science* 5 (**2012**) 5884.

[5.3] Vidal-Abarca C., Lavela P., Tirado J.L., Chadwick A.V., Alfredsson M., Kelder E. *J. Power Sources* 197 (**2012**) 314.

 [5.4] Kawabe Y., Yabuuchi N., Kajiyama M., Fukuhara N., Inamasu T., Okuyama R., Nakai I., Komaba S. *Electrochem.Commun.*13.11 (**2011**) 1225.

 [5.5] Yao, Y., McDowell M. T., Ryu I., Wu H., Liu N., Hu L., Nix W. D., Cui Y. *Nano Letters*, 11 (**2011**) 2949.

[5.6] Wu H., Chan G., Choi J. W., Ryu I., Yao Y., McDowell M. T., Lee S.W., Jackson A., Yang Y., Hu L., Cui Y. *Nature Nanotechnology*, 7 (**2012**) 310.

[5.7] Dong, F., Huang Y., Zou S., Liu J., Lee S. C. *J. Physical Chem. C* 115 (**2011**) 241.

[5.8] Ortega, J., Kodas T.T.. *J. Aerosol Science* 23 (**1992**) 253.

[5.9] Patil, L.A., Shinde M.D., Bari A.R., Deo V.V. *Sensors and Actuators B: Chem.* 143 (**2009**) 316.

[6.1] Dunn B., Kamath H., Tarascon J.M., Science. 334 (**2011**) 928.

[6.2] Palomares V., Serras P., Villaluenga I., Hueso K.B., Carretero-Gonzalez J., Rojo T., Energy Environ. Sci. 5 (**2012**) 5884.

[6.3] Wenzel S., Hara T., Janek J., Adelhelm P., Energy Environ Sci. 4 (**2011**) 3342.

[6.4] Stevens D. A., Dahn J. R., J. Electrochem Soc. 147 (**2000**) 4428.

[6.5] Wenzel S., Hara T., Janek J., Adelhelm P., Energy Environ. Sci. 4 (**2011**) 3342.

[6.6] Park S., Gocheva I., Okada S., Yamaki J., J. Electrochem Soc. 158 (**2011**) A1067.

[6.7] Xiong H., Slater M., Balasubramanian M., Johnson C., Rajh T., J. Phys Chem Lett. 2 (**2011**) 2560.

[6.8] Chevrier V., Ceder G., J Electrochem Soc. 158 (**2011**) A1011.

[6.9] Langrock A., Xu Y., Liu Y., Ehrman S., Manivannan A., Wang C., J. Power Sources 223 (**2013**) 62.

[6.10] Ellis B., Makahnouk W., Makimura Y., Toghill K., Nazar L., Nature Mat. 6 (**2007**) 749.

[6.11] Kawabe Y., Yabuuchi N., Kajiyama M., Fukuhara N., Inamasu T., Okuyama R., Nakai I., Komaba S., *Electrochem. Commun.* 13.11 (**2011**) 1225.

[6.12] Barker J., Saidi M., Swoyer J., *Electrochemical and Solid-State Letters* 6 (**2003**) A1.

[6.13] Meins J., J. Solid State Chem. 148 (**1999**) 260.

[6.14] Zhuo H., Wang X., Tang A., Liu Z., Gamboa S., Sebastian P., J. Power Sources 160 (**2006**) 698.

[6.15] Liu Z., Wang X., Wang Y., Tang A., Yang S., He L., Trans. Nonferrous Met. Soc. China 18 (**2008**) 346.

[6.16] Ding J., Zhou Y., Sun Q., Fu Z., Electrochem.Commun. 22 (**2012**) 85.

[6.17] D'Arienzo M., Ruffo R., Scotti R., Morazzoni F., Mari C., Polizzi S., *Phys. Chem.* 14 (**2012**) 5945.

[6.18] Ding J.J., Zhou Y.N., Sun Q., Yu X.Q., Yang X.Q., Fu Z.W., *Electrochimica Acta* 87 (**2013**) 388.

[6.19] Komaba S., Yabuuchi N., Nakayama T., Ogata A., Ishikawa T., Nakai I., *Inorg. Chem.* 51 (**2012**) 6211.

[6.20] Kim D., Lee E., Slater M., Lu W., Rood S., Johnson C., *Electrochem. Commun.* 18 **(2012)** 66.

[6.21] Parant J., Olazcuaga R., Devallete M., Fouassier C., Hagenmuller P., J. Solid State Chem. 3 **(1971)** 1.

[6.22] Paulsen J., Thomas C., Dahn J., J. Electrochem. Soc. 146 **(1999)** 3560.

[6.23] Bach S., Pereira-Ramos J. P., Baffier N., J. Solid State Chem. 120 **(1995)** 70.

[6.24] Chen R., Chiragyl T., Zavalij P., Whittingham M., Solid State Ionics 1 **(1996)** 86.

[6.25] Caballero A., Hernan L., Morales J., Sanchez L., Santos Pena J., Aranda M., J. Mater. Chem. 12 **(2002)** 1142.

[6.26] Yabuuchi N., Kajiyama M., Iwatate J., Nishikawa H., Hitomi S., Okuyama R., Usui R., Yamada Y., Komaba S., Nature Materials 11 **(2012)** 512.

[6.27] Mortemard de Boisse B., Carlier D., Guignard M., Delmas C., J. Electrochem. Soc. 160 **(2013)** A569.

[6.28] Thorne J.S., Dunlap R.A., Obrovac M.N., J. Electrochem. Soc. 160 **(2012)** A361.

[6.29] Yuan D., Hu X., Qian J., Pei F., Wu F., Mao R., Ai X., Yang H., Cao Y., Electrochimica Acta 116 **(2014)** 300.

[6.30] Kim D., Lee E., Slater M., Lu W., Rood S., Johnson C.S., Electrochemistry Communications 18 **(2012)** 66.

[6.31] Wang H., Yang B., Liao X.-Z., Xu J., Yang D., He Y.-S., Ma Z.-F., Electrochimica Acta 113 **(2013)** 200.

[6.32] Lu Z., Beaulieu L.Y., Donaberger R.A., Thomas C.L., Dahn J.R., J. Electrochem. Soc. 149 **(2002)** A778.

[6.33] Ma X., Chen H., Ceder G., J. Electrochem. Soc. 158 **(2011)** A1307.